

# Distant Sound Source Positioning by a 3D Octagonal Microphone Array Optimized by Improved Weighted Beamforming Algorithm

Mohammad Reza Tayuri<sup>1</sup>, Salman Karimi<sup>2\*</sup> 

1, 2- Department of Electrical Engineering, Lorestan University, Khorram-abad, Iran.  
Email: karimi.salman@lu.ac.ir (Corresponding author)

## ABSTRACT:

Audio source localization is one of the most important topics in different fields of signal processing e.g. entertainment, military and security applications. In this way, this article presents a novel approach for intercepting and localizing distant audio sources using a three-dimensional (3D) octagonal microphone array consisting of 23 microphones. The proposed system employs an efficient algorithm for analyzing the information obtained from the microphone array to accurately determine the spatial position of sound sources across a wide frequency range, from infrasound to ultrasonic frequencies. To validate the system efficiency, numerical simulations were conducted through 80 tests using different audio sources with frequencies ranging from 20 Hz to 1 MHz, located at spatial distances of 52 to 402 meters from the array. The results demonstrate the high accuracy of the proposed system in identifying the spatial position of sound sources. The proposed system's performance is optimized using an improved weighted beamforming algorithm, which is implemented in MATLAB software on a core i7, 64-bit, RAM-8GB computer system. The proposed approach has the potential to enhance the capabilities of military and security systems for detecting and localizing sound sources in complex environments.

**KEYWORDS:** Source Localization 3D Microphone Array; Weighted beamforming; Array Geometry; Sound Signal

## 1. INTRODUCTION

In recent years, the positioning of signal generation sources has emerged as a key research area across various domains, including global positioning systems, video conferences, radar and sonar-based interceptions, mobile phone positioning, robotics, and human-computer interaction. This research field also encompasses topics such as speaker tracking [1]-[5], sensor networks, and touch-based human-computer interactions. In this article, we propose a new method for identifying the position of sound sources using audio imaging. Audio imaging is a technique used to track audio signals and detect the location of their sources [6]. To better understand our proposed system, we first examine the fundamental concepts underlying this issue. Our method has the potential to enhance the accuracy of sound source localization, which is essential in a wide range of applications, including speech recognition, noise reduction, and audio surveillance.

### 1.1. Microphone array

A microphone array refers to a set of microphones arranged in a specific pattern and a geometric shape to capture sound from the surrounding environment. These arrays can be designed in two-dimensional (2D) or three-dimensional (3D) configurations, with various array types available, as illustrated in Fig. 1 [7]. Microphone arrays have gained widespread use in diverse applications such as speech recognition, audio surveillance, acoustic imaging, and noise reduction, among others. The design and configuration of microphone arrays play a crucial role in determining the accuracy and resolution of sound source localization, which is an essential aspect of many audio applications.

Paper type: Research paper

<https://doi.org/xxx>

Received: 17 February 2024; Revised: 28 April 2024; Accepted: 21 June 2024; Published: 1 March 2025

How to cite this paper: M. R. Tayuri, S. Karimi, “**Distant Sound Source Positioning by a 3D Octagonal Microphone Array Optimized by Improved Weighted Beamforming Algorithm**”, *Majlesi Journal of Telecommunication Devices*, Vol. 14, No. 1, pp. 1-17, 2025.

Several studies have shown that the accuracy and speed of sound source localization are directly and inversely related to the dimensions and number of microphones, respectively [8]. These findings suggest that increasing the size and reducing the number of microphones can enhance the accuracy and speed of sound source localization, respectively. However, the optimal design and configuration of microphone arrays depend on the specific application requirements and environmental factors.

## 1.2. Beamforming

Beamforming is a signal processing technique used in sensor arrays to transmit or receive a signal while also determining the direction of the source.

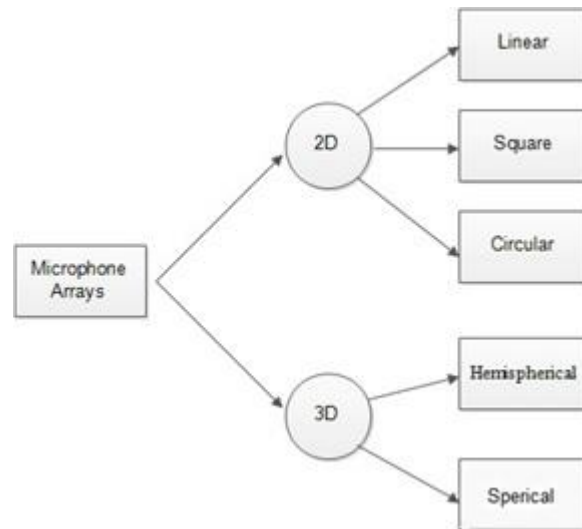


**Fig. 1.** The most common types of arrays based on appearance.

This technique is designed such that the desired signal enters the array microphones at different angles and creates constructive interference to determine the position of the array source [9]. Beamforming, also known as radiography, is a versatile technology that finds applications in various fields of science, such as seismology, radio astronomy, acoustics, radars, and sonars. In audio systems, beamforming is classified into two categories based on the type of microphone array and the working frequency of each microphone: active and passive audio imaging [10].

- Active audio imaging employs a specific wavelength to send a signal for imaging, instead of using the sound of environmental sources directly. In this approach, the sent audio signal collides with the elements in the surrounding environment and will be analyzed after returning [6]. These structures are widely used in various medical and military fields, such as ultrasound and subsurface radars. In these systems, the speed of sound is calculated as a compressed wave using equation (1), and the time interval between sending and receiving the signal, according to equation (2), is used to determine the distance of the desired object from the source [11]. Beamforming in audio systems is a powerful tool for enhancing the accuracy and resolution of sound source localization, which is essential in various audio applications, including speech recognition, noise reduction, and audio surveillance. The effectiveness of beamforming depends on factors such as the design and configuration of the microphone array, the characteristics of the sound source, and the environmental conditions.

$$c = 331.1 * \sqrt{1 + \frac{T}{273.15}} \quad (1)$$

$$l = \frac{c * t}{2} \quad (2)$$

where C is the speed of sound in m/s, T is the temperature in degrees Celsius, t is the time difference between sending and receiving the signal, and l is the distance between the source and the target.

- Passive audio imaging is a technique in which the audio imaging system does not emit any signals but rather is sensitive to specific frequencies and wavelengths received from the surrounding environment. By analyzing and

calculating the intensity and angle of these received signals, the system determines the position of the object [6] and [12]. This approach is useful in scenarios where active imaging is not feasible or may interfere with other systems. Passive audio imaging finds applications in various fields, including speech recognition, audio surveillance, and acoustic imaging. The effectiveness of passive audio imaging depends on factors such as the design and configuration of the microphone array, the characteristics of the sound source, and the environmental conditions.

This article proposes a novel method for determining the spatial position of sound sources in the frequency range from Hertz to Mega Hertz with high accuracy, by optimizing the microphone array structure. To the best of our knowledge, this is the first study to present such a method, which has potential applications in various audio-related fields such as speech recognition, acoustic imaging, and audio surveillance. The proposed method enhances the accuracy and resolution of sound source localization by optimizing the design and configuration of the microphone array, which plays a crucial role in determining the performance of passive audio imaging. Some of the most important applications of the proposed system can be stated as follows:

- 1- Automotive and aircraft industries: to identify the weak points of sound insulation and engine and moving parts troubleshooting [13].
- 2- Military industries: passive positioning of moving targets [14], [15].
- 3- Music: the direction of tuning and tuning the instruments and their correct placement in the performance hall [16].
- 4- Police traffic control cameras: to identify cars that cause noise pollution in unauthorized places [17].
- 5- Construction: evaluation of the walls, doors and windows of buildings, to prevent the entry of noise pollution [18], [19].
- 6- Power industry: Specifying the insulators of high pressure distribution and transmission systems that do not have a complete and correct connection with the cables, and this improper connection causes sounds caused by electric discharge [20], [21].
- 7- Robotics: to detect the position of the speaker's voice in noisy environments and also to detect the distance of the speaker's voice [22].
- 8- Subsurface applications: This technology is used to investigate the position of marine organisms such as fish masses and whales and to detect the position of moving targets such as submarines [23], [24].

The paper proposes a novel array configuration for microphones, along with a new approach to constrained optimization for optimal noise suppression. This is achieved by replacing the multi-dimensional optimization process with an efficient two-dimensional search.

The paper is organized as follows: Section 2 introduces different types of microphone arrays. Section 3 evaluates various techniques used for positioning sound sources. Section 4 discusses the proposed method, and its results are illustrated in Section 5. A comparison of the proposed algorithm's outcomes with other methods is provided in Section 6. Finally, the conclusion is presented in Section 7.

## 2. TYPES OF MICROPHONE ARRAY

In this section, we will examine the types of microphone arrays and their different applications.

### 2.1. Linear Array

In a linear microphone array, the microphones are arranged in a row. The distance between the microphones is an important factor that affects the performance of the array and varies depending on the specific application. Two main approaches are commonly used to consider the distance between the microphones in linear arrays. The first approach is to consider the distance in terms of the physical separation between the microphones, which is typically expressed in meters or centimeters. The second approach is to consider the distance in terms of the phase difference between the signals received by the microphones, which is typically expressed in degrees or radians. The optimal distance between the microphones depends on several factors such as the frequency range of the signals, the desired accuracy of sound source localization, and the environmental conditions. They are arranged in two main models:

- Uniforms; in which the distance of all microphones from each other is the same.
- Non-uniform; in which the distance between the microphones increases as the distance from the center of the array increases.

Fig. 2 shows the radiation pattern of a uniform linear microphone array consisting of four microphones placed at an equal distance of 10 cm. The graph indicates that the number of loops obtained at frequencies of 1 and 2 kHz is small and has an asymmetric shape. Therefore, this type of two-dimensional array may not provide sufficient accuracy in audio imaging systems, particularly in the range of speech frequencies. However, this structure offers the simplest calculation method to determine the sound source direction [25]. The optimal design and configuration of a microphone array depend on various factors, including the characteristics of the sound source, the size of the array, and the desired

accuracy of sound source localization. Linear microphone arrays find applications in diverse domains such as speech recognition, audio surveillance, beamforming, and acoustic imaging.

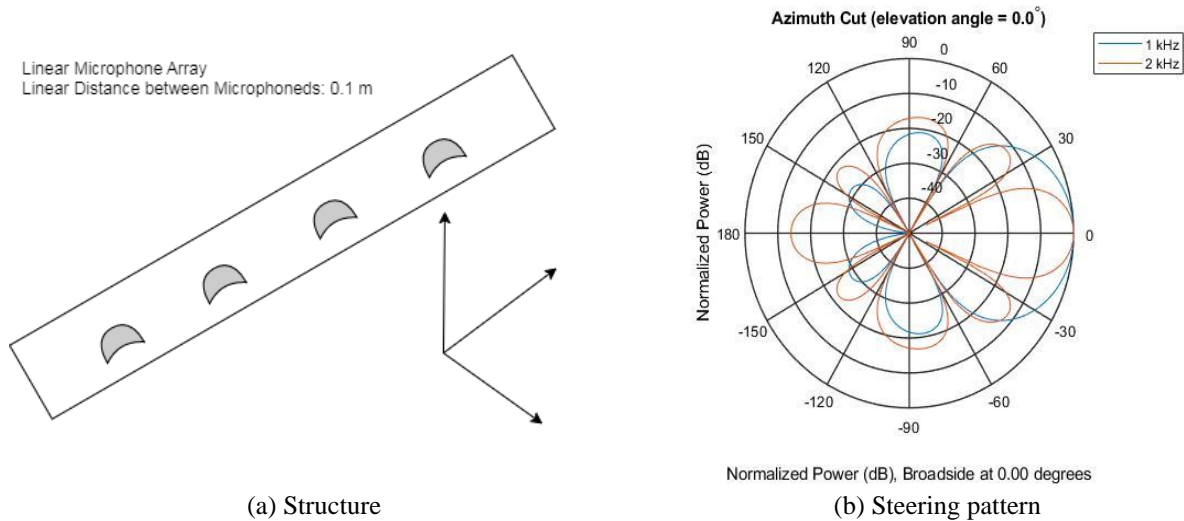


Fig. 2. Linear array.

### 2.2. Circular Array

The circular microphone array is a type of array in which the microphones are placed equidistantly on a circle with a certain radius [10]. This structure is widely used in various industries due to its inherent symmetry and the ability to capture sound from different angles. To increase the efficiency of this structure, microphones can be placed on several concentric circles. Fig. 3 shows an example of this type of array, and Fig. 3b depicts the radiation pattern of an eight-microphone circular array with a radius of 0.5 meters at frequencies of 1 and 2 kHz. As evident from the graph, the radiation pattern is perfectly symmetrical at various angles. Notably, the number of loops at a frequency of 2 kHz is higher, resulting in improved accuracy of the system. The optimal design and configuration of the circular array depend on various factors, such as the size of the array, the frequency range of the signals, and the environmental conditions. Circular microphone arrays find applications in diverse domains such as speech recognition, audio surveillance, beamforming, and acoustic imaging.

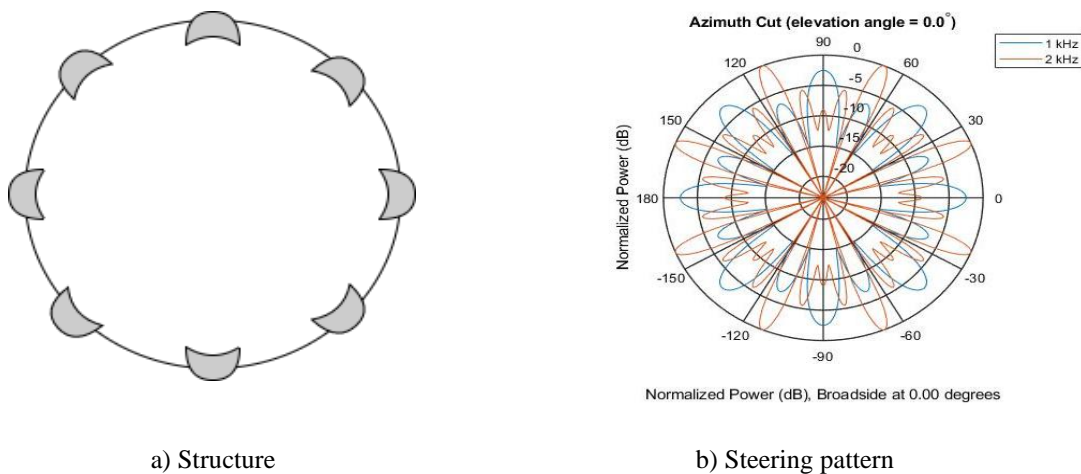


Fig. 3. Circular array.

### 2.3. Square array

The square microphone array is a type of array in which the microphones are arranged in a square structure with a certain distance between them. Fig. 4 shows an example of a square microphone array with 16 microphones arranged in four rows and four columns, each placed at a distance of 0.1 meters from each other. It is evident from the figure that the number of microphones used in the square structure is significantly higher than that used in the circular type.

However, the radiation pattern of the square structure is less accurate than that of the circular structure. Fig. 4 also depicts the radiation pattern of the square array at frequencies of 1 and 2 kHz.

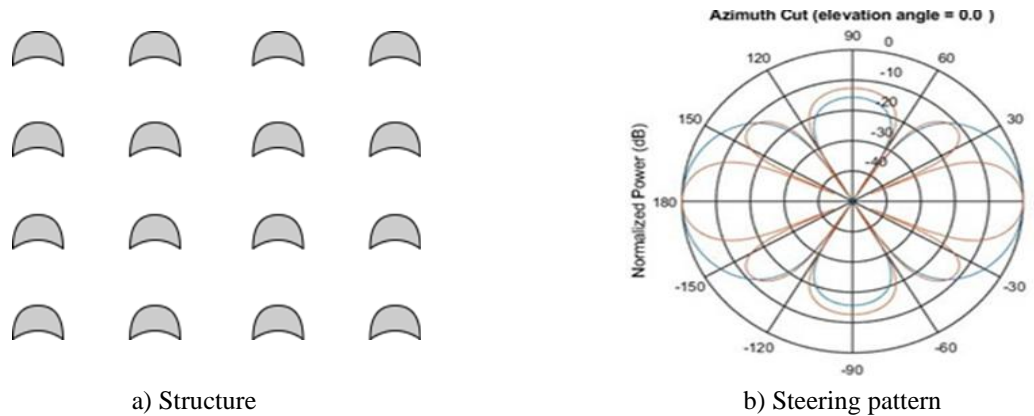


Fig. 4. Square array.

**2.4. Hemispherical array**

The hemispherical microphone array is a three-dimensional structure that consists of multiple circles with different radii placed together with a certain distance and radius. This structure forms a hemisphere and has diverse applications in various systems [26]. Fig. 5 presents an example of a hemispherical array with 17 microphones arranged in three circular layers with radii of 1, 1.5, and 2 meters, designed for implementation at frequencies of 1 and 2 kHz.

**2.5. Spherical array**

The spherical microphone array is a fully three-dimensional structure in which the microphones are arranged in a spherical shape. This structure allows for the capture of sound from all possible angles due to the shape of the microphones. The accuracy of this structure is very high, making it one of the most practical types of array [27]. Fig. 6 shows an example of a spherical array with 36 microphones placed on a sphere with a radius of 2 meters, illustrating the radiation pattern of the array.

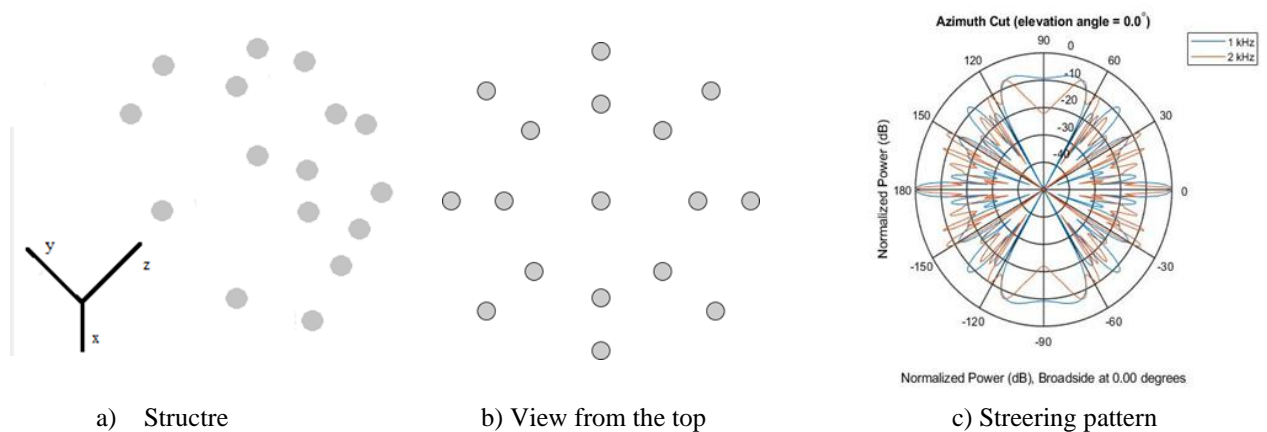


Fig. 5. Hemispherical array.

**3. SOURCE POSITIONING**

An audio camera is a microphone system that comprises a microphone array [28]. Each microphone in the array receives the sound produced by the source. Due to the geometric displacement between the microphones, the sound arrives at each microphone at different times, leading to a time delay between the signals recorded in the microphone

array. This time difference of arrival (TDOA) is used to identify the source position [29].

To determine the source position, changes are made to the microphone's radiation pattern, a process called beamforming. Beamforming is a signal processing technique that enables the localization of the sound source. In general, sound source localization involves more complex calculations compared to the localization of radio or optical frequencies, but it can be achieved with cheaper equipment. Fig. 7 depicts a sound collection system that amplifies the target sound using the delay-and-sum method while suppressing environmental noise without introducing a delay. Fig. 8 shows the received sound patterns of each microphone based on their angle and location.

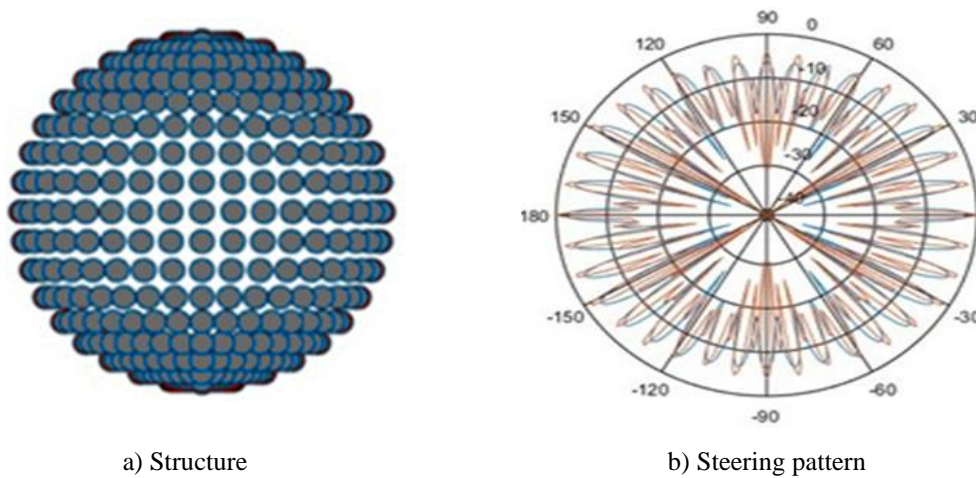
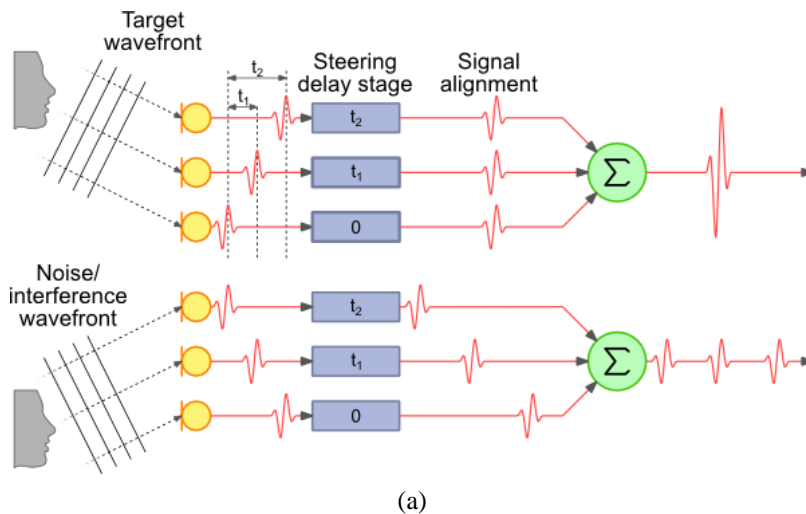


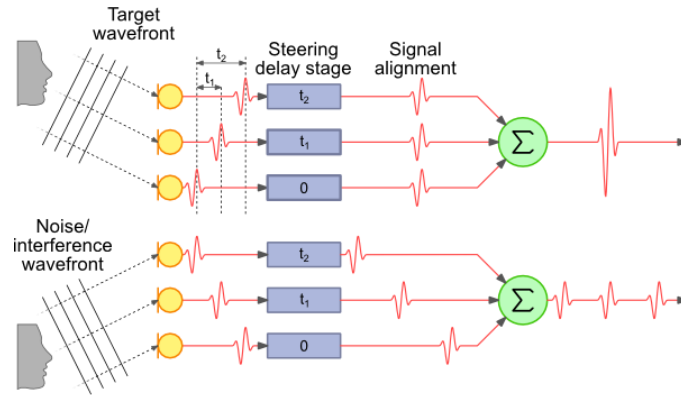
Fig. 6. Spherical array.

To determine the position of the audio source, we use a two-step algorithm as follows.

1) For broadband signals, many well-known algorithms, such as the Capon or MUSIC method, cannot be used because they use the phase difference between elements, which is only applicable for narrow-band signals. In the case of broadband signals, instead of phase information, the difference in signal arrival time between microphones can be used. In this research, we use the generalized cross-correlation algorithm using phase transformation (GCC-PHAT) to calculate the arrival time differences.

2) We calculate the position of the source by triangulation method. For this purpose, first, straight lines are drawn from the microphones along the directions of arrival. Then, the intersection of these lines is determined as the source location.





(b)

Fig. 7. The sum system of the received sounds; (a) Using delay; (b) Without delaying the sounds.

Assume that the microphones are located at two-dimensional coordinates (0,0) and (L, 0) and the unknown source is located at (X,Y).

Based on Fig. 9, the distance between two microphones can be obtained using equation (3) [28].

$$L = Y \tan \theta_1 + Y \tan \theta_2 \tag{3}$$

In this way, the values of Y and X are calculated using equations (4) and (5) [28]:

$$Y = L / (\tan \theta_1 + \tan \theta_2) \tag{4}$$

$$X = Y \tan \theta_1 \tag{5}$$

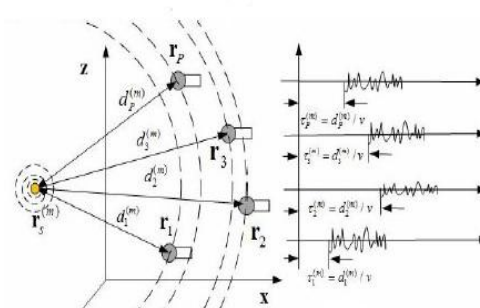


Fig. 8. Sound reception delay of each microphone based on position.

#### 4. THE PROPOSED SYSTEM

This section focuses on the proposed system and the resulting sound source positioning accuracy achieved using the three-dimensional microphone array and its unique structure, which does not have any frequency restrictions. The accuracy of the proposed system is very high, and it provides a robust and reliable method for sound source localization in various domains.

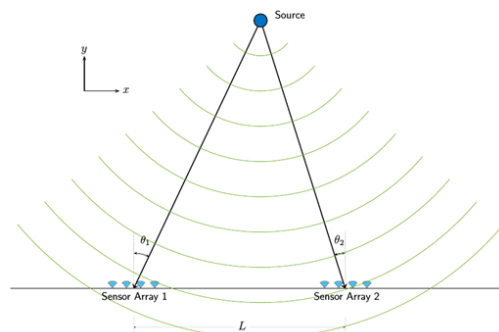


Fig. 9. Propagation of the sound source waves.

#### 4.1. Proposed 3D array

This section presents a novel three-dimensional array structure and assesses its properties. Specifically, the proposed array's microphone placement was optimized via a genetic algorithm in three-dimensional space to enhance sound source localization accuracy at distances ranging from 52 to 402 meters for military and security applications. The optimization process aimed to augment spatial coverage across various angles while amplifying received sound.

#### 4.2. Genetic Algorithm

This research employed the Genetic Algorithm (GA) to optimize the placement of microphones in an array for improved sound source localization. GA was selected for its ability to navigate a vast solution space and identify optimal solutions. GA was implemented to generate a range of candidate solutions for the microphone array's placement, and each solution was evaluated using an objective function that quantified the accuracy of sound source localization. The optimal microphone array configuration was then identified as the best solution. The findings indicate that the GA-optimized microphone array outperformed traditional methods, such as random placement and uniform spacing.

The pseudocode described in Algorithm 1 is presented to optimize the microphone placement in the schematic of our proposed microphone array.

**Algorithm 1.** Pseudocode to optimize the position of microphones in the proposed microphone array.

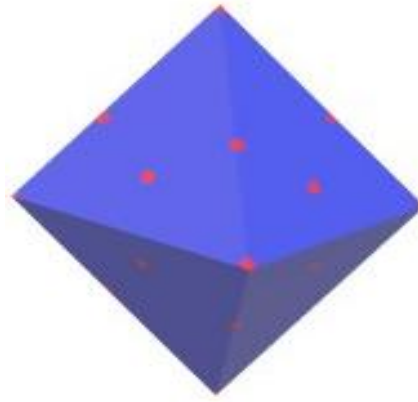
1. Define the objective function  $f$  to evaluate the quality of the microphone array.
2. Define the population size  $N$ , maximum number of generations  $G$ , and mutation rate  $p_m$ .
3. Initialize the population of candidate solutions  $X = \{x_1, x_2, \dots, x_N\}$  with random microphone positions.
4. Evaluate the fitness of each candidate solution using the objective function:  $f(x_i)$  for  $i = 1$  to  $N$ .
5. Repeat for a set number of generations:
  - a. Select the best individuals for reproduction based on fitness using tournament selection:
    - i. Randomly select two individuals from the population.
    - ii. Choose the individual with the higher fitness to be a parent.
    - iii. Repeat steps i and ii to select a second parent.
    - iv. Apply crossover operator to create new offspring.
  - b. Apply crossover operator to create new offspring:
    - i. Randomly select a crossover point  $k$  between 1 and the number of microphones  $M$ .
    - ii. Create a new offspring by swapping microphone positions after the crossover point.
  - c. Apply mutation operator to randomly modify offspring:
    - i. Randomly select a microphone position to mutate.
    - ii. Perturb the position by adding a normally distributed random value with mean 0 and standard deviation  $\sigma = 1$  multiplied by the mutation rate  $p_m$ .
  - d. Evaluate the fitness of new offspring using the objective function:  $f(x_i)$  for  $i = 1$  to  $N$ .
  - e. Replace the worst individuals in the population with the new offspring:
    - i. Select the two worst individuals in the population.
    - ii. Replace the worst individual with the best offspring.
    - iii. Replace the second-worst individual with the second-best offspring.
6. Return the best candidate solution found during the optimization process:  $\text{argmax}(f(x_i))$  for  $i = 1$  to  $N$ .

Fig. 10 displays the outcome of the proposed three-dimensional array model's design. The array structure comprises two pyramids with identical sections, aligned in a mirror-like fashion.

#### 4.3. Evaluation of the Sound Matrix

Following the design of the proposed array structure, we examined and analyzed sounds received from the microphones to identify the source's location.

The sound source's location is represented as  $(x_1, y_1, z_1)$ , the center of the array as  $(x_2, y_2, z_2)$ , and each microphone's location as  $(x_i, y_i, z_i)$ .



**Fig. 10.** Proposed 3D microphone array.

Equations (6) and (7) describe the pseudo-three-dimensional distance between the sound source's position and the microphones and the center of the microphone array in the two-dimensional x-z plane, respectively.

$$R_{1a} = \sqrt{((x, k_{a2}) - x_i)^2 + y_i^2 + ((z, k_{a1}) - z_i)^2} \quad (6)$$

$$R_{2a} = \sqrt{((x, k_{a2}) - x_2)^2 + y_2^2 + ((z, k_{a1}) - z_2)^2} \quad (7)$$

Where:

$$k_{a1} \in \{1, 1+\gamma, 1+2\gamma, \dots, z_1\}, k_{a2} \in \{1, 1+\gamma, 1+2\gamma, \dots, x_1\}$$

specify the amount of displacement in the z and x axes, respectively. In this way, by considering the difference of the above values, the sound intensity can be obtained based on the equation (8).

$$b_a = e^{-jw_n(k)f_d R_a/c} \sqrt{a^2 + b^2} \quad (8)$$

where  $R_a = R_{1a} - R_{2a}$ , c is the speed of sound,  $w_n(k)$  is the wave equation based on the angular frequency, and  $f_d$  is the amplification factor of the system. In this way, using relation (9), the sound measurement matrix can be obtained in the specified scale.

where  $R_a = R_{1a} - R_{2a}$ , c is the speed of sound,  $w_n(k)$  is the wave equation based on the angular frequency, and  $f_d$  is the amplification factor of the system. In this way, using relation (9), the sound measurement matrix can be obtained in the specified scale.

$$P(k_{a1}, k_{a2}) = |b_a \times R_a \times b_a'| \quad (9)$$

Utilizing this relation, the P matrix represents the noise measurement matrix in the x-z plane, where each value in the matrix's rows and columns indicates the received sound power according to a specified scale. This matrix can be interpreted as a grayscale image pattern, where each layer represents the sound intensity in that part of the screen. The maximum value in the matrix corresponds to the point where the maximum sound occurred based on the specified scale. Subsequently, the three-dimensional equation (10) employs the obtained results to determine the exact coordinates of the target point with high precision.

$$R_{3a} = \sqrt{((x, k_{a2}) - x_i)^2 + ((y, k_{a3}) - y_i)^2 + ((z, k_{a1}) - z_i)^2} \quad (10)$$

Where:

$$k_{a1} \in \{1, 1+\gamma, 1+2\gamma, \dots, z_1\},$$

$$k_{a2} \in \{1, 1+\gamma, 1+2\gamma, \dots, x_1\},$$

$$k_{a3} \in \{1, 1+\gamma, 1+2\gamma, \dots, y_1\}$$

Similarly, in equation (11), the three-dimensional distance of the microphone array center from the source location is obtained.

$$R_{4a} = \sqrt{((x.k_{a2}) - x_2)^2 + ((y.k_{a3}) - y_2)^2 + ((z.k_{a1}) - z_2)^2} \quad (11)$$

Based on this, similar to equation (9), the sound measurement matrix can be accurately obtained using relation (12).

$$P(k_{a1}, k_{a2}, k_{a3}) = b_a \times R_{a2} \times b_a' \quad (12)$$

where  $R_{a2} = R_{3a} - R_{4a}$ . In this way, P is the sound measurement matrix in x, y and z plane, which determines the maximum sound received in this plane.

To enhance the usability of the proposed algorithm, a maximization filter is applied to the matrix. This filter identifies the maximum value in each row and column, sets the maximum value to 1, and zeroes out the remaining values. Consequently, the precise location of the target point can be determined using the binary matrix presented in equation (13).

$$ZO(\mathbf{W}) = (x_m, y_m, z_m) = \max_x \left( \max_y \left( \max_z (\mathbf{W}) \right) \right) \quad (13)$$

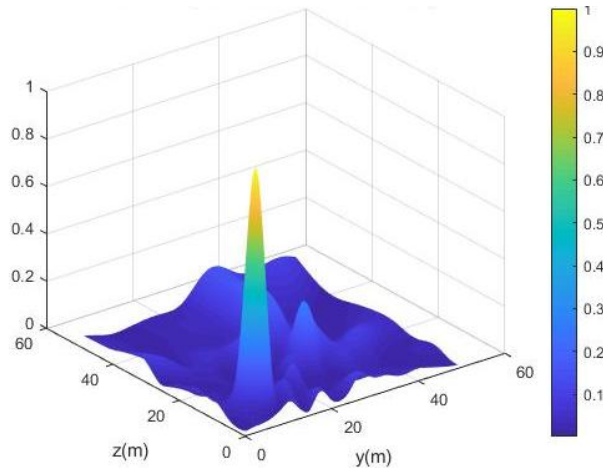
In which, W is the matrix resulting from the three-dimensional positioning of the source and the resulting matrix of zero and one, only its maximum dimension is equal to one and the rest of the elements are equal to zero.

## 5. RESULTS

In this section, we examine the results obtained from the implementation of the proposed algorithm and compare the results with similar works.

### 5.1. Preliminary 3D Array Results

In this section, we use the proposed 3D array to locate the sound source and we use the 3D space equations that were introduced in the previous section. To track distant sound sources for military and security applications, we first position the sound source on the three-dimensional coordinate plane at (10, 10, 10) meters from the center of the array, which is equivalent to a distance of 52 meters. To enhance tracking accuracy, we set the evaluation step to 0.01 meters. Subsequently, we evaluate the performance of the proposed system by varying the source's position and frequency and analyzing the results of the proposed algorithm's sound source localization. Figs. 11 and 12 illustrate some simulation results for varying the distance and frequency components of the source.



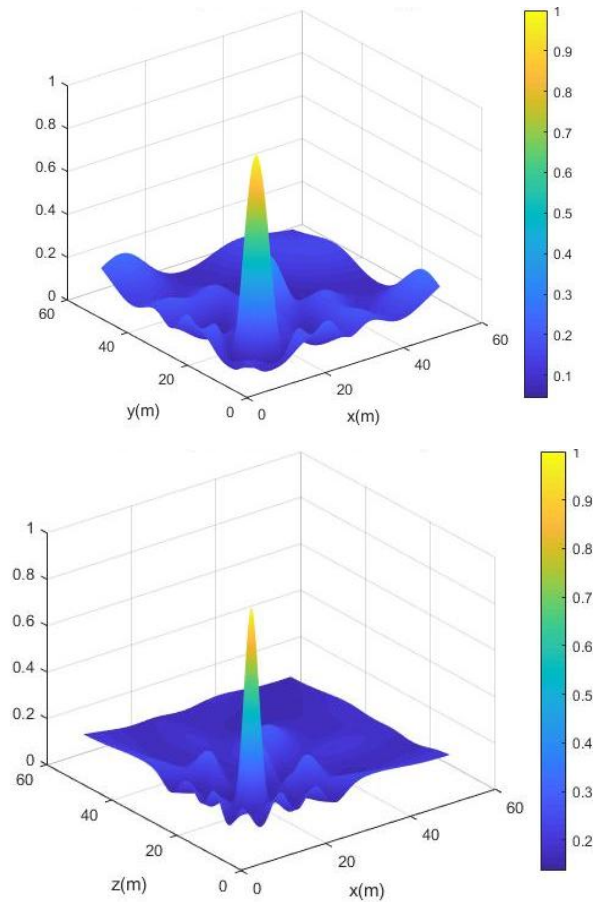


**Fig. 11.** 3D-localization of a 50 Hz sound source located at (10, 10, 10) using the proposed system.

Fig. 11 demonstrates the capability of the proposed system to determine the precise location of a sound source based on the received sound's intensity. However, some regions with strong noise could indicate potential errors in sound source detection. Another observation from the presented images is that as the distance between the source and the array increases, the localization error increases due to the impact of noise and the reduction in signal-to-noise ratio (SNR). The next section will examine the results of incorporating the proposed system, including the input signal amplifier equation, to evaluate the three-dimensional positioning of the sound source using the binary matrix.

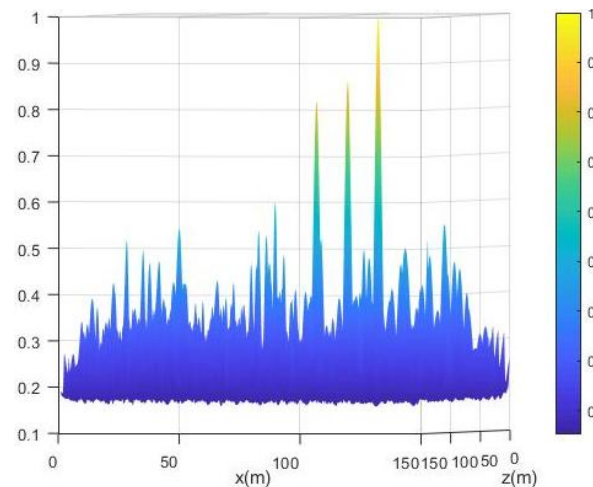


**Fig. 12.** Localization of a 1 kHz sound source located at (100, 120, 130) using the proposed system.

## 5.2. Proposed 3D Array System with Gain Coefficients

To evaluate the effectiveness of the amplification factor in enhancing the proposed system's performance, we conducted the following experiments. As previously mentioned, the distance of the sound source from the microphone array and the low frequency of the source signal are two significant factors that contribute to errors in sound source localization. In this section, we simulated these two factors in two experiments, depicted in Fig. 13. Specifically, we set the frequency of the sound source to 20 Hz and 100 Hz in the respective experiments and positioned it at (75, 70, 60) meters and (130, 120, 100) meters in the (x, y, z) space, respectively.

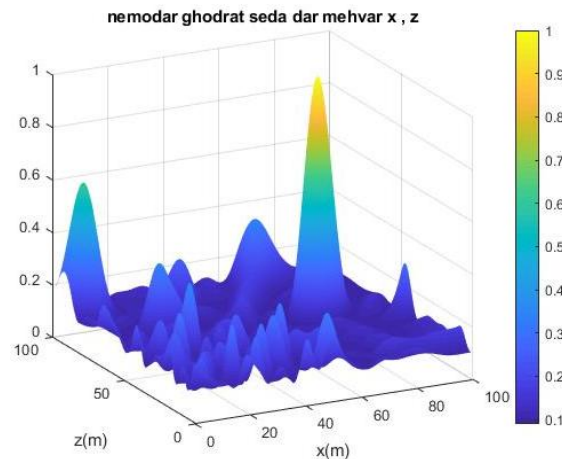


**Fig. 13.** Localization of a 20 Hz sound source located at (60, 75, 70) (in the x-z plane) using the amount of received sound power in the proposed 3D array with the amplification factor of the system.

The above results demonstrate that the proposed enhanced system can accurately locate a sound source with a frequency of 20 Hz at a distance where previous algorithms utilizing stronger frequencies experienced significant errors. Hence, it can be concluded that the proposed system is effective in identifying the sound source's position even at challenging distances and low frequencies.

## 5.3. Results of the Applying Zero and One Matrix

In addition to the amplifier system's contribution to enhancing sound source localization accuracy, this section presents the application of the zero and one filters on the system's output. These filters isolate the primary response, representing the sound source's location, while suppressing various visual disturbances and noises that may cause errors in determining the sound source's position.

The component matrix of the received sound power, obtained by analyzing equations (6-9), is based on the three-dimensional coordinate axis scale and a specific pitch, which indicates the received sound's power at each point with a specific pitch. The highest value in this matrix, located in a specific row and column, corresponds to the received sound power of the sound source. Therefore, this position is related to the source's x and y coordinates, which are represented in the first matrix. Using the position of the received sound power and the combination of the y position in this matrix with the highest value's position in the x and z plane, we can determine the sound source's precise location. This approach enables us to analyze the three-dimensional position of the surrounding space using only two matrices, which results in high accuracy and requires less time for analysis than traditional three-dimensional equations. We will elaborate on this approach in the next section.

In this experiment, we examine an example to illustrate the sound source's three-dimensional position. The sound source's position on the (x, y, z) coordinate axis is set at (72, 94, 30) for a 50 Hz source, and the range of 1 to 200 is monitored with a step of 0.1, as in previous experiments. Fig. 14 displays the sound source's position after applying the zero and one filter, which isolates the source's position while removing other noises and disturbances. Fig. 15 depicts the sound source and existing microphones on the array.

## 6. COMPARISON OF THE RESULTS

To evaluate the proposed algorithm's performance, we placed a 50 Hz sound source at the coordinates (30, 30, 30) and examined three modes: two-dimensional array, three-dimensional array, and three-dimensional array with the system amplification factor. The results of this comparison are presented in the figure, where the yellow area represents

the system's output in detecting the sound source's position. As shown, the proposed algorithm significantly reduces the probability of error, although some residual local noises still affect the sound source's position. To address this issue and determine the sound source's precise location, we applied the proposed zero and one filter to the three output matrices of the proposed algorithm. Each matrix examines the sound source's position in two dimensions (x-y, x-z, and y-z matrices). This approach enabled us to identify the sound source's exact three-dimensional position.

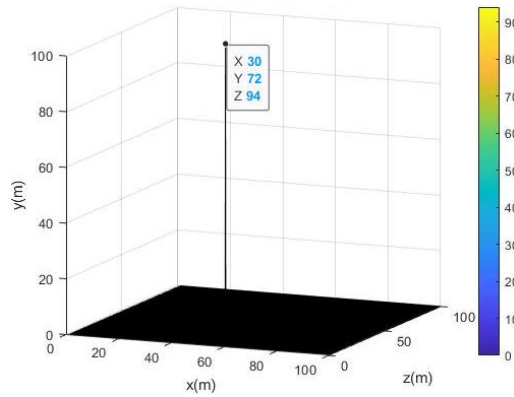


Fig. 14. Sound source position localization using the proposed method boosted by the zero and one matrix.

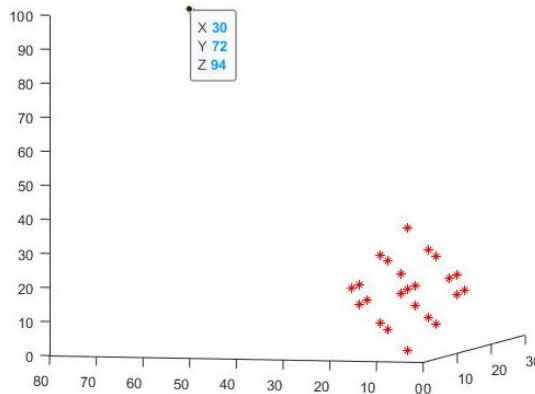
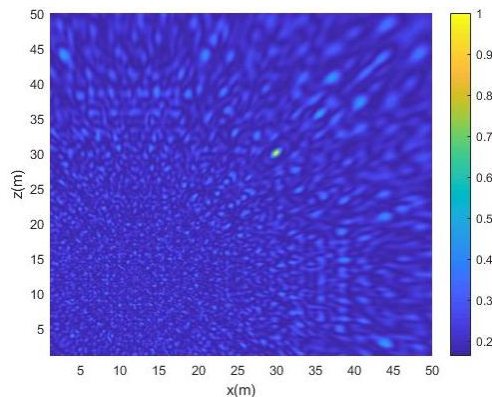
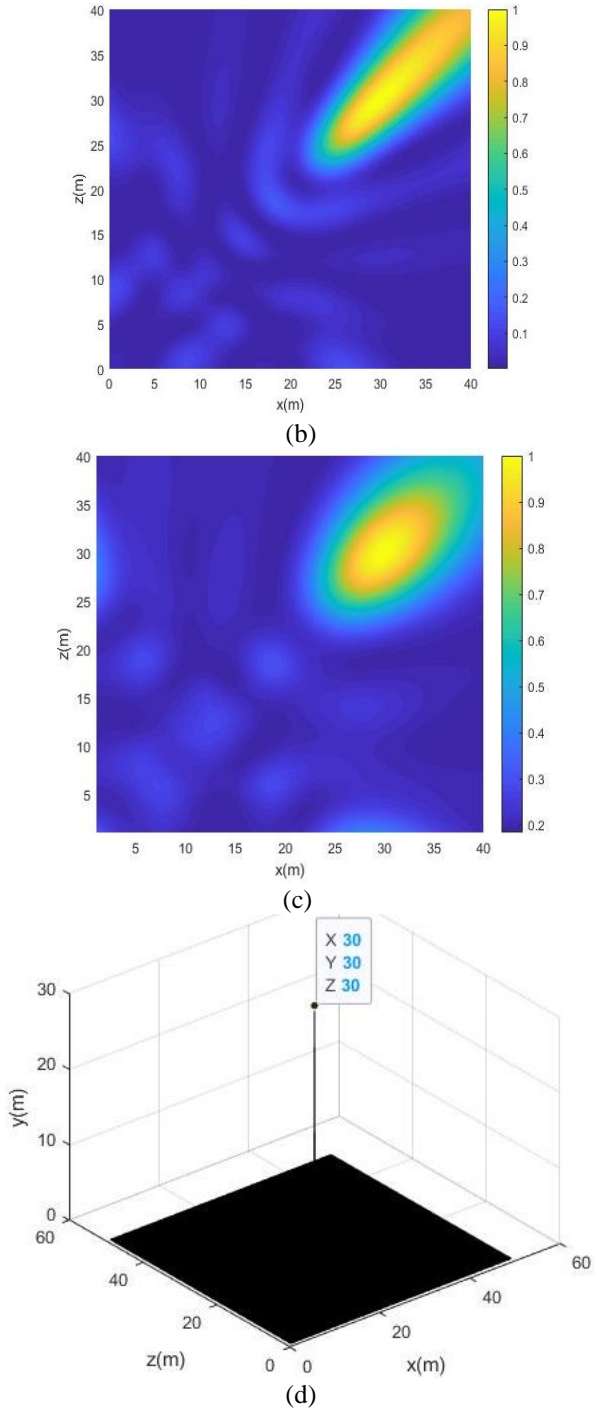


Fig. 15. Location of the sound source and the 3D microphone array.

The comparison tables of the results were designed based on the Euclidean distance pattern to demonstrate that the proposed system, which can amplify the received signal, enhances the accuracy of sound source identification compared to similar systems. We performed 160 tests for both near and far distances. Specifically, we conducted 80 tests on the first system without considering the signal amplification and the other 80 tests on the amplified system. The experiments also encompassed signals with frequencies of 20, 50, 100, 1K, 5K, 10K, 100K, and 1M Hz. Tables (1) and (2) present the results of these tests.



(a)



**Fig. 16.** Comparison of sound source positioning at 50 Hz using four structures (a) 2D array; (b) 3D array; (c) 3D array by applying the system amplification factor (proposed method 1); (d) 3D array by applying amplification factor and implementing zero and one filter on the output matrices (proposed method 2).

**Table 1.** Error percentage in locating the sound-source position using the delay and sum system without signal amplification.

		Sound source position $\begin{bmatrix} x \\ y \\ z \end{bmatrix}$ (in meters)									
		30	50	50	70	90	110	110	170	200	210
		30	50	60	80	100	130	140	145	210	240
		30	50	70	90	110	140	170	190	230	250
Sound source frequency (Hz)	20	37%	43%	47%	50%	57%	64%	68%	75%	80%	84%
	50	36%	41%	45%	48%	54%	61%	65%	72%	76%	80%
	100	33%	37%	41%	44%	50%	56%	60%	66%	70%	74%
	1K	26%	29%	34%	35%	41%	47%	50%	56%	59%	63%
	5K	23%	25%	29%	31%	36%	42%	45%	49%	53%	57%
	10K	20%	22%	26%	27%	31%	37%	40%	43%	47%	51%
	100K	17%	17%	24%	25%	28%	29%	32%	34%	38%	42%
1M	10%	19%	22%	24%	26%	27%	27%	29%	30%	31%	

**7. CONCLUSION**

In order to solve the distant sound source localization problem, this article explores various arraying methods and signal analysis techniques. By combining the advantages of each of these methods and providing an efficient microphone arrangement pattern, we propose a new method for accurately identifying the sound source's position based on the evaluation of received signals. To this end, we design an array structure comprising 23 microphones arranged in an octagonal pattern and two pyramids whose cross-sectional surfaces are stacked. Additionally, we introduce a delay and weighted summation system to improve signal analysis and increase the proposed system's positioning accuracy. By considering the wave equations, we present equations to strengthen the proposed system, which enhance the positioning accuracy for both clean and noisy signals and increase the speed of 3D processing calculations for sound source location. Finally, we apply a digital filter to the system's output, enabling us to determine the sound source's position with high accuracy.

**Table 1.** Error percentage in locating the sound-source position using the proposed delay and sum system with signal amplification and zero and one filter.

		Sound source position $\begin{bmatrix} x \\ y \\ z \end{bmatrix}$ (in meters)									
		30	50	50	70	90	110	110	170	200	210
		30	50	60	80	100	130	140	145	210	240
		30	50	70	90	110	140	170	190	230	250
Sound source frequency (Hz)	20	4%	7%	8%	9%	11%	11%	12%	13%	13%	15%
	50	3%	6%	6%	7%	9%	10%	10%	11%	12%	13%
	100	2%	4%	5%	6%	8%	9%	8%	9%	9%	12%
	1K	<1%	2%	4%	5%	7%	8%	6%	7%	8%	11%
	5K	<1%	<1%	2%	3%	5%	6%	5%	6%	6%	9%
	10K	0	<1%	1%	2%	4%	4%	4%	5%	5%	8%
	100K	0	0	<1%	1%	2%	3%	4%	5%	5%	7%
1M	0	0	0	<1%	<1%	1%	3%	4%	4%	5%	

## REFERENCES

- [1] Z. Wang, D. Hu, Y. Zhao, Z. Hu, and Z. Liu, "Real-Time Passive Localization of TDOA via Neural Networks," *IEEE Communications Letters*, 25(10), 3320-3324, 2021, doi: 10.1109/LCOMM.2021.3097065.
- [2] F. Ge and Y. Shen, "Single-Anchored Ultra-Wideband Localization System Using Wrapped PDOA" *IEEE Transactions on Mobile Computing*, vol. 21, no. 12, pp. 4609-4623, Dec. 2022, doi: 10.1109/TMC.2021.3083613.
- [3] A. Ishfaq and B. Kim, "Real-Time Sound Source Localization in Robots Using Fly Ormia Ochracea Inspired MEMS Directional Microphone," *IEEE Sensors Letters*, vol. 7, no. 1, pp. 1-4, Art no. 6000204, Jan. 2023, doi: 10.1109/LSENS.2022.3231595.
- [4] W. Li, B. Tian, Z. Chen and S. Xu, "Regularized Constrained Total Least Squares Source Localization Using TDOA and FDOA Measurements," in *IEEE Geoscience and Remote Sensing Letters*, vol. 21, pp. 1-5, 2024.
- [5] X. Li, Y. Wang, B. Qi and Y. Hao, "Long Baseline Acoustic Localization Based on Track-Before-Detect in Complex Underwater Environments," in *IEEE Transactions on Geoscience and Remote Sensing*, vol. 61, pp. 1-14, 2023.
- [6] P. Kim, J.H. Song, and T.-K. Song, "A new frequency domain passive acoustic mapping method using passive Hilbert beamforming to reduce the computational complexity of fast Fourier transform," *Ultrasonics*, vol. 102, pp. 106030, 2020, doi: 10.1016/j.ultras.2019.106030.
- [7] A. Pawlak, H. Lee, A. Mäkivirta and T. Lund, "Spatial Analysis and Synthesis Methods: Subjective and Objective Evaluations Using Various Microphone Arrays in the Auralization of a Critical Listening Room," in *IEEE/ACM Transactions on Audio, Speech, and Language Processing*, vol. 32, pp. 3986-4001, 2024.
- [8] B. Laufer-Goldshtein, R. Talmon, and S. Gannot, "Audio source separation by activity probability detection with maximum correlation and simplex geometry," *Journal of Audio, Speech, and Music Processing*, vol. 5, 2021, doi: 10.1186/s13636-021-00195-7.
- [9] K. J. Haworth, N. G. Salido, M. Lafond, D. S. Escudero and C. K. Holland, "Passive Cavitation Imaging Artifact Reduction Using Data-Adaptive Spatial Filtering," in *IEEE Transactions on Ultrasonics, Ferroelectrics, and Frequency Control*, vol. 70, no. 6, pp. 498-509, June 2023.
- [10] S. Grubesa, J. Stamac, I. Krizanic, and A. Petosic, "The Development and Analysis of Beamforming Algorithms Used for Designing an Acoustic Camera," *American Journal of Environmental Science and Engineering*, vol. 3, no. 4, pp. 94-102, 2019, doi: 10.11648/j.ajese.20190304.11.
- [11] F. Höflinger, R. Zhang, J. Hoppe, A. Bannoura, L. M. Reindl, J. Wendeberg, M. Bühner, and C. Schindelbauer, "Acoustic self-calibrating system for indoor smartphone tracking (assist)," in *2012 International Conference on Indoor Positioning and Indoor Navigation (IPIN)*, pp. 1-9, 2012, doi: 10.1109/IPIN.2012.6396478.
- [12] T. Ying, W. Kang, and X. Hou, "Use of Digital Radio Mondiale Broadcasting Signal as an Illuminator of Opportunity for Passive Detection," in *2021 14th International Congress on Image and Signal Processing, BioMedical Engineering and Informatics (CISP-BMEI)*, pp. 1-4, 2021, doi: 10.1109/CISP-BMEI53629.2021.
- [13] Z. Ruili, Z. Rong, M. Jianmin, and D. Lei, "Research on noise locating of diesel engine block based on microphone array," in *2018 Chinese Control and Decision Conference (CCDC)*, pp. 6610-6613, 2018, doi: 10.1109/CCDC.2018.8408031.
- [14] M.-A. Chung, H.-C. Chou, and C.-W. Lin, "Sound Localization Based on Acoustic Source Using Multiple Microphone Array in an Indoor Environment," *Electronics*, vol. 11, no. 6, p. 890, 2022, doi: 10.3390/electronics11060890.
- [15] S. M. Abel, S. Boyne, and H. Roesler-Mulrone, "Sound localization with an army helmet worn in combination with an in-ear advanced communications system," *Noise Health*, vol. 11, pp. 199-205, 2009, doi: 10.4103/1463-1741.56213.
- [16] D. Thompson and L. Harkom, "Application of Acoustic Cameras to Measurement and Tuning of an Orchestra Rehearsal Room," in *Proceedings of the International Symposium on Room Acoustics: 15 to 17 September 2019 in Amsterdam, Netherlands*.
- [17] M. U. Liaquat, H. S. Munawar, A. Rahman, Z. Qadir, A. Z. Kouzani, and M. A. P. Mahmud, "Localization of Sound Sources: A Systematic Review," *Energies*, vol. 14, no. 13, 2022.
- [18] L. Y. Cheung, R. Kwan, and D. B. K. Yeung, "The Use Of Acoustic Cameras In Assisting The Testing Of Baffle-type Acoustic Windows And Balconies," in *INTER-NOISE and NOISE-CON Congress and Conference Proceedings*, vol. 259, no. 6, pp. 3898-3904, 2018.
- [19] N. M. Ortiz, S. Barré, and B. Vonnrhein, "The Acoustic Camera as a valid tool to gain additional information over traditional methods in architectural acoustics," *Energy Procedia*, vol. 78, pp. 122-127, 2015.
- [20] S. Suwanasri, W. Khetcharoen, T. Suwanasri, N. Panmala, S. Rungsivattagapong, N. Atiwet, and P. Poonpoch, "Partial Discharge Investigation and Failure Analysis on Distribution Network Using Acoustic Camera," in *2021 9th International Electrical Engineering Congress (iEECON)*, pp. 181-184, 2021.
- [21] J. Pihera, J. Hornak, P. Trnka, O. Turecek, L. Zuzjak, K. Saksela, J. Nyberg, and R. Albrecht, "Partial discharge detection using acoustic camera," in *2020 IEEE 3rd International Conference on Dielectrics (ICD)*, pp. 830-833, 2020.
- [22] G. Liu, S. Yuan, J. Wu, and R. Zhang, "A Sound Source Localization Method Based on Microphone Array for Mobile Robot," in *2018 Chinese Automation Congress (CAC)*, pp. 1621-1625, 2018.
- [23] Y. Wang, Y. Ji, D. Liu, Y. Tamura, H. Tsuchiya, A. Yamashita, and H. Asama, "Acmarker: Acoustic camera-based fiducial marker system in underwater environment," *IEEE Robotics and Automation Letters*, vol. 5, no. 4, pp. 5018-5025, 2020.
- [24] K. Tsutsumi, K. Mizuno, and H. Sugimoto, "Accuracy enhancement of high-resolution acoustic mosaic images using positioning and navigating data," in *Global Oceans 2020*, Singapore – U.S. Gulf Coast, Biloxi, MS, USA, pp. 1-4, IEEE, 2020, doi: 10.1109/IEEECONF38699.2020.9389082.
- [25] G. Huang, J. Benesty, I. Cohen, and J. Chen, "A Simple Theory and New Method of Differential Beamforming with

- Uniform Linear Microphone Arrays,”** *IEEE/ACM Transactions on Audio, Speech, and Language Processing*, vol. 28, pp. 1079-1093, 2020, doi: 10.1109/TASLP.2020.2983894.
- [26] R. Wang, BZ. Wang, C. Hu, et al., “Wide-angle scanning planar array with quasi-hemispherical-pattern elements,” *Scientific Reports*, vol. 7, p. 2729, 2017, doi: 10.1038/s41598-017-03005-3.
- [27] D. Khaykin and B. Rafaely, “Acoustic analysis by spherical microphone array processing of room impulse responses,” *The Journal of the Acoustical Society of America*, vol. 132, no. 1, pp. 261-270, 2012, doi: 10.1121/1.4726012.
- [28] J. Stamac, S. Grubesa, and A. Petosic, “**Designing the Acoustic Camera using MATLAB with respect to different types of microphone arrays,**” in *Second International Colloquium on Smart Grid Metrology, SMAGRIMET 2019*.
- [29] T.E. Tuncer and B. Friedlander, “**Classical and Modern Direction-of-Arrival Estimation,**” *Academic Press*, 2009.



# Design and Implementation of Smart Home Using ZigBee and Bluetooth

Mohammad Hoseini Behbahani<sup>1</sup>, Hossein Shamsi<sup>2</sup> 

- 1- Department of Electrical Engineering, K. N. Toosi University of Technology, Tehran, Iran.  
Email: maryamhb1998@gmail.com
- 2- Department of Electrical Engineering, K. N. Toosi University of Technology, Tehran, Iran.  
Email: shamsi@eetd.kntu.ac.ir (Corresponding author)

## ABSTRACT:

— In this paper, a smart home system is designed and implemented by using both ZigBee and Bluetooth technologies at 2.4 GHz frequency. It includes two hardware implementations and an android based application. The first hardware, which is called end device, employs the low power ZigBee standard and is installed on appliances, lightening system, cooling system, and etc to control them. The second hardware, called coordinator, employs both ZigBee and Bluetooth. There is only one coordinator in each home, which acts as an interface between the user and end devices. It communicates with end devices through ZigBee and with users cellphone through Bluetooth. In this smart home, the Zigbee and Bluetooth protocols are implemented by using CC2530 chip and HC05module, respectively. The smart home utilizes the star network topology. Once the user wants to control something, by using the user interface on his/her smart phone, the Bluetooth of the cellphone is enabled and a radio signal is sent to HC05 Bluetooth module. This module converts the wireless Bluetooth signal to the wired TTL signal and sends it through a cable to the coordinator. Corresponding to the received signal, the coordinator broadcasts ZigBee wireless signal in an 80 square meters house. All end devices receive coordinator's signal and consequently the relevant end device responds to the coordinator by sending an acknowledge and changing the lightening or cooling system status. In other words, each authorized cellphone can act like a remote control hardware. Furthermore, in this work, MAC address of the authorized cellphones is used for increasing the security.

**KEYWORDS:** ZigBee, CC2530, Bluetooth, Smart home, Smartphone, Android.

## 1. INTRODUCTION

Nowadays, energy management and renewable energies have become hot topics in electrical engineering because of the limited fossil fuels resources and environmental pollution due to the fossil-based fuels. Consequently, smart grids are developed [1], which are electricity network based on digital technology (two-way digital communication) used to supply electricity to consumers. This system allows for monitoring, analysis, control and communication within the supply chain to help improve efficiency, reduce energy consumption and cost, and maximize the transparency and reliability of the energy supply chain. The smart grid was introduced with the aim of overcoming the weaknesses of conventional electrical grids by using smart net meters. Smart homes are an important part of smart grids [2], [3]. Smart home employs sensors to gather data and then regarding to these data and inhabitant activities, the home is controlled. Smart home can improve consumer behavior, causing decline in consumption of energy [4].

Wireless Sensor Networks (WSNs) have very significant role in smart homes. Their operation is that they collect data from the medium and transmit these data wirelessly through the coordinating node. Regarding there is no wire so we don't face to mess the home because of wires and the cost also is reduced. Therefore it's a user-friendly technology

Paper type: Research paper

<https://doi.org/xxx>

Received: 16 February 2024; Revised: 23 May 2024; Accepted: 16 July 2024; Published: 1 March 2025

How to cite this paper: M. H. Behbahani, H. Shamsi, "Design and Implementation of Smart Home Using ZigBee and Bluetooth", *Majlesi Journal of Telecommunication Devices*, Vol. 14, No. 1, pp.19-29, 2025.

and it's easy to use. The smart home can be monitored either on mobile platforms or on web-based platforms [5]. In [6-13] a few novel researches on smart home are reported which highlight the importance of the subject.

One important issue about using WSNs is their energy consumption. Today, technology manufacturers have problems with the time that a battery can work before it needs to be recharged. Improving the batteries is a hard work and it costs a lot of money. So one of the big challenges about each system is the low power consumption. Since Wi-Fi is a power hungry technology, studies have been concentrated on ZigBee networks, which are low cost, energy-saving and high reliability. This technology also can be used in public places including schools, libraries and etc. [14-16]. ZigBee is based on IEEE802.15.4 standard and designed for small scale projects which need low-rate wireless connection. ZigBee operates in the ISM bands, 913 MHz, 868 MHz and 2.4GHz and the devices range is limited to 10-100 meters. It can be deployed with three topologies; star, tree and mesh and maximum number of nodes is 65k [17]. One of the problems that ZigBee networks has been faced to be used extensively was its coexistence with Wi-Fi. To solve this problem, contention resolution in time domain had been tested but the result was underutilization of frequency resources. But recently, new approaches such as COFFEE (Coexist Wi-Fi for ZigBee networks) has been adopted which provides appropriate conditions for an efficient coexistence [18]. Moreover, ZigBee has the advantage of being able to bridge between home control and other domains such as IEEE 11073 domain which includes Telehealth and Telecare [19]. Hence the functionality of in-home gateway can be increased.

Most of the previous works done on smart home are based on Wi-Fi and Bluetooth networks. Although these networks have their own merits, the problem is that they consume vast amounts of energy. Hence, in this paper the network has been designed based on ZigBee to reduce the energy consumption. Another issue in conventional smart homes is that they require a remote control hardware for taking the devices under control which led to the need for an extra hardware and therefore the increase in costs. In this paper, by providing an android based user interface application, the cell phone has been used as the remote control hardware. In addition to decreasing the costs, this approach causes the users' convenience. However, as a problem, the state-of-the-art cell phones do not support the ZigBee protocol. By employing the users' cell phone Bluetooth and a coordinator (router) in the home, we have solved this problem as shown in Fig.1. Each resident of the home communicates with the coordinator through his/her personal mobile Bluetooth and sends the command to turn off or turn on the desired device. After receiving the command, the coordinator broadcasts it in the home through ZigBee. In fact, the coordinator has both Bluetooth hardware and ZigBee hardware. All the end devices receive coordinator's signal, but only the desired end device sends the acknowledge and turns off or on according to the command. The end devices employ the low power ZigBee protocol and is installed on appliances, lightening system, cooling system, and etc to control them.

....The rest of this paper is organized as follows: section II reviews the ZigBee protocol and the ZigBee network topologies briefly. Section III describes the system implementation including the user interface software, home coordinator hardware and the end device hardware. The firmware is described in section IV. Test results are given in section V and finally the paper is concluded in section VI.

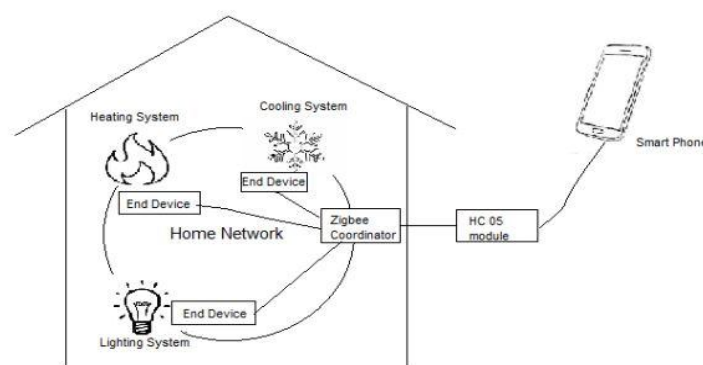


**Fig. 1.** Proposed smart home architecture.

## II. ZIGBEE PROTOCOL AND NETWORK TOPOLOGY

ZigBee protocol consists of four layers as follows [26]: application layer, network layer, MAC layer, PHY layer. The MAC and PHY layers are defined by IEEE802.15.4, while network and application layers are defined by ZigBee Alliance [27].

The PHY layer is responsible for physical channel data transmission and management, consisting of the synchronization header, the PHY header and the PHY service data unit. The synchronization header

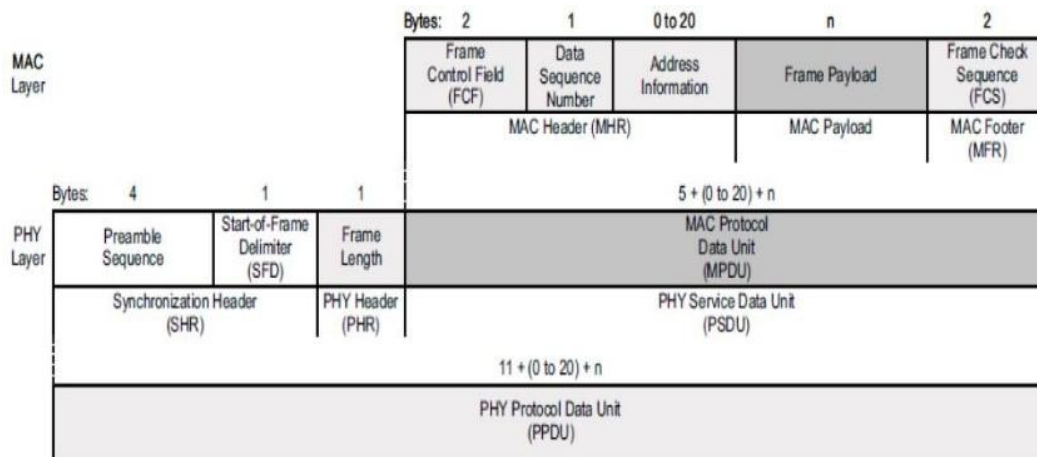


Fig. 2. Frame structure in IEEE 802.15.4 standard [28].

(SHR) consists of the preamble sequence followed by the start-of-frame delimiter (SFD). In the IEEE 802.15.4 specification [21], the preamble sequence is defined to be 4 bytes of 0x00. The SFD is one byte with value 0xA7. The PHY header consists only of the frame-length field. The frame-length field defines the number of bytes in the MAC protocol data unit (MPDU). The value of the frame-length field does not include the frame-length field itself. It, however, includes the frame-check sequence (FCS), even if this is inserted automatically by the hardware. The PHY service data unit (PSDU) contains MPDU. The function of the MAC layer is to generate or interpret the MPDU, and the radio has built-in support for processing of some of the MPDU subfields [20]. The network layer is responsible for establishment of topology and maintenance of network connections, as well as route discovery and route forwarding for equipment. Application layer is composed by the application support sub-layer (APS), ZigBee device configuration and user application layer. APS mainly provides ZigBee endpoint interface. ZigBee device configuration layer provides standard ZigBee configuration services. The user application is developed based on user’s needs [18]. ZigBee uses the IEEE 802.15.4 2003 specification for its physical and MAC layers. IEEE 802.15.4 offers star, tree, cluster tree, and mesh topologies; however, ZigBee supports only star, tree, and mesh topologies [22].

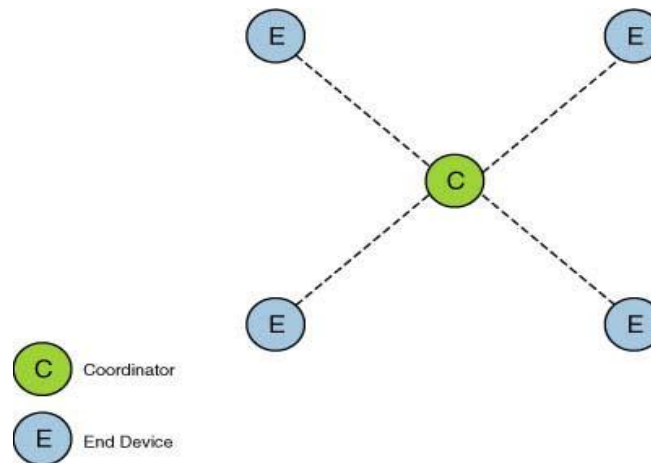
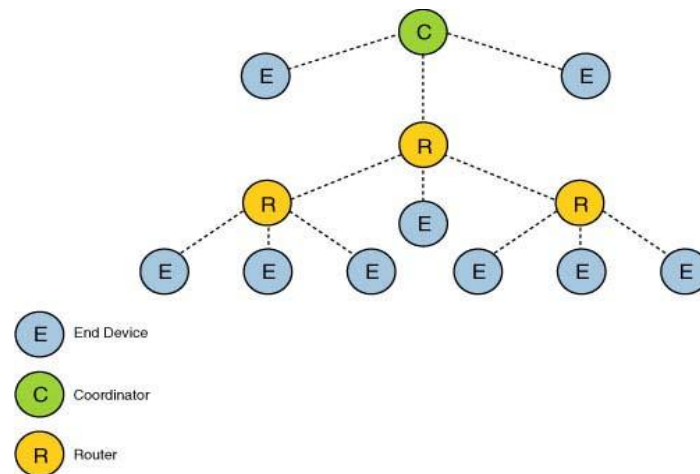


Fig. 3. Star topology [30].

**Star topology:** As shown in Fig. 2, the star topology consists of a coordinator and several end devices (nodes). In this topology end devices cannot communicate with each other directly. If they want to communicate, they first should communicate with the coordinator. So all the traffic goes through the coordinator. Therefore it can be a bottleneck for the network. If the coordinator is not in a working condition at any stage of operation, the performance of the network will be impaired. The advantage of star topology is that it is simple and easy to use.



**Fig. 4.** Tree topology [30].

**Tree topology:** In this topology, the network consists of a central node (root tree), which is a coordinator, several routers, and end devices, as shown in Fig. 3. Routers are used to extend the coverage of the network. The end nodes that are connected to the coordinator or the routers are called children. Only routers and the coordinator can have children. Therefore, they are the only devices that can be parents. An end device cannot have children and, therefore, may not be a parent. Each end device is only able to communicate with its parent (router or coordinator). In this technology, coordinator is at the highest level. If each message want to pass to the destination, it should go to the parents of destination node. So there is only one route for each message and it's not reliable [31].

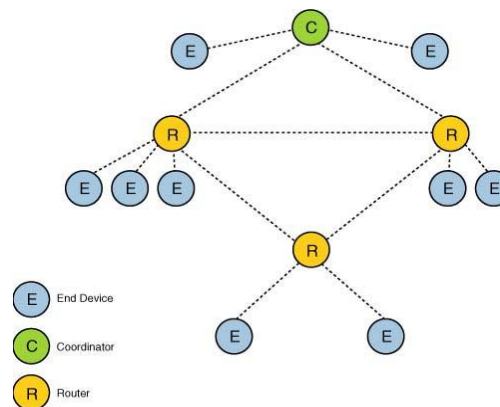


**Fig. 5.** Mesh topology [30].

**Mesh topology:** This topology is more flexible because there is more than one route for each message. If one path cannot pass the message, there is another path but the cost increases in this topology.

The star topology is mainly used in smart home, PC peripheral and so on. The tree topology is useful for mediocre networks in terms of coverage. The mesh topology applies to industrial control, logistics system and etc. [32]. The star network has the best performance regarding end-to-end delay, jitter and throughput [33]. We use star topology in this paper because in home there is no long distance and there are a few end devices. So there is no need for complexity of tree or mesh networks.

## 2. SYSTEM IMPLEMENTATION

The smart home implementation consists of three main subsystems. The first one is the user interface software. The software is an application that is written by android programming language. This application should be installed on the smart phone of each user. The application uses the phone Bluetooth. So it can connect to the HC05 Bluetooth module. HC05 module connects the first subsystem to the second one, coordinator. Coordinator and HC 05 module are connected to each other using TTL serial communication. The coordinator should be positioned in an appropriate place so that covers the whole house and all end devices. Coordinator communicates with end devices (third subsystem) by using

ZigBee. For each device that user wants to control, one end device is needed. In this work, a cost effective hardware is designed and implemented and tested for both coordinator and end devices. We used CC2530F256 in which both 8051 micro controller unit (MCU) and 2.4GHz IEEE802.15.4 compliant RF transceiver are integrated. This is called system on chip (SOC). Therefore there is no need for extra hardware. Hence, in addition to cost, circuit complexity and high frequency noises are also reduced.

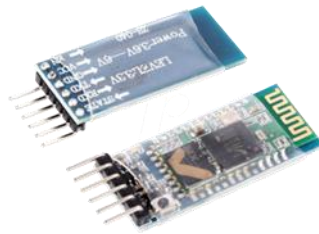
**User interface software:** By utilizing this application, users can control lighting, cooling system and other stuff in their house using their own smart phone. Moreover, they can monitor the status of equipment in their house like lighting system condition. Fig.s (6) and (7) show the windows of the provided user interface software. When users enter each section for the first time, they can see the former condition of each device, and then they can change them if they want to. In Fig. 7, the window relevant to the cooling system is shown.



Fig. 6. The main window of the provided user interface software.

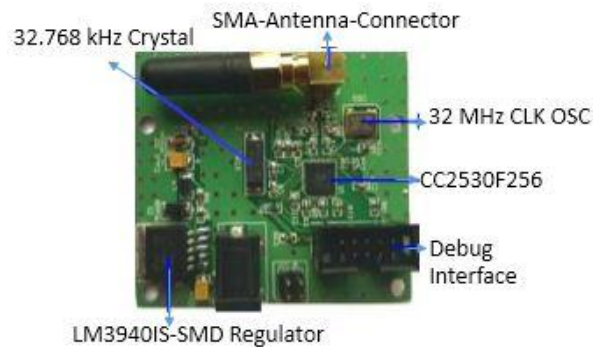


Fig. 7. The window relevant to the cooling system.



**Fig. 8.** HC05 Bluetooth module.

**HC05 Bluetooth module:** HC-05 module is a Bluetooth SPP (Serial Port Protocol) module. It can connect to the serial port of a microcontroller, which allows the microcontroller to communicate with other devices over a Bluetooth connection. It uses CSR Bluecore 04-External single chip Bluetooth system with CMOS technology and with AFH (Adaptive Frequency Hopping Feature) [34]. AFH helps to minimize the effects of interference with other devices. In Frequency Hopping technique when a link is formed, the devices are synchronized to change channels together many times a second. The pattern of channels used is called the hop sequence and is unique for each link. Since the devices spend only small amounts of time on a particular channel and because the hop sequence is different for each link the possibility of interference is minimized. HC05 can run in both master and slave modes. In this project it is used in slave mode, and its duty is to transfer data between the coordinator and cell phone. HC05 is connected through the UART to the CC2530F256 (coordinator). In other words, each user by enabling the Bluetooth of his/her own smart phone can connect to HC05, and consequently can indirectly transfer his/her own command to coordinator to control end devices. The printed circuit board (PCB) of the HC05 module is shown in Fig.8, where a microstrip antenna is utilized.



**Fig. 9.** Implemented coordinator hardware.

**Coordinator:** The main job of the coordinator is to receive the user's command from Bluetooth module and send it in the range of 80m for the end devices. Moreover, the coordinator should do the reverse; receives the response from end device and send it to Bluetooth module. The hardware of the coordinator (Fig. 9) includes a microprocessor and a 2.4GHz IEEE802.15.4 compliant RF transceiver integrated in a low-power single chip CC2530F256, a monopole 2.4GHz antenna, a voltage regulator and an oscillator.

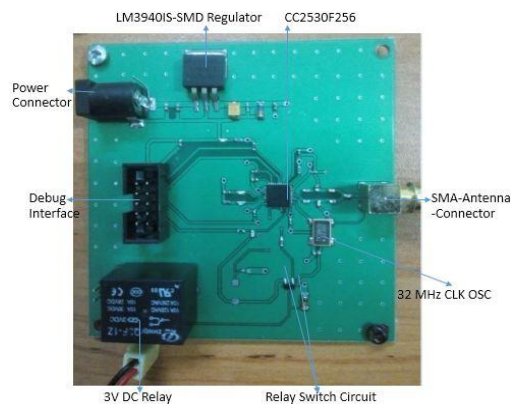


**Fig. 10.** Implemented end device hardware.

**End device:** An active end device (Fig. 10) is implemented for the proposed smart home. Hardware of the end device corresponds to that of coordinator. The only difference is that it has relay to provide enough current to control the devices. End device works at 2.4GHz and can sense different channels. It saves a lot of space in the hardware because of using SOC instead of separate MCU and RF transceiver. Each end device is attached to a device to control it. End device is waiting until it receives an input command. In this time, the end device switches to the sleep-mode by using the CC2530F256 ultra-low power sleep timer. This is an energy-efficient solution to decrease the end device power consumption while waiting for an incoming signal. At the sleep-mode, the digital voltage regulator is disabled. Neither the 32-MHz XOSC nor the 16-MHz RCOSC is running. SRAM and internal registers save their contents and 32.768 kHz XOSC and sleep timer are active. The system goes to the active mode on reset, an external interrupt, or when the Sleep Timer expires. The measurements shows that the designed active end device only consumes  $2.64\mu\text{W}$  in the sleep-mode, meanwhile 68mW power consumption is achieved in the active mode [20],[25].

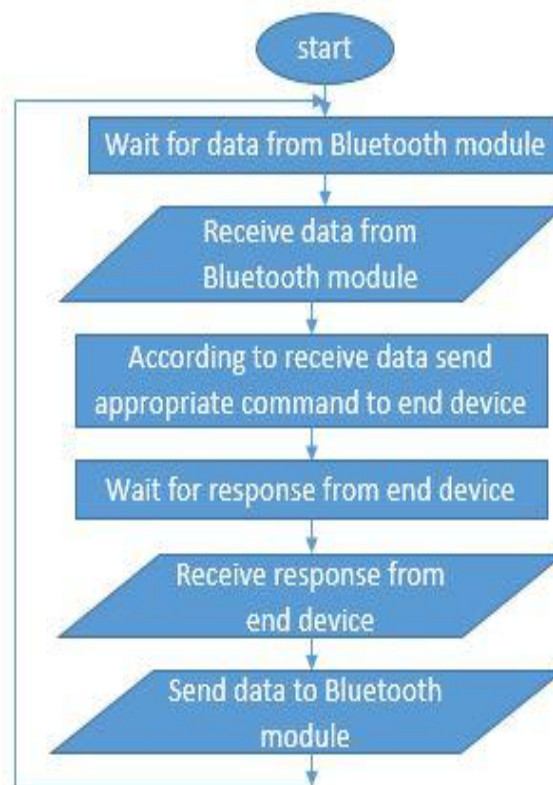


**Fig. 11.** Flow chart of the firmware programmed in the coordinator.

### 3. FIRMWARES

The whole flowchart of the firmware programmed in the coordinator is shown in Fig. 11. The coordinator waits for the user's command from the Bluetooth module. In this situation, the RF transceiver of the coordinator remains in the idle state to decrease the energy consumption. Each end device will have a unique identification number, and subsequently the user can search end devices by their unique IDs. When the user touches a button on the smart phone, the coordinator receives that message and then with respect to it, another message that contains the unique ID will be sent by the coordinator. At this moment every end devices receives the message and compares the ID with its own ID. If the ID is the same, then the end device controls the instrument, for example the lamp. The flowchart of the firmware programmed in end devices is shown in Fig. 12.

The pseudo code of the android application is as follows. This code is repeated for each section such as lighting, cooling and heating system.

If Bluetooth connection is established.

```

{
Buttons will be activated. (there is one button for each end device.)
Timer will be activated.

```

Command for checking current status will be sent and according to the received response, background image of buttons will be set.

```

}
Else {
Buttons will be deactivated.

```

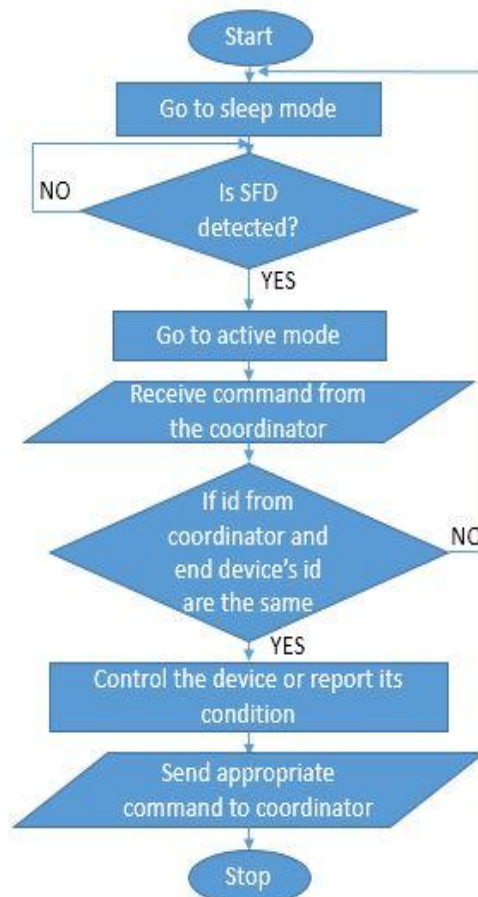


**Fig. 12.** Flow chart of the firmware programmed in the end device.

```

}
If user click each of the buttons
{
Command for changing status will be sent. (Also MAC Address will be sent for security reason.)
According to the received response, background image of button will be set.
}
If timer overflow occurs
{
Command for checking current status will be sent and according to the received response, background image of buttons will be set.
}
If error occurs in Bluetooth connection the user is notified to reestablish the connection.

```

**Network security:** Security should be considered in the link between coordinator and end devices and also in the link between smart phone and coordinator. Address is dedicated to coordinator and end devices. When they want to communicate with each other, transmitter sends a message containing its address and receiver's. Receiver check that message and if both addresses are correct the communication is established. Thus the link is only vulnerable if both addresses are leaked. To ensure the security of the link between smart phone, coordinator and authentication of the user, MAC address (Media Access Control address) is used. MAC address is a hardware identification number that uniquely

identifies each device on a network. It can be used as a network address in communications within a network. Each smart phone has its own MAC address. Therefore MAC address is used to secure the network. Smart phone sends its MAC address to coordinator and according to that coordinator checks if the smart phone is allowed to be part of the network otherwise the access is denied.

#### 4. TEST RESULTS

The proposed system is tested in an 80 square meters house and worked properly. Because of the fact that a ZigBee signal is weakened by hitting to the objects, it should be noticed that there are limitations for the distance that this system can cover. Consequently, in houses bigger than 80 square meters, there are blind spots and operation of the system will be disrupted. In this cases, router should be used to increase the coverage area. Also the reduction in energy consumption is considerable. Given the fact that lighting causes 25-50% of electricity consumption [35], even using the proposed system just for lighting section will help a lot in this regard.

In terms of coverage area, one vital parameter is RSSI (Received Signal Strength Indicator) which demonstrates input signal strength of receiver. RSSI should be higher than receiver sensitivity. For CC2530 chip, receiver sensitivity is -97 dBm [23]. RSSI varies depending on distance (between coordinator and end devices) and output signal strength of transmitter. It should be noticed that the more the output strength is, the more the total power consumption becomes. So for keeping the total power consumption down output signal strength will be adjusted according to the distance that should be covered. In Fig. 13, RSSI versus distance is depicted for two different amounts of output signal strength.

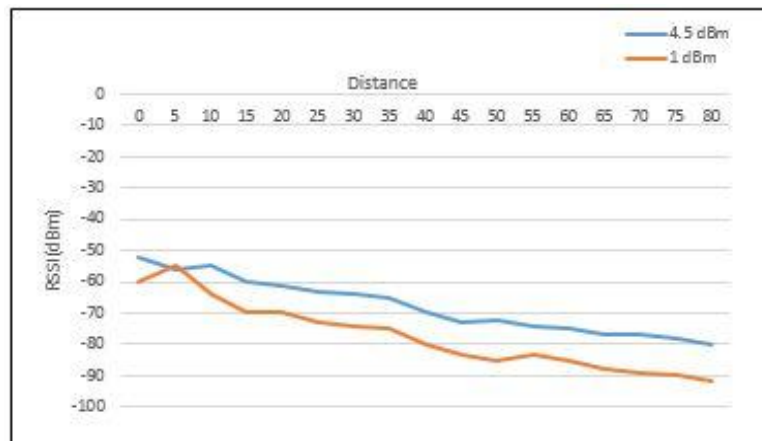


Fig. 13. Received signal strength (RSSI) versus distance.

Another crucial parameter is the PER (Packet Error Rate). It is stated in the form of percentage. The PER increased with increasing the distance, dramatically. The experiment was conducted for two different output powers as shown in Fig. 14.

#### 5. CONCLUSION

In this work, the required hardware and software for smart home is designed. The hardware is implemented by using the CC2530 chip, which is a low-power multi-purpose chip that integrates MCU and RF parts, leading to small dimensions for both coordinator and end device. Power consumption is an important issue and this problem is also taken into account by using CC2530 chip and adjusting proper output RF power for coordinator and end devices according to the area which should be covered. Integration of ZigBee and Bluetooth technologies allows users to benefit from both technologies, low power consumption of ZigBee technology and existence of Bluetooth technology in their cellphones. Consequently inhabitants can control their own house by using their own smart phones and there is no need to utilize a remote controller. As a result, costs are reduced and more comfort is provided for inhabitants. This system is tested and its operation is verified in an 80 square meters house successfully.

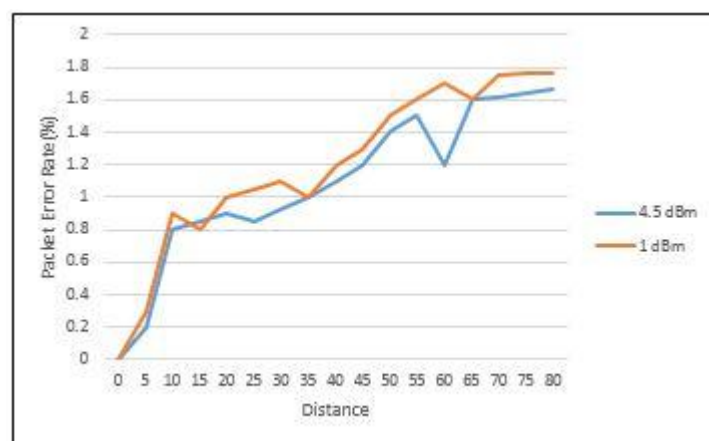


Fig. 14. Packet error rate versus distance.

## REFERENCES

- [1] A. Harrouz, M. Abbes, I. Colak and K. Kayisli, "Smart grid and renewable energy in Algeria," 2017 IEEE 6th International Conference on Renewable Energy Research and Applications (ICRERA), San Diego, CA, 2017, pp. 1166-1171.
- [2] B. K. Barman, S. N. Yadav, S. Kumar and S. Gope, "IOT Based Smart Energy Meter for Efficient Energy Utilization in Smart Grid," 2018 2nd International Conference on Power, Energy and Environment: Towards Smart Technology (ICEPE), Shillong, India, 2018, pp. 1-5.
- [3] H. L. M. do Amaral, J. A. G. Maginador, R. M. J. Ayres, A. N. de Souza and D. S. Gastaldello, "Integration of consumption forecasting in smart meters and smart home management systems," 2018 Simposio Brasileiro de Sistemas Eletricos (SBSE), Niteroi, 2018, pp. 1-6.
- [4] A. Anbarasi and M. Ishwarya, "Design and implementation of smart home using sensor network," 2013 International Conference on Optical Imaging Sensor and Security (ICOSS), Coimbatore, 2013, pp. 1-6.
- [5] J. Byun, B. Jeon, J. Noh, Y. Kim and S. Park, "An intelligent self-adjusting sensor for smart home services based on ZigBee communications," in IEEE Transactions on Consumer Electronics, vol. 58, no. 3, pp. 794-802, August 2012.
- [6] Sathesh, Yasir Babiker Hamdan, "Smart Home Environment Future Challenges and Issues - A Survey" Journal of Electronics and Informatics, vol.3, no.1, 2021.
- [7] Eva-Maria Schomakers, Hannah Biermann, and Martina Ziefle. 2021. Users' Preferences for Smart Home Automation – Investigating Aspects of Privacy and Trust. Telemat. Inf. 64, C, Nov 2021.
- [8] Jo'rayev Vohid Tojimatovich and Xalilova Muhabbat Alimdjanoyna, "CLIMATE CONTROL AND LIGHT CONTROL IN A SMART HOME", Euro. Jour. of Inte. Res. and Dev., vol. 8, pp. 149–155, Oct. 2022.
- [9] Ma, C., Guerra-Santin, O. & Mohammadi, M. Smart home modification design strategies for ageing in place: a systematic review. J Hous and the Built Environ 37, 625–651 (2022).
- [10] Donghang Liu, Chensi Wu, Lulin Yang, Xiaoying Zhao, Qifeng Sun, "The Development of Privacy Protection Standards for Smart Home", Wireless Communications and Mobile Computing, vol. 2022, Article ID 9641143, 10 pages, 2022.
- [11] Olutosin Taiwo, Absalom E. Ezugwu, "Internet of Things-Based Intelligent Smart Home Control System", Security and Communication Networks, vol. 2021, Article ID 9928254, 17 pages, 2021.
- [12] Ching-Han Chen, Ming-Yi Lin and Wen-Hung Lin, "Designing and Implementing a Lightweight WSN MAC Protocol for Smart Home Networking Applications", Journal of Circuits, Systems and Computers, vol.26, no. 3, 2017.
- [13] Rebecca Jamwal, Hannah K. Jarman, Eve Roseingrave, Jacinta Douglas & Dianne Winkler, "Smart home and communication technology for people with disability: a scoping review", Disability and Rehabilitation: Assistive Technology, 17:6, 624-644, 2022.
- [14] R. Panna, R. Thesrumluk, and C. Chantrapornchai, "Development of Energy Saving Smart Home Prototype," International Journal of Smart Home, vol. 7, pp. 47-65, Jan 2013.
- [15] S. J. Danbatta and A. Varol, "Comparison of Zigbee, Z-Wave, Wi-Fi, and Bluetooth Wireless Technologies Used in Home Automation," 2019 7th International Symposium on Digital Forensics and Security (ISDFS), Barcelos, Portugal, 2019, pp. 1-5
- [16] D. M. Han, J. H. Lim, "Smart home energy management system using IEEE 802.15.4 and zigbee," IEEE Transactions on Consumer Electronics, vol. 56, pp. 1403-1410, Aug. 2010.
- [17] S. Marksteiner, V. J. Exposito Jimenez, H. Valiant and H. Zeiner, "An overview of wireless IoT protocol security in the smart home domain," 2017 Internet of Things Business Models, Users, and Networks, Copenhagen, 2017, pp. 1-8.
- [18] P. Li, Y. Yan, P. Yang, X. Li and Q. Lin, "Coexist WiFi for ZigBee Networks With Fine-Grained Frequency Approach," in IEEE Access, vol. 7, pp. 135363-135376, 2019.

- [19] M. Clarke, J. de Folter, V. Verma and H. Gokalp, "**Interoperable End-to-End Remote Patient Monitoring Platform Based on IEEE 11073 PHD and ZigBee Health Care Profile,**" in IEEE Transactions on Biomedical Engineering, vol. 65, no. 5, pp. 1014-1025, May 2018.
- [20] Texas Instruments Inc., "**CC2530 Datasheet,**"SWRS081B, 2011.
- [21] Xin Li, "**Design of ZigBee Network Node Based on CC2530,**" PLC&FA, pp.97-99, Mar.2011.
- [22] C. Boyer and S. Roy, "**Backscatter Communication and RFID: Coding, Energy, and MIMO Analysis,**" IEEE Transactions on communications, Vol. 62, No. 03, pp. 770–785, 2014.
- [23] H. Landaluze, A. Perallos, E. Onieva, A. Laura and L. Bengtsson, "**An Energy and Identification Time Decreasing Procedure for Memoryless RFID Tag Anti-Collision Protocols,**" IEEE Transactions on Wireless Communications, Vol. 15, No. 06, pp. 4234-4247, 2016.
- [24] A. Alma'aitah, H. S. Hassanein and M. Ibnkahla, "**Tag Modulation Silencing: Design and Application in RFID Anti-Collision Protocols,**" IEEE Transactions on Communications, Vol. 62, No. 11, pp. 4068–4079, 2014.
- [25] F. Nafar and H. Shamsi, "**Design and Implementation of an RFID-GSM-Based Vehicle Identification System on Highways,**" in IEEE Sensors Journal, vol. 18, no. 17, pp. 7281-7293, 1 Sept.1, 2018.
- [26] Jian-Ming Liao, Xue-Qin He, Guo-Ming Lu1, Si-Yu Zzhan, "**The research and design of ZigBee wireless networking based on CC2530**" 2013 10th International Computer Conference on Wavelet Active Media Technology and Information Processing (ICCWAMTIP)
- [27] Francesca Cuomo, Anna Abbagnale and Emanuele Cipollone,"**Cross-layer network formation for energy-efficient IEEE 802.15.4/ZigBee Wireless Sensor Networks**",Ad Hoc Networks,Vol 11, No. 2, pp.672-686,Mar.2013.
- [28] Texas Instruments Inc., "**CC2530 User's Guide,**"SWRU191D, 2013.
- [29] IEEE Std. 802.15.4-2006: Wireless Medium Access Control (MAC) and Physical Layer (PHY) specifications for Low Rate Wireless Personal Area Networks (LR-WPANs)
- [30] Adam Gschwender and Ata Elahi, "Zigbee Wireless Sensor and Control Network" Prentice Hall, 2009.
- [31] Boris Mihajlov1, Mitko Bogdanoski,"**overview and analysis of the performances of ZigBee-based wireless sensor networks** in International Journal of Computer Applications 29(12):28-35 · September 2011.
- [32] T. Nimi and P. Samundiswary, "**Comparative Performance evaluation on Priority based ZigBee Network with tree and mesh routing,**" 2018 4th International Conference on Electrical Energy Systems (ICEES), Chennai, 2018, pp. 691-695
- [33] S. G. Varghese, C. P. Kurian, V. I. George, A. John, V. Nayak and A. Upadhyay, "**Comparative study of zigBee topologies for IoT-based lighting automation,**" in IET Wireless Sensor Systems, vol. 9, no. 4, pp. 201-207, 8 2019.
- [34] HC05-Bluetooth to Serial Port Module datasheet.
- [35] Panjaitan, S.D., Hartoyo, A.: '**A lighting control system in buildings based on fuzzy logic**', Telkommika, 2011, 9, (3), p. 423.



# FPGA-Implementation of Electronic Voting Machine (EVM)

Abhishek Kumar 

Electronics and Electrical, Lovely Professional University, Phagwara, Punjab, India.  
Email: abkvjti@gmail.com (Corresponding author)

## ABSTRACT:

The voting process is one of the most significant areas that benefits from technological growth, and the development of digital technology has changed many other industries. Electronic voting machines (EVMs) are an essential part of traditional voting systems because of their effectiveness, accuracy, and ease of use. The design, architecture, and advantages of the FPGA (Field-Programmable Gate Array) implementation of an electronic voting machine over conventional voting systems have been explored in this work. EVMs based on FPGA have benefits in terms of reliability, flexibility, security, and speed. The elements of the FPGA implementation, the design process, and the difficulties in maintaining data integrity and thwarting tampering are also covered in the article. The goal is to demonstrate how FPGA technology can be applied to build a voting system that is safe, reliable, and effective, therefore enhancing the election process. FPGA-based EVM describes more complex functionalities and enhances performance and electronics voting application

**KEYWORDS:** EVM, Voting, FPGA, Counting, Efficient design

## 8. INTRODUCTION

In democratic cultures, the voting process is essential, and it is crucial to guarantee its correctness and integrity. Voting is the foundation of democratic systems, where citizens elect representatives based on majority opinion. Historically, elections have used paper ballots, a process vulnerable to issues like vote tampering, errors in counting, and time inefficiency [1]. Electronic voting machines (EVMs), which offer automated, precise, and quick voting and counting, were created to overcome these problems. To address these challenges, the shift toward electronic voting has gained prominence, and the EVM has emerged as a viable solution. EVMs not only streamline the voting process but also ensure better data integrity and security, which is critical for fair election outcomes [2]. Despite the advantages of EVMs, concerns remain regarding security, particularly the risks associated with removable storage devices like memory cards, which can be tampered with. To address these security concerns, we present a digital EVM system designed using Verilog HDL and implemented on FPGA [3], thereby eliminating physical storage vulnerabilities and introducing digital security measures like password protection and voter verification. Field-Programmable Gate Arrays (FPGAs) have become a viable platform for EVM implementation in recent years. By reconfiguring logic and processing components, FPGAs provide the flexibility of hardware programming, allowing for the creation of adaptable and effective systems. FPGA-based EVMs are the perfect option for safe voting applications as they not only increase the voting process's dependability and security but also provide real-time processing and improved hardware control. A democratic society must prioritize the efficiency, security, and integrity of the election process [4]. Ensuring a dependable and safe voting process has become crucial due to the growing usage of electronic voting systems. FPGA-based systems are more secure than software-based ones, they can still be attacked via reverse engineering or side-channel attacks. The EVM can be protected using countermeasures including secure boot sequences, tamper-resistant designs, and the application of cryptographic algorithms. The voting process's security and integrity are crucial. In this regard, FPGA-based EVM are beneficial as they enable the incorporation of strong security features at the hardware level [5].

(a) Data Encryption: Encryption methods can be implemented directly on the FPGA to guarantee that vote data is safely sent and saved. As a result, attackers will find it more difficult to intercept and alter vote data.

(b) Tamper Detection: FPGA-based systems can contain elements to detect physical tampering, such as voltage,

Paper type: Research paper

<https://doi.org/xxx>

Received: 30 December 2024; Revised: 22 January 2025; Accepted: 23 February 2025; Published: 1 March 2025

How to cite this paper: A. Kumar, "FPGA-Implementation of Electronic Voting Machine (EVM)", *Majlesi Journal of Telecommunication Devices*, Vol. 14, No. 1, pp. 31-38, 2025.

temperature, or logic state sensors, to warn authorities of potential security breaches.

(c) Audit Trails: Election results may be transparently verified by using FPGAs to create audit trails, which guarantee that every vote is documented together with its timestamp and related security hash.

Processing massive volumes of data in real-time, FPGAs may use a lot of electricity. Low-power FPGAs or power-efficient design strategies, including lowering clock frequencies or improving the logic architecture, can reduce this problem. Compared to conventional voting machines, FPGA-based solutions might be more costly and complicated to build. However, the higher initial cost is justified by the long-term advantages, which include reconfigurability, scalability, and improved security. The remainder of the article is organized as follows, literature review is included in section 2. The design and implementation of EVM with FPGA using Verilog HDL is illustrated in section 3. The result and analysis is presented in section 4 and finally concluded in section 5.

## 9. LITERATURE REVIEW

The need of speeding up the vote-counting process and minimize human error pushed the early deployment of EVMs. First-generation electronic voting systems relied on embedded microcontrollers, however security problems soon emerged due to these systems' susceptibility to software flaws. A more reliable and secure solution was provided by the use of FPGA technology into the EVM architecture. The shift from software-based to hardware-based EVM systems has been covered in a number of studies. According to research in [6], FPGA-based EVMs might address several issues with microprocessor-based systems, including high maintenance costs because of the need for regular software upgrades and susceptibility to software hacking. FPGAs provide an alternative by putting into practice extremely configurable, safe, and tamper-resistant hardware-based solutions. FPGAs offer significant advantages for designing voting systems due to their customizable nature and ability to perform parallel processing. Because of their versatility and capacity for parallel processing, FPGAs provide several benefits when it comes to voting system design. FPGAs are configured to perform certain functions, such as vote counting, encryption, and security protocols, directly within the hardware thanks to the flexible design of FPGAs. In recent years, several FPGA implementations for EVMs have been investigated. One remarkable example is the work of [7] suggested an electronic voting system based on FPGA, in which the votes were safely saved in on-chip memory and the FPGA counted the votes in real-time. An encryption module was also included in their design to ensure the votes' privacy. Research in [8] conducted additional research that concentrated on creating an FPGA-based EVM with a built-in real-time voter validation mechanism. This concept had a counting device that offered real-time vote tallying, a secure memory block for storing votes, and a control unit to oversee voting sequences. According to their research, using FPGA gave more flexibility in meeting different election needs, such as supporting several candidates and using different vote-counting techniques.

The capacity of FPGAs to include tamper detection and encryption directly into the hardware is one of their advantages. The application of FPGA in establishing secure communication protocols within EVMs was investigated in research conducted by [9]. To safeguard vote data while it is being sent and stored, they included cryptographic techniques like Advanced Encryption Standard (AES) into the FPGA hardware. Effective real-time encryption and decryption were made possible by the FPGA's built-in parallelism, guaranteeing vote integrity throughout the voting procedure. Research in [10] focused on the FPGA-based EVMs' real-time processing capabilities. The total time needed for vote tallying was significantly reduced by their FPGA implementation's ability to process several votes in parallel. Additionally, their idea showed how FPGA systems may be scaled to manage elections of different sizes, from national elections with a big voter base to local elections with fewer candidates. The concept of electronic voting has evolved significantly over the years. In authors [11] described an early voting system that could automate the recording of votes without manual handling, laying the foundation for secure digital voting systems. Electronic systems developed in [12] presented an electronic device that eliminated human handling of votes, reducing the risk of fraud and error. Further advances in EVM technology were noted in [13], who described programmable devices capable of handling complex election scenarios, including those requiring multiple votes per voter. Authors in [14] introduced the concept of biometric security in EVMs, using fingerprint recognition to further secure voting processes. Each of these studies contributed critical insights into the development of secure, efficient, and adaptable EVMs that meet the diverse needs of various electoral systems.

## 3. DESIGN AND ARCHITECTURE OF FPGA-BASED EVM

The goal of an FPGA-based Electronic Voting Machine's (EVM) architecture and design is to create a reliable, safe, and effective system for collecting, storing, tallying, and sending votes during an election. High-speed parallel processing and reconfigurability are two benefits of FPGA technology [15,16] that make it perfect for applications requiring fault tolerance, security, and real-time data processing. Below, we discuss the design considerations, components, and architecture involved in an FPGA-based EVM. Fig 1 presents the EVM system is developed in three distinct stages, ensuring security and accuracy throughout the voting process. Designed using Verilog HDL, this EVM

can be implemented on an FPGA, allowing for easy reprogramming and cost-effective adaptation across various elections.

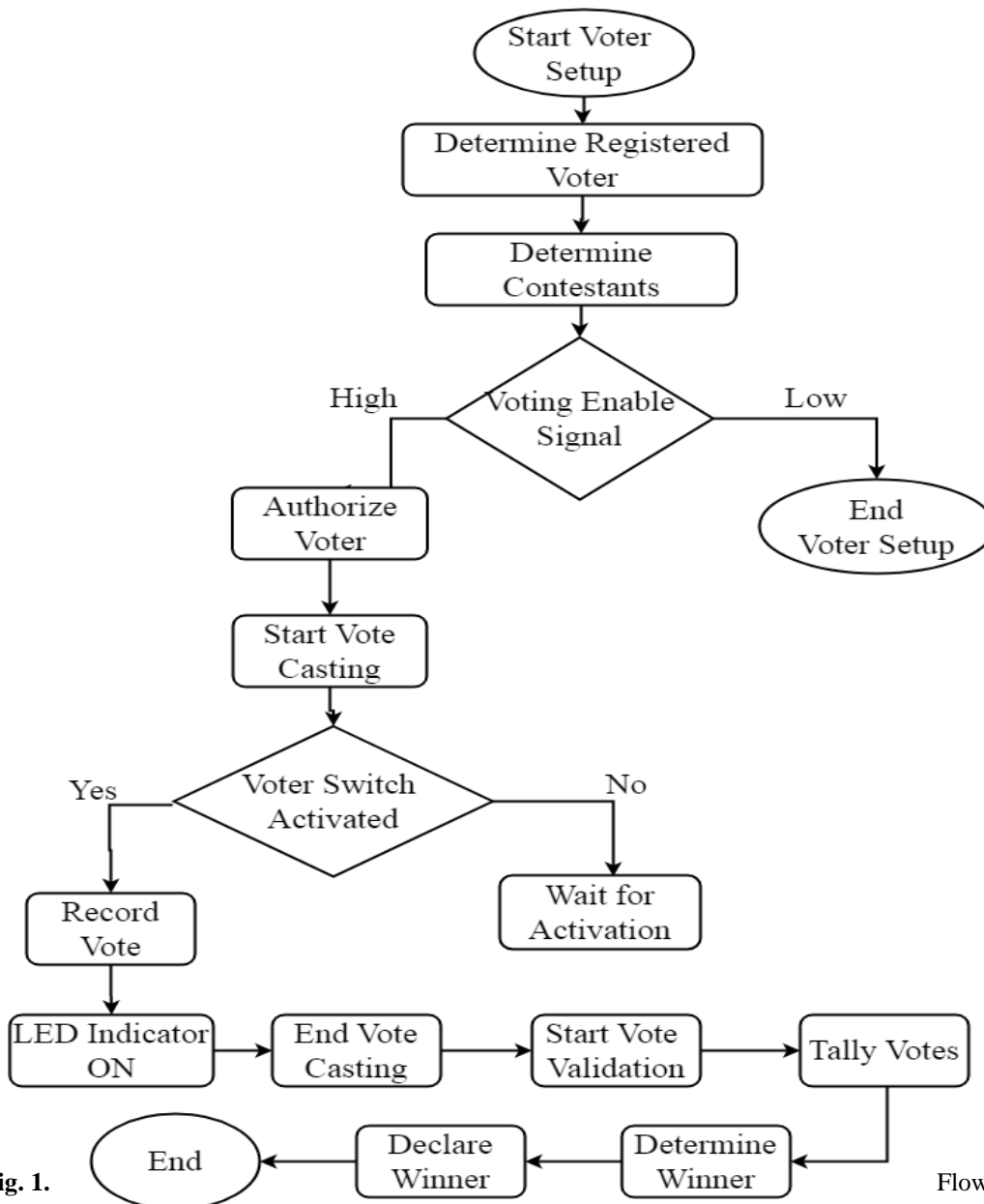


Fig. 1. process.

Flow chart of EVM

Stage 1: Voter Setup At the beginning of the election, the total number of registered voters and contestants is determined. An active high input signal, termed Voting Enable, authorizes each voter to cast a single vote, ensuring the validity of the voting session.

Stage 2: Vote Casting The voting process begins when the Voting Enable signal is high. Voters select their preferred candidate by activating the Voter Switch, which records the vote in the corresponding candidate’s registry. Visual confirmation through an LED indicator assures the voter that their vote has been successfully cast.

Stage 3: Vote Validation and Result Declaration Upon completion of voting, the system verifies the results by tallying votes stored in each candidate’s registry. The candidate with the highest count is declared the winner, and process ends.

Field-Programmable Gate Array (FPGA) can be configured to carry out particular functions. In contrast to

conventional microcontrollers or CPUs, FPGAs provide a high degree of parallelism and circuit design freedom. They are made up of an assortment of input/output blocks, interconnects, and programmable logic blocks (PLBs) that may be set up to carry out a broad range of tasks. FPGAs provide designers the ability to create unique hardware designs for particular uses, such as the creation of an electronic voting machine. The following are the benefits of implementing an electronic voting machine with FPGAs:

- (a) Parallel Processing: FPGAs are excellent for high-speed jobs like encryption and vote counting
- (b) Flexibility: The voting system may be updated and modified without requiring new hardware
- (c) Security: Encryption and tamper detection methods at the hardware level,
- (d) Real-time Operation: FPGAs can process data in real-time

Verilog HDL was chosen due to its hardware abstraction capabilities and compatibility with Xilinx Vivado tools. The design operates on a Artix 7 FPGA, which offers high configurability and cost efficiency, making it suitable for various election types. An FPGA-based EVM integrates multiple functionalities into a single hardware platform, from voter input to vote storage, counting, and result declaration. A polling officer controls the Voting Enable signal, which is only enabled during legitimate voting times, the system clock makes sure that the whole voting process is synchronized. The voter can choose from the three candidates after the Voter Switch is turned on. An LED indicator illuminates when a vote is cast, removing any doubt among voters and verifying that the vote was successfully registered. To visually track the number of votes cast for each candidate, the EVM uses three seven-segment displays, each of which is coupled to an active low signal (An0, An1, An2). This instant response simplifies the verification process and increases vote-counting transparency. The objective of the work is

- (a) Verilog Hardware Description Language (HDL) to design and implement EVM.
- (b) The EVM module mimics the voting mechanism, records votes for various parties, and shows the vote tallies.
- (c) The system also allows voters to select "None of the Above" (NOTA).
- (d) Additionally, LED indicators are incorporated into the design to verify legitimate votes and highlight incorrect inputs if an improper switch combination is discovered.

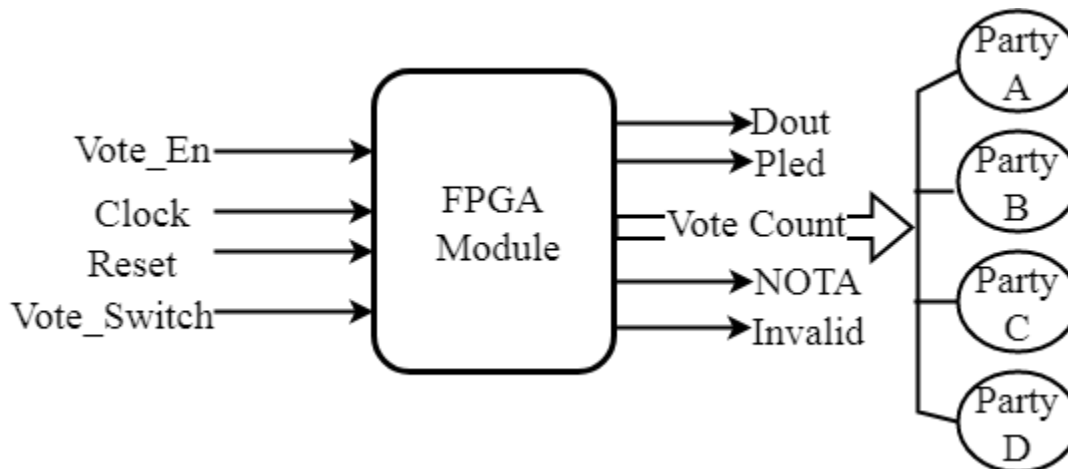


Fig. 2. Block diagram of EVM module.

The EVM module that you are designing includes a variety of features such as vote counting, LED control for visual feedback, and flag handling for invalid voting attempts. To manage the voting process, the EVM system is built with several input and output signals. Vo\_en, which permits voting while it is active; first, a reset signal to set the system to a known state; clk, a clock signal for synchronization; and vo\_switch, a 5-bit input that chooses which candidate or option the vote is cast for, are among the input signals. Pled, a 5-bit signal that controls the LEDs for each party and NOTA, and Dout, the overall aggregate of votes cast for all candidates and the NOTA option, make up the output signals. Furthermore, 8-bit registers hold the vote totals for the four candidates (Parties 1 through 4) as well as the NOTA option, and the invalid flag indicates if a vote was cast that is invalid. The design contains parameters, registers, and counters, such as LED\_TIMER\_MAX, which determines the length for which the LED should remain after a vote is cast. Pled manages the LED indicators for each candidate and NOTA, while the Party1, Party2, Party3, Party4, and Nota registers keep track of the number of votes cast. After a vote, a counter called led\_timer controls how long the LEDs remain light. The voting mechanism checks the vo\_switch value to see which candidate the vote is cast for when vo\_en is active. The appropriate LED in Pled is activated for the amount of time indicated by LED\_TIMER\_MAX, and the related vote count is increased if the vote is legitimate. The invalid flag is raised if the vote is deemed invalid. After every vote, the

led\_timer decreases, and when the timer hits zero, the LED is turned off. Lastly, the sum of the votes cast for each candidate plus the NOTA choice is used to get the final vote total, Dout. Additionally, the `invalid` flag is raised (set to high) if an invalid value is detected on the `vo\_switch` input, indicating that the vote does not correspond to a valid candidate or the NOTA option.

#### 4. RESULT ANALYSIS AND VALIDATION

The simulation results in fig 3 confirmed that the proposed Electronic Voting Machine (EVM) design meets the functional requirements of a secure and reliable voting system. The RTL schematic in Fig 4 validated each stage of the voting process, demonstrating accurate vote registration, signal synchronization, and output verification. The final vote count displayed in the Dout register matched the total number of participants, ensuring there were no instances of overvoting or data discrepancies. The simulations showed that every vote was correctly registered and allocated to the chosen candidate's registry, with signal timings synced to guarantee that votes were cast just once and kept safe. To ensure there were no overvotes or discrepancies and that the final result accurately represented the total number of voters, it was cross-checked before being shown in the Dout register. By removing the possibility of duplicate or incorrect votes, this precise count in Dout demonstrates how effectively the system manages votes in a clear and reliable method. This successful validation procedure shows that the suggested EVM architecture is suitable for practical applications and further validates its resilience. The design may be used in a variety of election contexts, from small-scale municipal elections to major public elections, guaranteeing its usefulness in a range of situations. The results of the simulation demonstrate that the EVM system, which was developed with Verilog HDL, operates efficiently and reliably. To ensure accuracy, security, and adherence to design criteria, every system component underwent extensive testing in the Xilinx Vivado simulation environment.

The following are a few significant findings from the simulation results:

1. **Vote Count Update and LED Feedback:** The voting process increases the number of votes in the appropriate register (Party0, Party1, or Party2) when the system detects the selected candidate. The voter is given visible proof that their vote was correctly recorded simultaneously and LED is turned on. This feature guarantees the system's responsiveness to legitimate inputs while simultaneously boosting voter trust.

2. **Handling of Invalid Inputs:** The EVM is made to handle illegal or incorrect inputs efficiently. The system generates an invalid signal whenever it detects an incorrect signal, such as a repeated vote or an input that is outside of the permitted voting parameters. This guarantees that there are no increases in the vote count registers, thus only valid votes are counted. By eliminating vote tampering and reducing mistakes brought on by illegal inputs, this feature improves the EVM's security and accuracy.

3. **Total Vote Display Accuracy:** The total number of votes cast for each candidate is adequately shown in the EVM's Dot output. The system's capacity to consistently track and validate the total number of votes is demonstrated by the fact that the sum of the individual vote counts kept in each candidate's register (Party0, Party1, Party2) coincides exactly with the value displayed on the Dot. To maintain openness and validate the election results after the voting process, the total vote count must be calculated accurately.

4. **Timing and Synchronization:** The results additionally emphasize the system's exact timing and signal synchronization, especially when the voting enable signals and system clock are used. Because every vote is timed to the clock cycles, there is a lower probability of data corruption or miscounts and voter registration is reliable and orderly. This synchronization ensures precise and efficient system operation.

5. **Candidate Result Declaration:** After voting is over, the EVM system counts the votes and correctly declares the winner to be the candidate with the most votes. In accordance with the system's architecture, which relies on vote totals to correctly report outcomes, this step completes the voting process. Thus, each module's ability to produce safe, dependable, and accurate voting results is validated by the system simulation.

The Artix7 FPGA-based power consumption report presented in Fig 5 shows the total on chip power consumption is 0931 W, out of which 88% is dynamic power indicated the EVM is active and has maximum time. The power consumption during ideal phase is only 12%. Fig 6 presents the resousre utilization summary for the EVM requires LUT, slice registers, and IOBs. There is a significant difference between traditional EVM and FPGA-based EVM. Presented design describes more complex functionalities and enhances performance and electronics voting application.



Name	Slice LUTs (134600)	Slice Registers (269200)	Bonded IOB (285)	BUFGCTRL (32)
N EVM	68	47	44	1

Fig. 5. EVM power profile report.

## Summary

Power estimation from Synthesized netlist. Activity derived from constraints files, simulation files or vectorless analysis. Note: these early estimates can change after implementation.

<b>Total On-Chip Power:</b>	<b>0.931 W</b>
<b>Design Power Budget:</b>	<b>Not Specified</b>
<b>Power Budget Margin:</b>	<b>N/A</b>
<b>Junction Temperature:</b>	<b>28.1°C</b>
<b>Thermal Margin:</b>	<b>71.9°C (21.3 W)</b>
<b>Effective <math>\theta_{JA}</math>:</b>	<b>3.3°C/W</b>

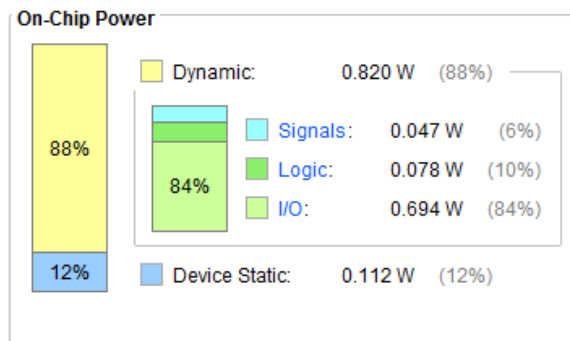


Fig. 6. Resource utilization summary of FPGA implementation of EVM.

## 5. CONCLUSION

This Verilog HDL-based EVM design meets the critical requirements for secure and efficient voting, providing an adaptable solution for various election types. Future enhancements include integrating biometric authentication to strengthen voter verification and prevent unauthorized access. Additionally, the design could incorporate real-time data transmission for remote election monitoring and statistical analysis, paving the way for fully digitized and auditable electoral processes. Implementation of EVM with FPGA technology offers benefits like increased speed, flexibility, security, and scalability. Customizable and effective voting machines that can manage complex tasks like vote counting and encryption in real time are made possible by FPGAs. Any election system must have strong security and tamper-resistance measures and FPGA-based solutions provide reliable ways to guarantee the voting process's integrity. The advantages of FPGA-based EVMs make them a viable alternative for the future of electoral systems, helping to create more secure, transparent, and effective elections in spite of the difficulties associated with power consumption and development complexity.

## REFERENCES

- [30] Ohize, Henry O., et al. "Blockchain for securing electronic voting systems: a survey of architectures, trends, solutions, and challenges." *Cluster Computing* 28(2), pp 132. 2025
- [31] Oyelude, Olufunmilayo, and Ibukunoluwa Olojede. "Evaluating the effectiveness of electronic voting systems in Nigeria: Challenges and opportunities." *African Journal of Politics and Administrative Studies* 16(2), pp 84-104, 2023
- [32] Swapna, Tangelapalli, Dharmavaram Asha Devi, and Manu Gupta. "Digital Electronic Voting Machine Using Verilog." *Disruptive technologies in Computing and Communication Systems*. CRC Press, pp 425-431, 2024.
- [33] Keerthi, T., et al. "Real Time Implementation of Biometric-based EVM System for Distinct Verification." *Procedia Computer Science* 230, pp 407-416.2023.
- [34] Molina, Romina Soledad, et al. "High-level synthesis hardware design for fpga-based accelerators: Models, methodologies, and frameworks." *IEEE Access* 10, pp 90429-90455, 2022
- [35] Kalra, Hariom, et al. "Impregnable Electronic Voting Machine Harnessing the Power of FPGA Zynq 7000." *IEEE International Conference on Interdisciplinary Approaches in Technology and Management for Social Innovation (IATMSI)*. Vol. 2., 2024.
- [36] Soomro, Zeeshan Ahmed, et al. "FPGA Based Real-Time Face Authorization System for Electronic Voting System." *3rd International Conference on Computing, Mathematics and Engineering Technologies (iCoMET)*, pp 1-6 2020.
- [37] Khan, Areeb Adnan, et al. "DigitalNizam: Shaping the Future of Pakistani Elections through Secure Field-Programmable Gate Array-Based Voting Solutions." *Engineering Proceedings* 46(1) pp 44, 2023.
- [38] Zhang, Jiliang, and Gang Qu. "Recent attacks and defenses on FPGA-based systems." *ACM Transactions on Reconfigurable Technology and Systems (TRETS)* 12(3), pp 1-24, 2019.
- [39] Drimer, Saar. "Volatile FPGA design security—a survey." *IEEE Computer Society Annual Volume*, pp 292-297, 2008.
- [40] Coşgun, Ercan, and Anıl Çelebi. "FPGA based real-time epileptic seizure prediction system." *Biocybernetics and*

- Biomedical Engineering* 41(1), pp 278-292, 2021
- [41] Drimer, Saar. "**Volatile FPGA design security—a survey.**" *IEEE Computer Society Annual Volume*, pp 292-297, 2008
- [42] Kumar, Mritunjay, et al. "**FPGA Based Voting Machine.**" *Kilby*, 7<sup>th</sup> edition ,pp 100, 2023.
- [43] Chaabane, Faten, et al. "Low power blockchained e-vote platform for university environment." *Future Internet* 14(9) pp 269, 2022.
- [44] Tripathi, Suman Lata, Abhishek Kumar, and Mufti Mahmud. "**FPGA for secured hardware & IP ownership.**" *IEEE international conference of electron devices society Kolkata chapter (EDKCON)*. IEEE, 2022.
- [45] Kumar, Abhishek. "**VLSI implementation of Vedic multiplier.**" *Design and Development of Efficient Energy Systems*, pp 13-30, 2022

# Analysis and Simulation of Reliable and Robust UAV Data Transmission Through Geo Satellite using Long Code DSSS with ZP Algorithm

Ehsan Azizi<sup>1</sup>, Mohammad Hossein Madani<sup>2</sup> 

1- Electrical Engineering Faculty, Malek-Ashtar University of Technology, Lavizan, Tehran, Iran.

2- Electrical Engineering Faculty, Malek-Ashtar University of Technology, Lavizan, Tehran, Iran.

Email: madani@mut.ac.ir (Corresponding author)

## ABSTRACT:

Wireless communication is the major form of connection nowadays. In most cases it exploits the benefits of the spread spectrum techniques to overcome corruptions introduced by channel like Doppler residual frequency, noise, interference and jamming. The purpose of this paper is to exchange secure information with unmanned aerial vehicle (UAV) through GEO satellites at low bit rates (kbps) with the aim of expanding the radius and operational coverage in the absence of LoS communications. In order to evaluate the possibility of communication, the link budget calculations are performed and minimum Carrier to Noise ratio (C/N) required to receive the signal at the receiver's side is measured. Basically, due to the information relay with geo-satellite, security of the link and the lack of access to information by unauthorized users is very important, therefore, direct sequence spread spectrum technique with long code has been used in physical layer to increase signal security and non-detectability. In order to detect the signal, different code acquisition techniques are examined and Zero Padding (ZP) is shown to outperform the other existing techniques in terms of Doppler effect tolerance and probability of detection in low SNRs. The results show that the proposed method makes detection at SNR levels as low as -14dB possible with a probability of false alarm of  $10^{-5}$  and  $P_d > 0.9$ .

**KEYWORDS:** SNR, Acquisition, UAV, Doppler, Zero Padding (ZP).

## INTRODUCTION

Deployment of different means of wireless communication has become more widespread among different groups with different applications. From cell phones and wireless Internet to secure military communications. The propagation of radio waves in free spaces such as the urban environment, causes the waves to be reflected and reach the receiver from different paths. Additionally at each certain place and time, numerous users may request to make use of a specific frequency channel under a desired protocol. One way to deal with such problems is the use the spread spectrum technique. The basis of this technique is to spread the signal spectrum in the frequency domain beyond the actual need for the data contained in it. Satellite communications are the outcome of research in the area of communications and space technologies whose objective is to achieve ever-increasing ranges and capacities with the lowest possible costs. In this paper, the UAV is assumed to deploy the Spread Spectrum technique in order to increase the transmission of information over long distances, considering its extended range coverage, while using a public broadcasting satellite to relay links to UAV. Spread spectrum techniques are among the most commonly used techniques in communication systems today, since the use of these techniques will increase the security of the signal layer.

Today, a lot of research has been done to robustly send data via UAVs and mobile receivers and many papers have been published in this field. [1] explores the paradigm that Remotely Piloted Air Systems (RPASs) or Unmanned Aerial Vehicles (UAVs) are integrated as a communication platform with cellular networks using radio access. [2] explores tethered UAV assisted hybrid cooperative communication to improve the end-to-end performance of the links between

Paper type: Research paper

<https://doi.org/xxx>

Received: 17 February 2024; Revised: 11 April 2024; Accepted: 20 June 2024; Published: 1 March 2025

How to cite this paper: E. Azizi, M. H. Madani, "Analysis and Simulation of Reliable and Robust UAV Data Transmission Through Geo Satellite using Long Code DSSS with ZP Algorithm", *Majlesi Journal of Telecommunication Devices*, Vol. 14, No. 1, pp. 39-48, 2025.

base stations and user equipment. [3] examines potential data link candidates for unmanned aerial vehicles (UAVs). Authors in [4] put forward the UAV data link deployment scheme based on 5G technology after analyzing the shortcomings of traditional UAV data links, and analyse the key issues such as transmission rate, end-to-end delay and network coverage. [5] proposes an anti-interference scheme, named as Mary-MCM, for UAV data links in AGIVNs based on multi-array (M-array) spread spectrum and multi-carrier modulation (MCM). [6] characteristics of code division multiple access are used to realize the TT&C of the mass unmanned aerial vehicle. [10] the design and analysis of Telemetry, Tracking and Command Subsystem (TT&CS) for Libyan imaging mini-satellite (LibyaSat-1) is presented. The presented method in [7], called Segmented Zero Padding (SZP), reduces the Doppler effects on the probability of detection in the acquisition of GPS receiver. To improve the mean acquisition time performance of the zero-padding (ZP) method, [8] is proposed to fully exploit the computation capability of FFT by partially folding the local pseudo-noise (PN) code. In [9], an expression for the expected values of the cells' energies to analyze the impact of the Doppler bin width on detection and false alarm probabilities is presented. [10] presents a new onboard PN Codes Synchronizer Architecture based on the Generalized Zero Padding Algorithm (GZP) and frequency domain Doppler compensation. In [11], a fast acquisition algorithm is put forward for high dynamic DSSS signal based on double layers of short FFT. In [12], the widely used Zero Padding Scheme (ZPS) for direct GPS P-code acquisition is generalized to investigate the effects of the ZPS on detection performance, parallel searching capability, and mean acquisition time. [13] compares the meaning of different threshold setting principles in the code acquisition process of a direct sequence (DS) spread spectrum (SS) receiver. Finally, [14] indicates the standards of DVB-S and DVB-S2. What is analyzed in this paper is sending reliable and robust data through the geo satellite using the Zero Padding method to UAV, which has been done with the help of the introduced references. The structure of this paper includes problem definition in section 2, system model in section 3, and performance evaluation of the zero padding method in the section 4, and finally, section 5 contains the conclusion.



Fig. 2. Figure of network.

Table 1. Link Specifications.

Name	Value
Ku band Frequency	11-14 GHz
$f_{\text{uplink}}$	13.75 GHz
$f_{\text{downlink}}$	10.7 GHz
Satellite EIRP	54.4 dB
Height of satellite	35814 Km
G/T Receiver	7 dB/k

## PROBLEM DEFINITION

As previously mentioned in the introduction, spread spectrum techniques are used both to prevent the multipath fading phenomenon and also to increase the range of data transmission to the receiving stations while performing link budget calculations. This method requires significantly larger bandwidth than the original signal bandwidth because the signal processing gain is 30dB. Parameters related to DVB-S and SDVB-S2 standards have been performed for transplanted budget calculations [14].

### 1.1. Calculation of the Minimum C/N

According to the DVB-S and DVB-S2 standard for link budget calculations, the BER value is less than  $10^{-6}$  for BPSK and QPSK modulation schemes [14], and the minimum C/N ratio for signal detection needs to be calculated [19]. The minimum  $E_b/N_0$  value required for  $BER=10^{-6}$  is equal to 10.5dB. Since the received signal is BPSK modulated, the occupied bandwidth of the signal using the RRC filter is 12KHz. In MPSK modulation scheme, to achieve a bit rate of

9.6 Kbps, a minimum of 19.2 KHz channel bandwidth is required [8]. This requirement can be further decreased. C/N ratio required to obtain the desired BER is obtained as follows:

$$50.32 = \left(\frac{C}{N}\right) + 10\text{Log}(2 \times 9600) \quad (3)$$

$$\left(\frac{C}{N}\right) = 7.5\text{dB} \quad (4)$$

### 1.2. Downlink Budget

In the current paper, the receiver, being a ship, car, UAV and etc. has been assumed to be mobile, which might possibly lead to Doppler effect. The downlink budget can be calculated to be  $\frac{C}{N} = 34.3\text{dB}$  based on (3) [16].

The C/N obtained is greater than the calculated minimum C/N, so the downlink is established and the signal is detected in receiver.

### 1.3. Uplink Budget

The calculations in this section are similar to the calculations of the Downlink budget. BER for the uplink is considered to be  $10^{-7}$  [14]. Firstly, as in the previous section, the minimum C/N required for the Uplink is calculated, which will be followed by the calculations for the uplink budget. The value of  $E_b/N_0$  for  $\text{BER}=10^{-7}$  is equal to 11.5dB. The carrier to noise ratio can be calculated as:

$$\left(\frac{C}{N}\right) = 8.6 \quad (5)$$

minimum C/N value can therefore be obtained as follows [19][20]:

$$\frac{C}{N} = 42.78 \quad (6)$$

According to the obtained C/N, it can be concluded that the uplink has been established because it surpasses the minimum C/N.

### 1.4. Signal Model

The k-th sample of In-phase and Quadrature phase components of the received digital baseband signal are as follows:

$$s_I[k] = Ad[k + \tau]c[k + \tau] \cos(\omega_D k \Delta t + \varphi) + n_I[k] \quad (7)$$

$$s_Q[k] = Ad[k + \tau]c[k + \tau] \sin(\omega_D k \Delta t + \varphi) + n_Q[k] \quad (8)$$

Where  $A$  is the signal amplitude,  $d$  is the modulated data bit  $\in \{-1, +1\}$ ,  $\tau$  is the code phase offset of the received signal,  $c$  is the spreading code's chip  $\in \{-1, +1\}$ ,  $\omega_D$  is the residual frequency in radians,  $\Delta t$  is the sampling period (the same as code period i.e. one sample per chip),  $\varphi$  is the unknown carrier phase offset and  $n_I$  and  $n_Q$  are in-phase and quadrature phase additive white Gaussian noises respectively with zero mean and variance  $\sigma^2$ ,  $\mathcal{N}(0, \sigma^2)$ .

Codes used in spread spectrum system; It can be said that these codes cause the signal to become LPI. In other words, it makes access to information impossible for unauthorized individuals and receivers. This is achieved because, to gain access to the desired information, the exact same code used in the transmitter side must be used in the receiver side after full synchronization [15]. The basis of the spread spectrum technique is to expand the bandwidth of the transmitted signal. Considering the codes used in spread spectrum systems, which have a pseudo-noise property, it causes the signal to act similar to noise [15]. In this paper, 14th and 24th order code is used. In fact, security in physical layer proves the signal to be LPI and LPD, which is an intrinsic feature of all SS systems. To retrieve the signal in the receiver, it is necessary for the code to be completely synchronous with the received signal, since if the received signal is not synchronous with the code generator in the receiver due to transmission delay, detection would not be possible. So synchronization in the receiver will include two stages: acquisition and tracking. According to the codes used, there are many synchronization methods. For short codes there are series and parallel methods in the time domain that these methods cannot be used for codes with long periodicity, and so the acquisition methods in the frequency domain have been used, which are the ZP, DF, XFAST method and Average method. In this paper, long codes have been used, so

while reviewing the mentioned methods, select the ZP method and analyze and simulate the detection curves, acquisition time, system model of this method simulated by MATLAB Simulink. In Zero Padding method, it is assumed that the length of the FFT receiver  $L$  and the number of zeros added to the signal are represented by  $N$  [16],[17] so the steps of the Spread Spectrum method following:

- 1) The received signal is sampled at a rate equal to the chip rate and transmitted to the base band.
- 2) A piece with length  $L-N$  of the selected received signal,  $N$  zero is attached to it until its length reaches  $L$ , then its FFT conjugate is calculated.
- 3) A window with length  $L$  is viewed from the production code and its FFT is calculated.
- 4) IFFT The product of FFT is calculated two steps before and  $N + 1$  of the first sample is considered as the result of correlation.
- 5) The maximum IFFT size result of the previous step is compared with the threshold, if it crosses the threshold, the acquisition is declared.[18]

In section3 system model is mentioned, which includes the transmitter, receiver, and finally, we will provide a review of the parameters related to the performance of the simulated method.

### System Model

As a DS receiver starts to operate, the number of samples is removed from the received signal and the acquisition operation, Doppler search is performed on it, then in the tracking stage, go back to the received signal and samples its update is received and synchronized by the distributor code and deleted. At the beginning of the tracking stage, the time taken to acquire the code is considered and the code generator is moved forward as much as this time so as not to lag behind the received signal. Because during the acquisition phase, more recent samples of the received signal are not used and the offset amount obtained at the end of this phase is equal to the shift between the transmitted code and samples of the received signal, which was removed at the beginning of the receiver. The receiver in the current work, focuses solely on the acquisition of the signal.

#### 1.5. Transmitter

Each bit of the transmitted signal, which has a rate of 9.6kbps is multiplied by 1024 chips, which is a sample of quasi-random code with rate 10MHz. Other specifications of the PRN code are given in Table1. The signal is then passed through the RRC filter in the transmitter and each symbol with 8 samples is ready to be sent to the AWGN channel. Fig. 2 shows the transmitted signal spectrum and Fig. 3 shows the channel model.

**Table 2.** Specifications of the PRN code [15]

Name	Value
Primitive Polynomial	$g(x) = x^{14} + x^{10} + x^6 + x + 1$
Binary Mode	[100010001000011]
Octal Mode	42103
Initial LFSR	[00000000000001]
Periodicity	$N = 2^{14} - 1 = 16383$
Processing gain ( $G_p$ )	30dB

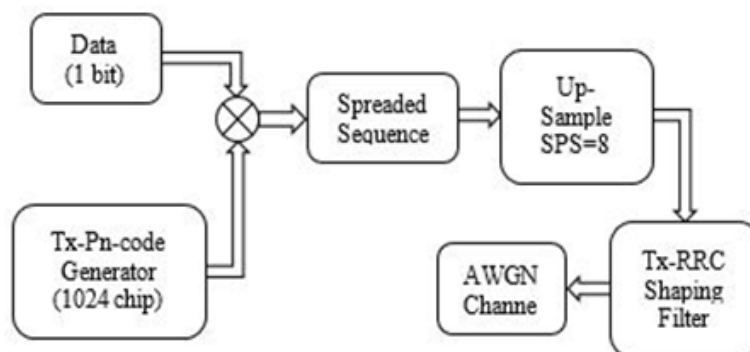


**Fig. 3.** Transmitter Block Diagram.

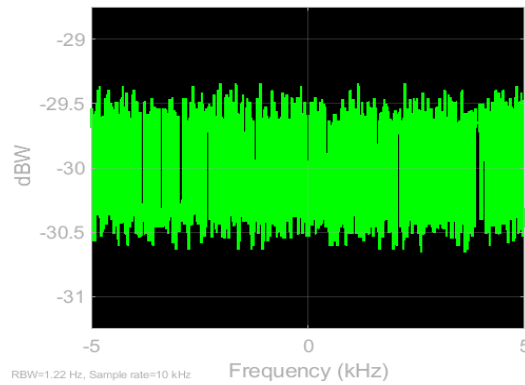


Fig. 4. spectrum of spread signal.

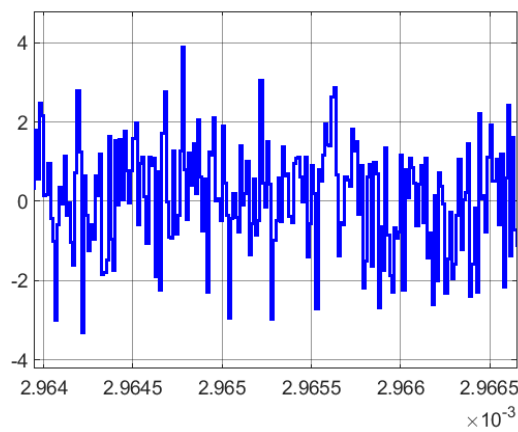


Fig. 5. AWGN channel output with SNR=-5dB.

### 1.6. Receiver

According to the block diagram of the receiver shown in Fig. 5, structure of the receiver is as follows: RRC filter is placed at the beginning of the receiver to remove the transmitter shaping. The signal then enters the down sampling block to remove 8 samples per symbol. The method used to acquire the code in the receiver is ZP. In this method, the receiver picks up half of the FFT block, i.e., 512 samples, by the buffer from the received signal, and also picks up observation windows with a length of 1024 from the code generator in the receiver. The receiver pads 512 zeros to the 512 samples taken from the signal to reach a length of 1024, then takes FFT\* and multiplies by 1024 samples of the output code from which the FFT is taken. This is followed by the IFFT of the signal in the previous stage (product of the received signal multiplied by the PRN code in the receiver’s side). Subsequently, the maximum amount of IFFT is compared with the threshold. If the maximum value is higher than the threshold, the signal enters the tracking phase, otherwise the code generator is shifted by 1024 samples. This comparison is repeated until the maximum amount of IFFT surpasses the threshold.

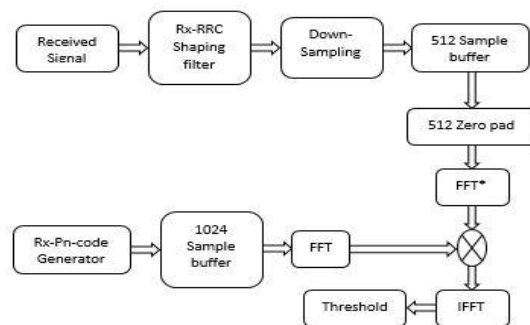


Fig. 6. Receiver Block Diagram.

### 3.2.1 Threshold

The operation of the Tang detector method shown in Fig.4 is such that it takes an RMS value from the IFFT output, and multiplies the output by a value which depends on the SNR value in order for the threshold to surpass the signal level. The value of scale is obtained according to the noise level in this simulation. This scale is obtained in such a way that at SNR = -14dB, the  $P_d=0.9$  [13].

Fig. 4 shows the threshold values and the maximum IFFT value. In each period of code ( $T_C$ ), the maximum signal value is twice as much as the threshold value, which is exactly when the receiver code generator overlaps with the received signal. If in two consecutive correlations, the maximum signal value exceeds the threshold, it means that the Zero Padding method has worked correctly.

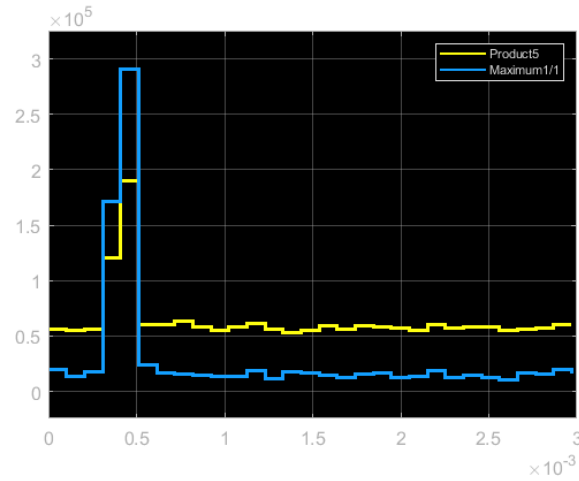


Fig. 7. Compare the maximum correlation result with the threshold.

## Performance Evaluation

Two main criteria of evaluating the performance of an acquisition algorithm are the detection probability of true code phase offset ( $\tau$ ) and mean acquisition time ( $T_D$ ). Here in this paper, these items for the proposed algorithm are analyzed with an eye on comparing the results with similar methods in the literature. Detection performance of the long code acquisition method will be investigated. The probability of detection of phase difference (offset) of the code phase is influenced by various parameters, here SNR is considered as the primary parameter and the effect of various factors such as FFT length and Doppler frequency is expressed with different diagrams of detection probability in terms of SNR.

### 1.7. Detection Performance

Finding the true code phase offset involves correlation of the received signal with a code phase offset of  $\tau$  and locally generated spreading code with offset of  $\delta$ . The probability of detection can be obtained either for the entire observation block or for a cell of the observation window.

Detection probability of a single cell is estimated through Neyman-Pearson method, for a given false alarm probability,  $P_{fa}$ , the threshold can be derived from

$$P_{fa} = \int_{V_t}^{+\infty} f_{\Psi}(x|\theta, H_0) dx \quad (7)$$

With

$$V_t = \sigma_{H_0} \sqrt{-2 \ln P_{fa}} \quad (8)$$

And the detection probability will be [21]:

$$P_d = Q_1 \left( \frac{\mu_1}{\sigma_{H_1}}, \frac{V_t}{\sigma_{H_1}} \right) \quad (9)$$

Where  $Q_1$  is Marcum's Q function and

$$\mu_1^2 = A^2(1 - |P|)^2 \text{sinc}^2(f_D \Delta t (L - N)) n^2 \quad (10)$$

For the ZP method, the detection probability for the entire observation block is obtained from the following equation:

$$V_t = \sqrt{-2 \ln P_{fa} (A^2(1 - |p|)^2 + \sigma^2)(L - N)} \quad (11)$$

$$\mu_1^2 = (L - N)^2 A^2 \text{sinc}^2\left(\frac{\omega_D}{2} (L - N) \Delta t\right) (1 - |p|)^2 \quad (12)$$

$$\sigma_{H_1}^2 = (\sigma^2 + A^2 p^2)(L - N) \quad (13)$$

as is illustrated in [21], GZP method has the best detection performance and XFAST method has the worst performance in signal detection in terms of FFT length. Additionally, GZP method has the highest Doppler tolerance among the other methods. As a result, The ZP method has been chosen to transmit signal. However, the method suffers from the drawback of a longer acquisition time when compared with other methods since it detects the signal at a very low SNR.

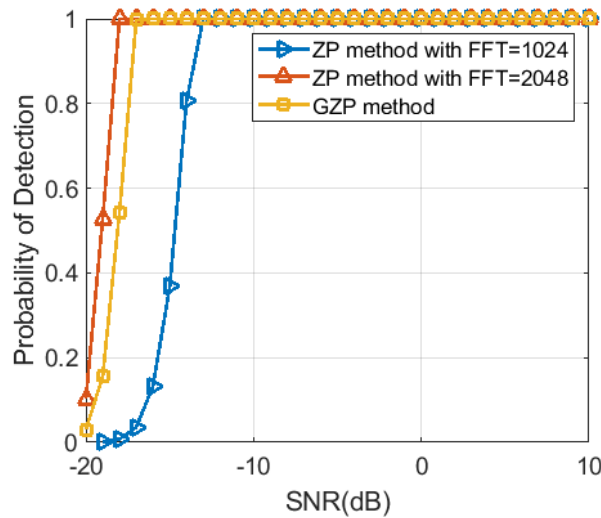


Fig. 8. Probability of detection with FFT=1024 &  $f_d=0$ .

The effect of FFT length on probability of detection is shown in Fig.5. In long code acquisition methods, doubling the FFT length improves the detection performance of the ZP method for nearly 3-4dB.

### 1.8. Mean Acquisition Time

Expected value of the time spent for code acquisition (achieving to desired detection probability) or mean acquisition time for a given false alarm, is a useful measurement for performance comparison of acquisition techniques. The principals of calculating mean acquisition time of an acquisition algorithm are described in [21] for serial search of short codes, which is applicable to long codes as well and is formulated as:

$$E(T_{AcQ}) = \frac{T_D}{P_d^b} \left\{ 1 + (1 + \gamma P_{fa}^b) (2 - P_d^b) \frac{(\Lambda - 1)}{2} \right\} \quad (14)$$

Where  $P_d^b$  and  $P_{fa}^b$  are detection and false alarm probability for the block of observation window, respectively.  $T_D$  is the dwell time for searching an observation window.  $\Lambda$  is the number of observation windows in an uncertainty region of  $\theta$  code phases which is proportional to parallel searching capability of the algorithm that for ZP equals to  $\left\lceil \frac{\theta}{N+1} \right\rceil$ . Consequently, the mean acquisition time of ZP is obtained from (12) with following parameters:

$$\Lambda = \left\lceil \frac{\theta}{N+1} \right\rceil \quad (15)$$

$$P_{fa}^b = 1 - (1 - P_{fa})^N \quad (16)$$

$$P_d^b = 1 - (1 - P_{fa})^{N-1} (1 - P_d) \quad (17)$$

Fig. 8 shows the mean acquisition time in  $T_D$ . Although GZP has the best performance in terms of detection capabilities, it performs poorly in terms of Mean acquisition time.

As mentioned earlier, the ZP method is a vastly time-consuming technique in the acquisition stage, as is shown in Fig. 6, which verifies the results obtained in [8]. Although the chosen method consumes a lot of acquisition time, what remains of high essence is the signal detection at low SNRs, which increases the acquisition time.

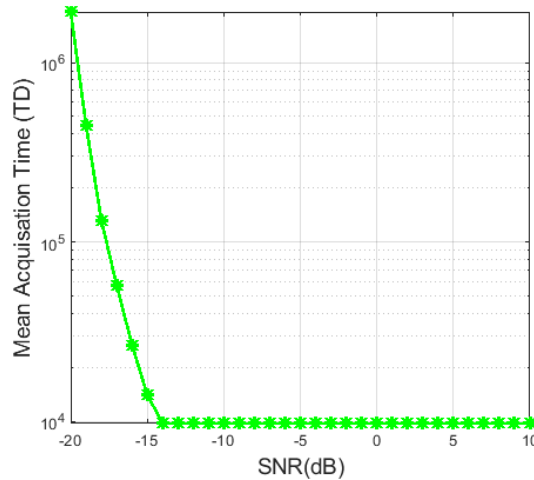


Fig. 9. ZP Mean Acquisition Time.

### 1.9. Doppler Effect

The residual frequency due to Doppler effect depends on the carrier frequency and the relative speed between the transmitter and the receiver. The residual frequency (usually Doppler) appears in the first argument of the Marcum Q-function as:

$$\text{sinc}^2\left(\frac{\omega_D}{2} n \Delta t\right) \quad (18)$$

According to which, the first zero occurs in  $\frac{1}{T_{Cl}}$  [21]. therefore, in the ZP method, assuming a chip rate of 10MHz and an FFT length of 1024 samples, the first zero-crossing occurs at approximately 19KHz. Therefore, the Doppler frequency has very little effect on the detection performance of the ZP method.

In the ZP method with the mentioned conditions, Doppler tolerance is equal to [7], [8]:

$$f_d = \frac{f_s}{L - N} = \frac{10^7}{1024 - 512} = 19 \text{KHz} \quad (19)$$

In this work, the receiver is considered to be a UAV flying at the speed of 350 km/h, followed by a subsequent Doppler shift which can be calculated as [19]:

$$f_{\text{doppler}} = \frac{V_{UAV}}{\lambda} = 3.5 \text{KHz} \quad (20)$$

Therefore, comparison of (17) and (18) shows that doppler effect can be ignored.

As shown in Fig.7, the Doppler effect has a negligible effect on the detection of the ZP method. As the Doppler frequency rises to 20 kHz, the detection probability drops by 2 to 3dB

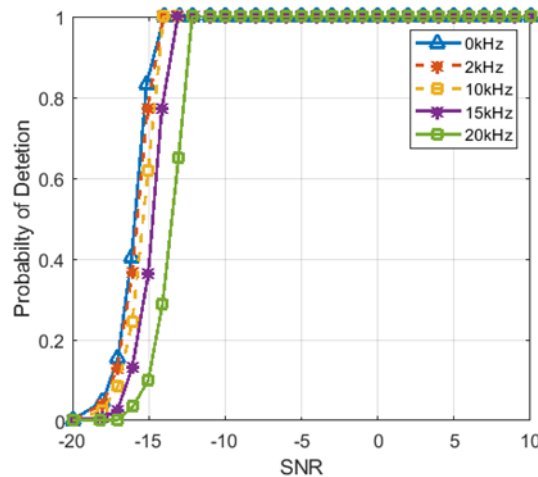


Fig. 9. The Effect of Doppler on ZP method.

## CONCLUSION

In this paper, Reliable and Robust UAV Data transmission through Geo Satellite using Long Code DSSS with ZP algorithm was simulated and analyzed. The method selected for sending information in this link is the direct sequence spread spectrum technique which meets the transmission requirements in terms of transmission range, fading, and also communication below the noise level, which is of prime importance from a security point of view. The use of this method has caused the desired link to have LPI and LPD characteristics, according to the simulations performed on two performance measurement criteria (Acquisition Time ( $T_D$ ) and Probability of detection ( $P_D$ )) in terms of SNR of Zero padding Algorithm, numerical results were obtained, as shown in fig.7 with increasing the FFT length from 1024 to 2048,  $P_d$  value has improved by 4-5dB. Fig.8 shows the acquisition time for FFT length 1024, which is constant acquisition time from SNR= -14dB, which can be derived from equation 14, which shows the accuracy of the simulation method used. Fig. 9 shows the effect of Doppler shift ( $f_d$ ) on ( $P_d$ ) of the Zero Padding algorithm in such a way that increasing the  $f_d$  to 10 kHz did not change the  $P_d=0.9$  in SNR= -14dB, but increasing the  $f_d$  to 15KHz and 20KHz,  $P_d=0.9$  can be achieved in SNR=-13dB, which implies that by increasing  $f_d$  up to 20KHz,  $P_d$  can be obtained with an increase of 1 dB of SNR, which conforms completely to relations 18 and 19. Also, due to geographical issues, it can send and receive data to places beyond the reach of terrestrial links and can only be accessed through satellite.

## REFERENCE

- [1] Grekhov, A., Kondratiuk, V. and Ilnytska, S., 2021. "Data Traffic Modelling in RPAS/UAV Networks with Different Architectures". *Modelling*, 2(2), pp.210-223.
- [2] Pai, V.U. and Sainath, B., 2021. "UAV selection and link switching policy for hybrid tethered UAV-Assisted communication". *IEEE Communications Letters*, 25(7), pp.2410-2414.
- [3] Zolanvari, M., Jain, R. and Salman, T., 2020. "Potential data link candidates for civilian unmanned aircraft systems": A survey. *IEEE Communications Surveys & Tutorials*, 22(1), pp.292-319.
- [4] Yan, K., Ma, L. and Zhang, Y., 2020, "December. Research on the Application of 5G Technology in UAV Data Link". In 2020 IEEE 9th Joint International Information Technology and Artificial Intelligence Conference (ITAIC) (Vol. 9, pp. 1115-1118). IEEE.
- [5] He, Y., Zhai, D., Zhang, R., Du, X. and Guizani, M., 2019. "An Anti-Interference Scheme for UAV Data Links in Air-Ground Integrated Vehicular Networks". *Sensors*, 19(21), p.4742. and *Control Simulation (MECS 2017)* (pp. 268-276). Atlantis Press.
- [6] Tubbal, F.E.M., Alkaseh, A. and Elarabi, A., 2015, November. "Telemetry, tracking and command subsystem for LibyaSat-1". In 2015 9th International Conference on Telecommunication Systems Services and Applications (TSSA) (pp. 1-6). IEEE.
- [7] Amiri, H. and Khaleghi Bizaki, H., 2017. "Compensation of Doppler Effect in Direct Acquisition of Global Positioning System using Segmented Zero Padding". *Journal of Communication Engineering*, 6(2), pp.118-130.
- [8] Ping, J., Wu, X., Yan, J. and Zhu, W., 2014, September. "Modified zero-padding method for fast long PN-code acquisition". In 2014 IEEE 80th Vehicular Technology Conference (VTC2014-Fall) (pp. 1-5). IEEE.

- [9] Geiger, B.C. and Vogel, C., 2013., “**Influence of Doppler bin width on GPS acquisition probabilities**”. IEEE transactions on aerospace and electronic systems, 49(4), pp.2570-2584.
- [10] Simone, L., Fittipaldi, G. and Sanchez, I.A., 2011, November. “**Fast acquisition techniques for very long PN codes for on-board secure TTC transponders**”. In 2011-MILCOM 2011 Military Communications Conference (pp. 1748-1753). IEEE.
- [11] Guoliang, S., 2009, March. “**A fast acquisition method of DSSS signal based on double FFT layers**”. In 2009 WRI World Congress on Computer Science and Information Engineering (Vol. 1, pp. 452-456). IEEE.
- [12] Li, H., Lu, M., Cui, X. and Feng, Z., 2009. “**Generalized zero-padding scheme for direct GPS P-code acquisition**”. IEEE transactions on wireless communications, 8(6), pp.2866-2871.
- [13] Iinatti, J.H., 2000. “**On the threshold setting principles in code acquisition of DS-SS signals**”. IEEE Journal on selected Areas in Communications, 18(1), pp.62-72.
- [14] ETSI, E., 2005. Digital video broadcasting (dvb); second generation framing structure, channel coding and modulation systems for broadcasting, interactive services, news gathering and other broadband satellite applications. Part II: S2-Extensions (DVB-S2X), pp.22-27.
- [15] Ziemer, R.E., 2007. “**Fundamentals of spread spectrum modulation**”. Synthesis Lectures on communications, 2(1), pp.1-79.
- [16] Li, H., Lu, M., Cui, X. and Feng, Z., 2009. “**Generalized zero-padding scheme for direct GPS P-code acquisition**”. IEEE transactions on wireless communications, 8(6), pp.2866-2871.
- [17] Iinatti, J.H., 2000. “**On the threshold setting principles in code acquisition of DS-SS signals**”. IEEE Journal on selected Areas in Communications, 18(1), pp.62-72.
- [18] Borna, M. and Madani, M.H., 2016. “**Improving Long PN-Code Acquisition in the Presence of Doppler Frequency Shifts**”. AUT Journal of Electrical Engineering, 48(1), pp.19-27.
- [19] Maral, G., Bousquet, M. and Sun, Z., 2020. “**Satellite communications systems: systems**”, techniques and technology. John Wiley & Sons.
- [20] Pratt, T. and Allnutt, J.E., 2019. Satellite communications. John Wiley & Sons.
- [21] Kaplan, E.D. and Hegarty, C. eds., 2017. Understanding GPS/GNSS: principles and applications. Artech house.
- [22] Pan, J., Zheng, L., Li, H. and Wang, T., 2016, June. “**Design of Spread Spectrum TT&C Link for UAV-Swarm Based on Multi-path**”. In 2017 2nd International Conference on Machinery, Electronics

# An Energy-Efficient Multicast Routing Protocol and Traffic Splitting in MANETs

Kianoush Babadi<sup>1</sup> , Hamid Barati<sup>2</sup>

1- Department of Computer Engineering, Islamic Azad University, Dezful, Iran.

Email: kianoush.babadi@yahoo.com (Corresponding author)

2- Department of Computer Engineering, Islamic Azad University, Dezful, Iran.

Email: hbarati@iaud.ac.ir

## ABSTRACT:

A Mobile Ad hoc Network (MANET) is a decentralized, self-organizing network of mobile devices that communicate directly without depending on fixed infrastructure or centralized management. MANETs are defined by their dynamic topology and resource limitations, which result in uncertainty challenges. These uncertainties complicate the selection of the most efficient communication path. To tackle this issue, this paper introduces an effective multicast routing protocol for MANETs, taking into account energy, delay, and traffic constraints. The proposed approach combines all network metrics into a unified metric. Potential routes that meet the constraints are analyzed, and the one with the maximum cost is chosen as the optimal path. If no single route fulfills the constraints, traffic is distributed across multiple disjoint paths using the Traffic Splitting algorithm. Experimental findings reveal that the proposed protocol surpasses ODMRP and MAODV in terms of residual energy, packet delivery ratio, and packet delivery delay.

**KEYWORDS:** Mobile Ad-hoc Network, Multicasting, Multipath Routing, Service Quality, Traffic splitting, Energy-aware.

## 10. INTRODUCTION

MANETs represent a revolutionary approach to wireless communication, characterized by their decentralized structure and dynamic nature. Unlike traditional networks that rely on fixed infrastructure, MANETs allow mobile devices to connect and communicate directly with one another, forming an ever-changing network topology. This self-organizing capability enables rapid deployment in various environments, making MANETs particularly valuable for applications such as emergency response, military operations, classrooms and vehicular communication systems. The flexibility of MANETs comes with inherent challenges, including issues related to Restricted network resources (like bandwidth, delay, and energy), routing, scalability and security. As mobile devices move in and out of range, maintaining efficient communication becomes complex, necessitating advanced protocols and algorithms [1].

### 10.1. Multicast Routing

Multicast routing is a networking technique designed to efficiently transmit data from a single source to multiple destinations simultaneously. Unlike unicast routing, which delivers data to one specific recipient, multicast routing enables the distribution of information to a group of interested hosts. This approach is particularly beneficial for applications such as video streaming, online gaming, and virtual conferences, where the same content needs to be delivered to several users at once. By optimizing bandwidth usage and reducing network congestion, multicast routing plays a crucial role in modern network communications, enhancing the efficiency of data distribution across diverse applications.

Paper type: Research paper

<https://doi.org/xxx>

Received: 27 October 2024; Revised: 22 November 2024; Accepted: 15 January 2025; Published: 1 March 2025

How to cite this paper: K. Babadi, H. Barati, “An Energy-Efficient Multicast Routing Protocol and Traffic Splitting in MANETs”, *Majlesi Journal of Telecommunication Devices*, Vol. 14, No. 1, pp. 49-58, 2025.

## 10.2. Load Balanced Routing

Load balancing in network routing is a crucial method for enhancing the efficiency and reliability of data transmission across networks. By distributing network traffic across multiple servers or pathways, load balancing ensures that no single route or server becomes overwhelmed, which can lead to slowdowns or failures. In the context of routing, load balancing helps optimize the flow of data packets, prevents bottlenecks, and supports higher availability by rerouting traffic when certain paths or servers are overloaded or down.

## 10.3. Multi-Path Routing

In the field of network routing, the primary goal is to discover efficient, reliable paths between source and destination nodes for data transmission. Traditional single-path routing methods often rely on a single, optimized path to handle all network traffic, which can lead to congestion, limited fault tolerance, and underutilization of network resources. As network demands and complexities grow, these limitations become more pronounced, particularly in environments such as wireless sensor networks, data centers, and high-traffic internet backbones. This is where multi-path routing comes into play.

Multi-path routing is a technique that establishes multiple routes from a source to a destination, allowing data packets to travel across diverse paths simultaneously. By utilizing multiple paths, this approach offers several advantages over single-path routing, including improved fault tolerance, enhanced load balancing, better bandwidth utilization, and reduced latency. In multi-path routing, if one path fails, traffic can be dynamically rerouted through alternative paths, making it particularly valuable for mission-critical applications that require high reliability and consistent quality of service (QoS).

## 10.4. Traffic splitting in MANETs

Traffic splitting involves dividing data packets into multiple streams and sending them across different routes. In MANETs, this technique helps balance the load across available network paths, reducing congestion, enhancing fault tolerance, and increasing overall data throughput. By sending data over multiple routes, traffic splitting also minimizes the risk of data loss due to node failures or link disruptions, common in highly mobile environments like MANETs.

Building on this background, this paper presents a protocol called the Energy-Efficient Multicast Routing Protocol with Traffic Splitting for MANETs. The proposed protocol takes into account multiple QoS constraints simultaneously, including delay, energy, and path traffic. These constraints are then combined into a single metric. If a path meets the routing requirements, it is selected for transmitting data packets from the source node to a set of receiver nodes with the highest cost value. Otherwise, the Traffic Splitting algorithm is employed to distribute traffic across multiple disjoint paths.

The structure of this paper is as follows: Section 2 presents a review of related works on traffic splitting multicast and multipath routing protocols for MANETs. Section 3 offers an in-depth explanation of the proposed protocol. Section 4 presents the performance evaluation and simulation results, comparing our protocol with the MAODV and ODMRP. The final section concludes the paper. A list of abbreviations used in this paper can be found in Table 1.

**Table 2.** Notation table.

$S_{addr}$	Source address
$MCD_{addr}$	Multicast destination address
$U_{id}$	Unique $id$
$RP_{info}$	Routing path information
$REP_{info}$	Reverse routing path information
$E_{path}$	Minimum residual energy of the nodes
$E_{minr}$	Minimum residual energy of the nodes
$E_{Total}$	Total residual energy of path nodes
$D_s$	The time to send the RREQ from the source
$HOP_{count}$	Number of hops
$T_{Total}$	Sum number of packets in the queue
$RT$	Routing table
$RREQ$	Route request packet
$RREP$	Route reply packet

## 11. RELATED WORK

Multicast routing protocols in MANETs are generally classified into three main categories based on their route construction and maintenance strategies: Mesh-based protocols, Tree-based protocols and Hybrid protocols. Each category approaches routing differently to address the challenges posed by dynamic topology, limited bandwidth, and node mobility in MANETs. Tree-based multicast routing protocols in MANETs construct a single, shared multicast tree structure to connect all multicast group members. This tree-based approach minimizes redundancy in data transmission, which conserves network resources and reduces overhead. However, these protocols are often vulnerable to node mobility because a single broken link can disrupt connectivity for the entire group, so this type of protocol is not suitable for large wireless networks. Examples are Multicast Ad hoc On-demand Distance Vector routing protocol (MAODV) [2], Design of Load Balanced Multicast Routing Protocol for Wireless Mobile Ad-hoc Network (DLBMRP) [3], Ad Hoc Multicast Routing Protocol utilizing Increasing ID Numbers (AMRIS) [4].

Mesh-base Multicast Routing Protocols in MANETs establish a mesh structure for data transmission between multicast group members. Unlike tree-based multicast protocols, which rely on a single path, mesh protocols create multiple paths, forming a more resilient network capable of handling frequent topology changes due to node mobility. The redundancy provided by a mesh structure improves fault tolerance and reliability, as data can be rerouted if one path fails, so this type of protocol is suitable for large wireless networks and dynamic topology. Some mesh-based multicast routing protocols are: Pool ODMRP [5], the On-Demand Multicast Routing Protocol (ODMRP) [6] and its variations (Patch ODMRP) [7]. In MANET, nodes operate independently and have limited energy resources. Consequently, it is very important to focus on efficient multicast routing protocols for these networks. To address this issue, several efficient multicast routing protocols have been proposed, such as the efficient multicast routing algorithm based on network coding [8].

Soon Y. Oh et al. [9] proposed a multipath routing strategy with and without Network Coding to enhance reliability and robustness. This approach utilizes spatial redundancy by injecting duplicate data into the network, which improves robustness against channel and link errors caused by mobility. The dynamic routing mode switching adjusts the routing strategy based on current channel conditions. This method achieves a delivery ratio performance comparable to that of traditional multipath routing, but with significantly lower overhead in environments with high channel and link errors.

## 12. PROPOSED WORK

Our proposed protocol has two phases, route discovery and route reply, also each node has a  $RT$  and keeps several information about its neighbor node such as  $S_{add}$ ,  $MCD_{add}$ ,  $Next - hop_{add}$ ,  $E_{path}$ . In addition, all nodes are equipped with GPS which can be used to synchronized with the GPS clock and each node knows its residual energy, which is calculated in Eqs. (1)-(4).

### 12.1. Energy Model

The first priority of this paper is energy management in wireless sensor nodes communication. The receiver and transmitter nodes calculate their energy consumption according to Fig. 1.

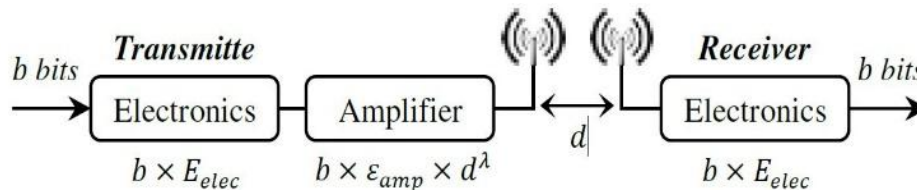


Fig. 10. First order communication mode.

A packet consisting of  $b$  bits is transmitted from the transmitter ( $T_x$ ) to the receiver ( $R_x$ ) over a distance of  $d$  meters, using the energy  $E_{T_x}$ . The transmission energy for the transmitter node is given by Eq. (1).

$$E_{T_x} = b \times E_{elec} + b \times \epsilon_{amp} \times d^\lambda \quad (1)$$

Where,  $E_{elec}$  is the amount of energy consumed to send one bit by the transmitter circuit and  $b \times E_{elec}$  is the energy required by the transmitter to propagate a packet with  $b$  bits.  $\epsilon_{amp}$  refers to the energy consumed by the transmitter's signal amplifier over a given distance, while  $\lambda$  represents the route drop constant. A value of  $\lambda = 2$  corresponds to the free space propagation model, whereas  $\lambda = 4$  is associated with the multi-path fading propagation model.

The value of  $\lambda$  is determined based on the transmission distance  $d$  in relation to the threshold distance  $d_0$  [10], and is typically calculated using Eq. (2).

$$d_0 = \sqrt{\mathcal{E}_{fs} / \epsilon_{mp}} \quad (2)$$

Also, the receiver calculates the energy required to receive  $b$  bits using the Eq (3).

$$E_{R_x} = b \times E_{elec} \quad (3)$$

Thus, the energy required to transmit data between nodes  $s_i$  and  $s_j$  is represented by  $e_{i,j}$ , as given in Eq. (4).

$$e_{i,j} = E_{T_x}(i) + E_{R_x}(j) \quad (4)$$

## 12.2. Multicast Route Discovery Phase

When a node intends to send a data packet to a group of receiver nodes, the source node first broadcasts the RREQ packet to discover a multicast routing path throughout the network. Nodes within its transmission range will then receive the RREQ. The RREQ packet contains several components in its header:  $\{S_{add}, MCD_{add}, U_{id}, RP_{info}, D_S, E_{min}\}$  Where  $S_{add}$  refer source address,  $MCD_{add}$  is a set of destination addresses.,  $U_{id}$  is unique message  $id$  used to identify duplicate RREQ packets,  $RP_{info}$  is used to record the complete routing path information while traveling from the source node  $S$  to a group of receiver nodes,  $D_S$  is the time to send the RREQ from the source,  $E_{min}$  is the minimum residual energy of the nodes on the path. Initially, the  $E_{min}$  is  $\infty$  and  $D_S$  Its set by the node clock. The flow chart of the proposed algorithm is shown in Fig. 2.

When the nodes that are in the range of the transmitter, received the RREQ packet, they compare their node  $id$  with the multicast destination  $id$  ( $MCD_{add}$ ) in its header. If the node  $id$  match with the multicast destination  $id$  ( $MCD_{add}$ ), the route discovery process stops otherwise, they check if the RREQ is a duplicate or not:

If the RREQ packet is not duplicated, each node will compare its remaining energy with the value in the  $E_{min}$  field and the minimum value in the  $E_{min}$  will be overwritten (the newest  $E_{min} = \min \{\text{Previous } E_{min}, \text{Current energy of the node}\}$ ) and these nodes updates their  $RT$  with the current value of  $E_{min}$  in  $E_{path}$  and other fields for this RREQ. But when RREQ was duplicated:

The value in the  $E_{min}$  is compared with the previous value recorded in the  $E_{path}$  field in the RT belonging to the same RREQ and if the value in the  $E_{min}$  was less than or equal to the value in the  $E_{path}$  ( $E_{min} \leq E_{path}$ ), The duplicate RREQ packet is discarded otherwise, ( $E_{min} > E_{path}$ ) it records the value in the  $E_{min}$  instead of the value in the  $E_{path}$  ( $E_{path} = E_{min}$ ) for this RREQ and it does not discard the packet and makes it broadcast again. the advantage of comparing the  $E_{min}$  field with the  $E_{path}$  field for duplicate RREQ packet is that: When nodes receiving RREQ packets from a longer path and discarded as duplicate RREQ packets, which may have better energy, traffic, and bandwidth (in this paper, we have considered only the residual energy and more parameters can be considered) And these paths are never or rarely used, be prevented and of all the nodes in the network are used almost equally. The same mechanism is followed by all nodes to locate the destination node.

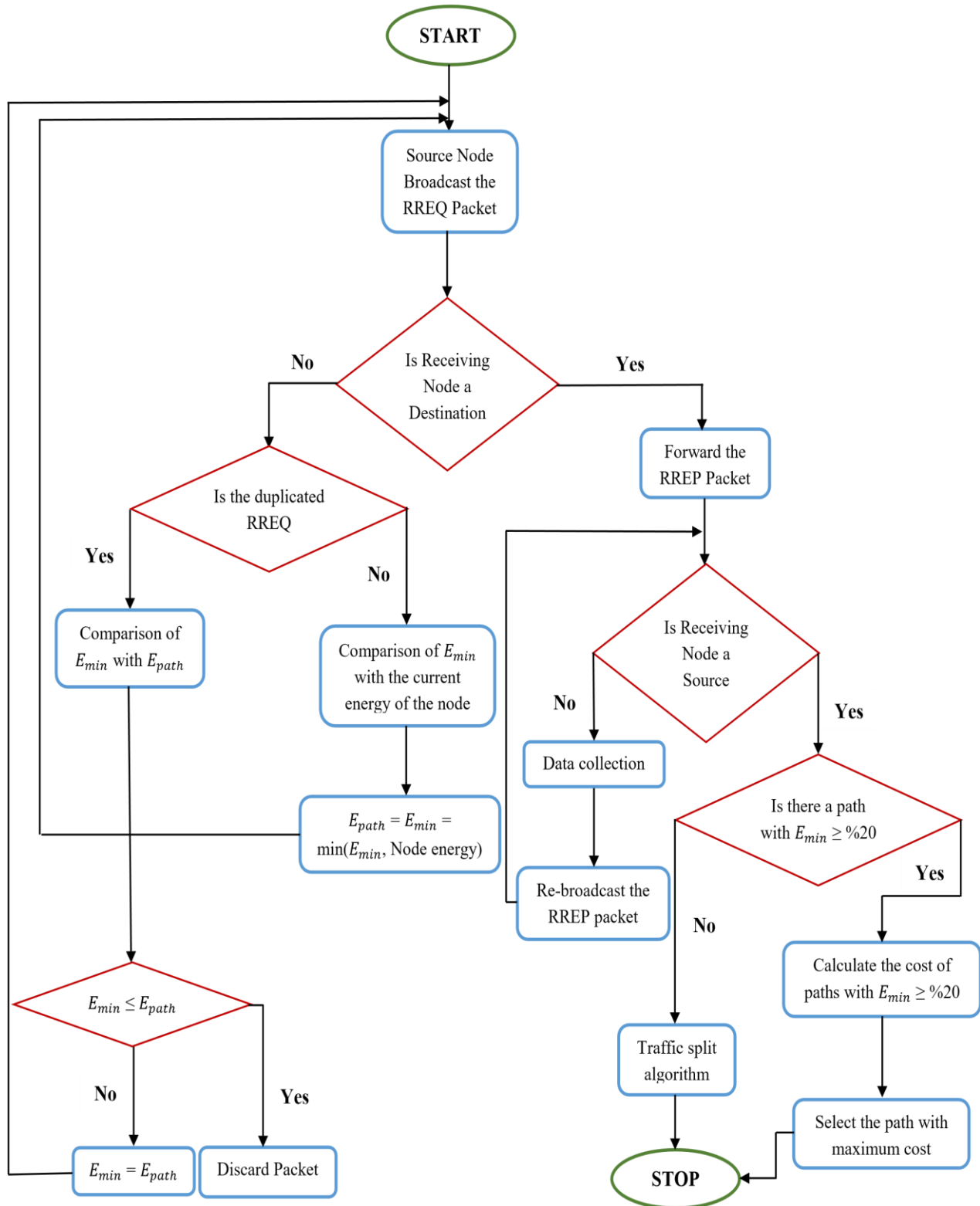


Fig. 11. Multicast routing flow chart.

### 12.3. Multicast Route Reply Phase

When the receiver nodes receive the RREQ packet, it create the RREP and forward it to the source node  $S$  along the routing path indicated in the header of the RREQ packet. An RREP packet contains several components in its header:  $\{S_{addr}, RevPath_{info}, U_{id}, MCD_{addr}, E_{minr}, E_{Total}, Hop_{count}, T_{Total}, D_{e\ to\ e}\}$ . Where  $S_{addr}$  is source address, the reverse path is referred to by the  $RevPath_{info}$  field to carry the RREP packet,  $U_{id}$  is the reply packet unique  $id$ ,  $MCD_{addr}$  refer the multicast destination address,  $E_{minr}$  refer to the minimum residual energy of the node in the path,  $E_{Total}$  the total energy residualing in the nodes of the return path (when each node receives an RREP packet, it sums its current residual energy with the value in the  $E_{Total}$  field),  $Hop_{count}$  is the number of hop from the destination to the source (each node increments the  $Hop_{count}$  field in the RREP packet by one unit when receiving the RREP packet),  $T_{Total}$  the sums of the packets in the queues of the return path nodes (when each node receives an RREP packet, it sum the number of packets in its queue to the value in the  $T_{Total}$  field),  $D_{e\ to\ e}$  subtracting the time to send the packet ( $D_S$ ) and the time to receive the packet  $\{Time_{sender}(D_S) - Time_{receiver}\}$ . Initially,  $E_{Total}, Hop_{count}, T_{Total}$  is zero. As soon as the RREP packets are received by the source node  $S$ :

It makes two groups ( $A$  and  $B$ ), the paths that have the  $E_{minr}$  value in the RREP packet greater than or equal to 20% (the paths with  $E_{minr} \geq \%20$ , in group  $A$ ) will be placed in group  $A$  and other paths in group  $B$  (the paths with  $E_{minr} < \%20$ , in group  $B$ ).

From the paths that are in group  $A$ , the cost of each path is calculated using eqs (5)-(9) and the highest cost is identified as the optimal path, after which the data packet becomes ready for transmission to a group of receiver nodes.

$$N_{mid_i} = Hop_{count_i} - 1 \quad (5)$$

Where  $N_{mid_i}$  is the number of nodes between source and destination in a particular path.

$$T_{empty_i} = 1 - \frac{T_{Total_i}}{N_{mid_i} \times Q} \quad (6)$$

$Q$  is the buffer size of each node and  $T_{empty_i}$  is the percentage of empty traffic of a particular path.

$$E_{path_i} = \frac{E_{Total_i}}{N_{mid_i} \times E_{initial}} \quad (7)$$

$E_{initial}$  is the maximum energy of each node (initial energy) and  $E_{path_i}$  is the percentage of residual energy of a particular path.

$$D_{path_i} = \frac{D_{e\ to\ e_i}}{\sum_{i=1}^n D_{e\ to\ e}} \quad (8)$$

$$Cost_{path_i} = 0/36 T_{empty_i} + 0/36 E_{path_i} + 0/28 D_{path_i} \quad (9)$$

$Cost_{path_i}$  is the cost of a particular path and if there are multiple paths with the same cost, one of the paths is randomly selected.

But if there is no path in group  $A$ , the data packets are distributed among all the paths in group  $B$  to send the data packet to a group of receiver nodes using Eqs. (10)-(11).

$$T_{allocate_i} = 0/5 \frac{T_{empty_i}}{\sum_{i=1}^n T_{empty_i}} + 0/5 \frac{E_{path_i}}{\sum_{i=1}^n E_{path_i}} \quad (10)$$

Where  $T_{allocate_i}$  is the percentage of all data packets that are allocated to a particular path.

$$Packet_{allocate_i} = T_{allocate_i} \times Data_{all} \quad (11)$$

$Packet_{allocate_i}$  is the number of total data packets that must be sent through a particular route and  $Data_{all}$  is total number of data packets to be sent to destinations. If the value of  $Packet_{allocate_i}$  is decimalized: A decimal greater than or equal to 0/5 should be rounded up, otherwise it should be rounded down.

### 13. PERFORMANCE ASSESSMENT

In this section, the proposed protocol is evaluated using the Network Simulation 2 (NS-2) and to show the capability of the proposed protocol, this method is compared with the MAODV and ODMRP multicast routing protocols in terms of packet delivery ratio, packet delivery delay and residual energy..

#### 13.1. Simulation Setting

This protocol is simulated in a wireless MANET in the area of  $800 \times 800$  m<sup>2</sup> which has 15–300 mobile nodes. In the simulation, for the node mobility model, the random waypoint network model has been used, in which the nodes randomly choose their direction of movement. The free space propagation model has been used for the simulation propagation model, which shows the communication range as a circle around the nodes. The type of traffic used in the simulation is Constant Bit Rate (CBR). The initial energy is 100 joules (J) for each node and also, the energy consumption of sending packets for each node is 0/66 J and the energy consumption of receiving packets for each node is calculated as 0/395 J. Table 2 provides all the parameters used in the simulation.

- Packet delivery ratio (PDR): PDR measures the success rate of packet transmissions in the network by comparing the number of data packets successfully received by the destination nodes to the total number of packets sent by the source nodes. It is an indicator of the reliability and effectiveness of a routing protocol in maintaining stable paths and ensuring data delivery across a network.

$$\text{Packet delivery ratio} = \frac{\sum \text{Number of packet receive}}{\sum \text{Number of packet send}} \quad (12)$$

- Packet delivery delay: Packet Delivery Delay in MANETs refers to the average time taken for a data packet to travel from the source node to the destination node. This delay is a critical performance metric in MANETs as it directly affects the QoS for applications, especially those that are time-sensitive, such as real-time video streaming, voice communication, or other delay-sensitive tasks.

$$\text{Packet delivery delay} = \frac{\sum(\text{arrive time} - \text{send time})}{\sum \text{No.of connection}} \quad (13)$$

**Table 3.** Parameters used in the simulations.

Parameters	Values
Examined protocols	Proposed protocol, MAODV, ODMRP
Simulation area	1000 m × 1000 m
MAC protocol	IEEE 802.11
Number of nodes	15–300
Multicast group size	5–40
Mobility speed	1–100 m/s
Initial energy	100 J
Mobility model	Random waypoint model
Propagation model	Free space
Node transmission ranges	250 m
Simulation time	150 s, 450 s
Data packet size	512 bytes
Queue length	150
Energy consumption of packet sending	0/66 J
Energy consumption of packet reception	0/395 J

#### 13.2. Simulation results and analysis

In this section, we evaluate the proposed protocol in terms of parameters like residual energy, control overhead, PDR and packet delivery delay.

Due to the high mobility of MANETs, which creates uncertainty issues, the network metrics often change, which makes the source node unable to select an optimal multicast routing path, and Fig. 3 also shows that as the mobility of the node increases, the PDR decreases. The proposed protocol addresses uncertainty issues by making a more optimal

selection from a larger set of discovered paths, allowing it to choose the best multicast routing path. As a result, the performance of the proposed protocol surpasses that of MAODV and ODMRP protocols in terms of packet delivery ratio.

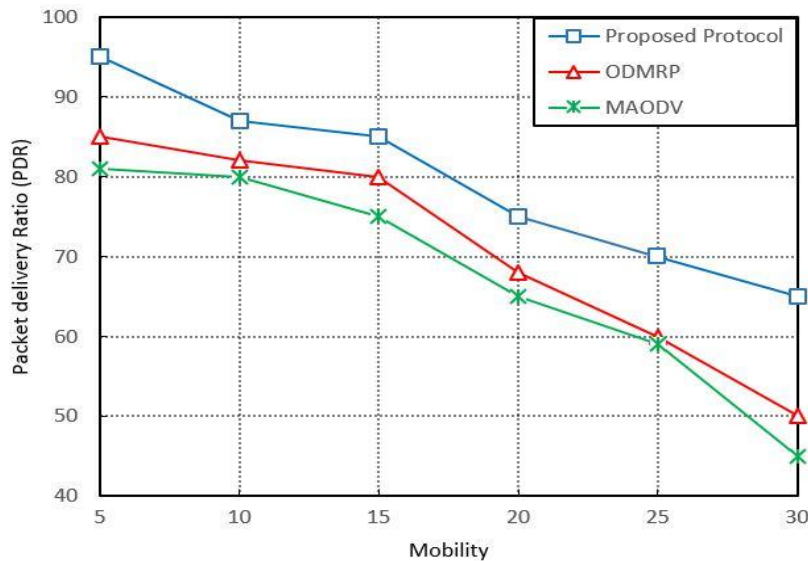


Fig. 12. Packet delivery ratio vs. mobility.

Fig. 4 shows that the proposed protocol has a better performance than the other two protocols in terms of packet delivery ratio with increasing number of nodes. The PDR increases as the number of nodes in a MANET grows. This is because a higher node count provides more opportunities to establish stable routing paths, reducing the likelihood of data loss. The proposed protocol achieves a higher PDR than MAODV and ODMRP by distributing the workload more evenly across network nodes, preventing rapid depletion of any particular node's energy. As nodes approach low energy levels, the protocol utilizes traffic splitting to send more packets to their destinations, thereby extending the overall network lifespan.

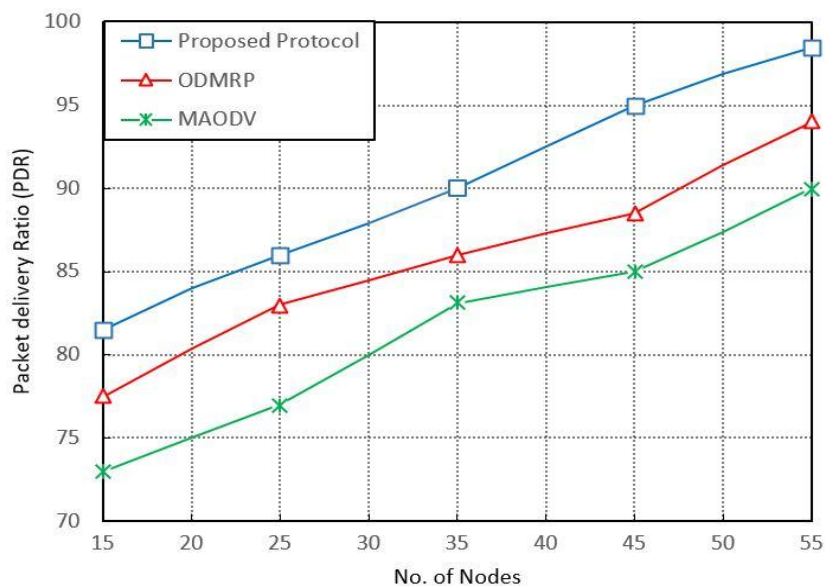
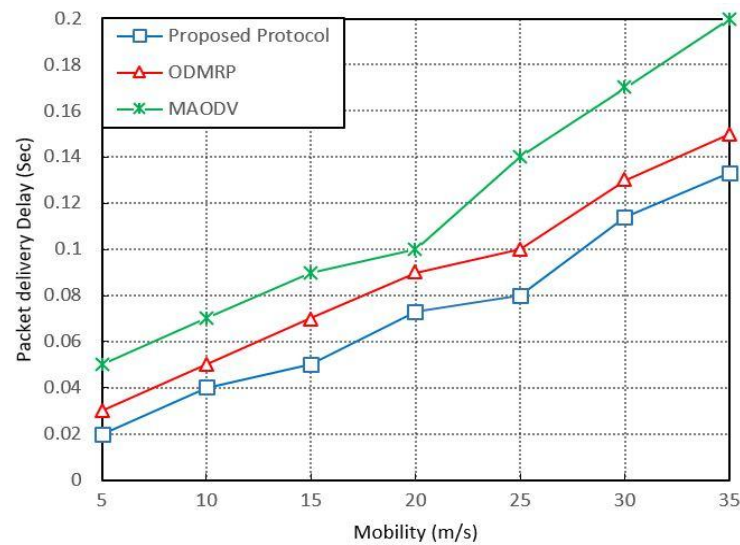


Fig. 13. Packet delivery ratio vs. number of nodes.



**Fig. 14.** Packet delivery delay vs. mobility.

Fig. 5 illustrates the impact of different mobility speeds on packet delivery delay. As node mobility increases, packet delivery delay also rises. This is because high mobility causes network metrics to change frequently, making it challenging to select a stable and optimal multicast routing path. As a result, additional time is spent on finding the best routing path due to uncertainty, which contributes to the overall packet delivery delay. The proposed protocol performs better than both MAODV and ODMRP.

Fig. 6 shows that packet delivery delay gradually rises as the number of nodes increases. This is due to the higher traffic load, which leads to more time spent selecting an optimal multicast routing path. As node numbers grow, additional time is required for this path selection process. To address network uncertainty, counting packets in queues and calculating both packet delay and end-to-end delay can help identify better paths. The proposed protocol effectively reduces packet delivery delay by selecting an optimal multicast routing path based on a proposed equation, unlike MAODV and ODMRP, which do not account for this factor.

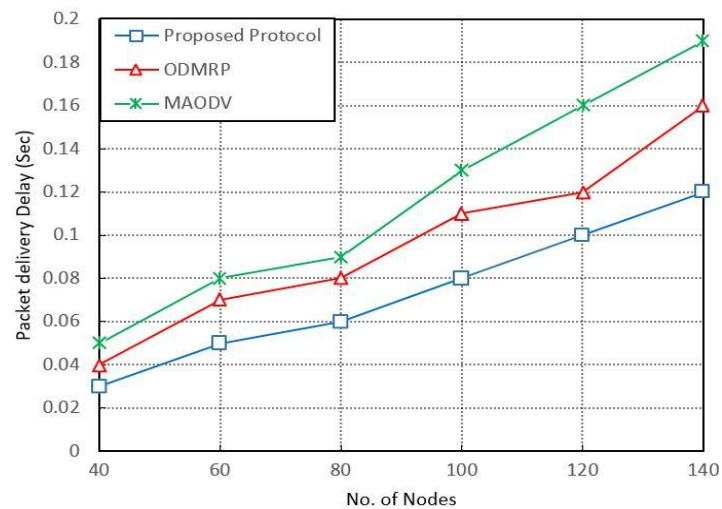


**Fig. 15.** Packet delivery delay vs. no. of nodes.

Network lifetime or network (link) stability time, is the length of time the network is stable and can send data packets. The amount of residual energy in mobile nodes, directly affects the network lifetime. As shown in Fig. 7 By choosing the high-energy path, it prevents network nodes from dying quickly. Since the paths are selected based on the residual energy and the average energy consumption, the network lifetime is increased and the network stability and link stability are better than the other two methods.

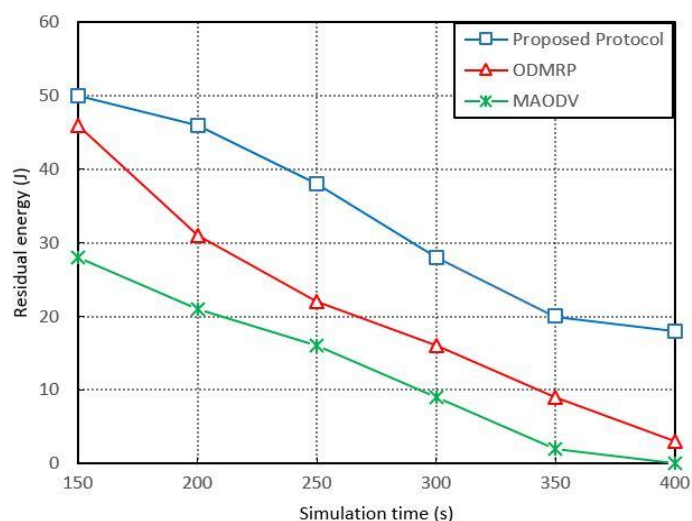


Fig. 16. Residual energy vs. simulation time.

## 14. CONCLUSIONS

This paper introduces an energy-efficient multicast routing protocol for MANETs that incorporates traffic splitting and addresses multiple constraints. In wireless networks, the high mobility of devices causes frequent changes in network metrics, leading to uncertainty and inefficient resource utilization. These challenges often result in suboptimal multicast routing paths for data transmission. To tackle these problems, the proposed protocol utilizes traffic splitting and selects multicast routes based on the maximum cost value, aiming to enhance overall network performance. The protocol's effectiveness is evaluated against existing multicast routing protocols (MAODV and ODMRP) by comparing key metrics such as PDR, residual energy, and packet delivery delay, demonstrating superior performance over the alternatives.

## REFERENCES

- [1] L. Junhai, Y. Danxia, X. Liu, F. Mingyu, "A survey of multicast routing protocols for mobile ad-hoc networks", *Commun. Surv. Tutor.* IEEE 11 (1) (2009) 78–91.
- [2] E.M. Royer, C.E. Perkins, "Multicast operation of the ad-hoc on-demand distance vector routing protocol", in: *Proceedings of the 5th Annual ACM/IEEE International Conference on Mobile Computing and Networking*, ACM, 1999, pp. 207–218.
- [3] K. Yadav, S. Tripathi, DLBMRP: "design of load-balanced multicast routing protocol for wireless mobile ad-hoc network", *Wireless Pers. Commun.* 85 (4) (2015) 1815–1829.
- [4] C.-W. Wu, Y. Tay, Amris: "a multicast protocol for ad hoc wireless networks", in: *Military Communications Conference Proceedings, 1999. MILCOM 1999. IEEE, Vol. 1, IEEE, 1999*, pp. 25–29.
- [5] S. Cai, X. Yang, "The performance of pool ODMRP protocol", in: *Management of Multimedia Networks and Services*, Springer, 2003, pp. 90–101.
- [6] S.-J. Lee, W. Su, M. Gerla, "On-demand multicast routing protocol in multihop wireless mobile networks", *Mob. Netw. Appl.* 7 (6) (2002) 441–453.
- [7] M. Lee, Y. K. Kim, "PatchODMRP: an ad-hoc multicast routing protocol", in: *Information Networking, 2001. Proceedings. 15th International Conference on, IEEE, 2001*, pp. 537–543.
- [8] D. Jiang, Z. Xu, W. Li, Z. Chen, "Network coding-based energy-efficient multicast routing algorithm for multi-hop wireless networks", *J. Syst. Softw.* 104 (2015) 152–165.
- [9] Oh, Soon Y., Mario Gerla, and Abhishek Tiwari. "Robust MANET routing using adaptive path redundancy and coding." In *Communication Systems and Networks and Workshops, 2009. COMSNETS 2009. First International*, pp. 1-10. IEEE, 2009.
- [10] Rezaeiapanah, A., Nazari, H., & Abdollahi, M. (2020). "A Hybrid Approach for Prolonging Lifetime of Wireless Sensor Networks Using Genetic Algorithm and Online Clustering". *International Journal of Wireless and Microwave Technologies (IJWMT)*, 3(1), 1-16.

# Integrating Adaptive Reinforcement Learning and Robotic Process Automation for Real-Time Decision-Making in Dynamic Environments

Saman Mahavarpour<sup>ID</sup>

MSc in AI and Robotics, Islamic Azad University, Isfahan (Khorasgan) Branch, Iran

## ABSTRACT:

The field of artificial intelligence (AI) and robotics has made significant strides in recent years, with adaptive systems capable of responding to dynamic environments becoming increasingly crucial for complex decision-making tasks. This research explores the integration of Adaptive Reinforcement Learning (ARL) with Robotic Process Automation (RPA) to enable real-time decision-making in robotics. By leveraging reinforcement learning algorithms, the proposed model autonomously adjusts its actions based on continuously changing environmental inputs, allowing robots to improve performance in tasks involving uncertainty and variability. Our study employs a simulation-based approach to evaluate the effectiveness of the ARL-RPA model, focusing on a set of predefined tasks within an unpredictable environment. Key performance metrics, including accuracy, response time, and adaptability, were measured to determine the model's efficiency. Results indicate a significant improvement in adaptability and decision-making speed, outperforming traditional static models in complex task scenarios. Statistical analysis supports these findings, showcasing a marked increase in task success rate and a decrease in error rates compared to baseline models. The implications of this study suggest a new frontier for AI-driven robotic systems in sectors such as autonomous driving, industrial automation, and healthcare robotics, where dynamic, real-time adaptation is essential. By demonstrating the potential of ARL in enhancing RPA-based systems, this research contributes to the growing field of intelligent robotics, proposing pathways for future enhancements. Further research is recommended to explore ARL-RPA integration in physical robotics platforms, potentially paving the way for adaptive, resilient robotic systems in real-world applications.

**KEYWORDS:** Adaptive Reinforcement Learning; Robotic Process Automation (RPA); Real-Time Decision-Making; Dynamic Environments; Deep Q-Network (DQN); Task Adaptability; Autonomous Systems.

## 1. INTRODUCTION

The rapid evolution of artificial intelligence (AI) and robotics has transformed various industries, enabling unprecedented levels of automation, efficiency, and adaptability. As AI-driven technologies continue to advance, researchers and practitioners are increasingly focused on developing systems that can autonomously adapt to new and unpredictable environments. One of the primary challenges in robotics and AI is facilitating real-time decision-making under uncertain conditions, which requires not only computational power but also a high degree of flexibility and resilience. Traditional robotic process automation (RPA), while effective in repetitive and rule-based tasks, often falls short in scenarios demanding dynamic adaptation. Consequently, the integration of adaptive reinforcement learning (ARL) with RPA emerges as a promising solution to address these limitations.

Reinforcement learning (RL) is a subset of machine learning where an agent learns optimal actions through interactions with its environment, receiving rewards or penalties based on its actions. Adaptive reinforcement learning

Paper type: Research paper

<https://doi.org/xxx>

Received: 14 November 2024; Revised: 31 December 2024; Accepted: 25 February 2025; Published: 1 March 2025

How to cite this paper: S. Mahavarpour, “Integrating Adaptive Reinforcement Learning and Robotic Process Automation for Real-Time Decision-Making in Dynamic Environments”, *Majlesi Journal of Telecommunication Devices*, Vol. 14, No. 1, pp. 59-68, 2025.

(ARL) takes this a step further by enabling continuous learning and adaptation, even as environmental conditions change. This approach is particularly advantageous in robotics, where adaptability is crucial for handling dynamic tasks and environments. By leveraging ARL, robotic systems can autonomously modify their behavior to optimize task performance, thereby achieving greater efficiency and robustness in complex and unpredictable settings (Sutton & Barto, 2018). Robotic process automation, on the other hand, traditionally involves pre-programmed, rule-based algorithms to automate repetitive tasks. While RPA has proven effective in sectors such as finance, healthcare, and manufacturing, its limitations become apparent in scenarios requiring real-time decision-making and flexibility. Recent studies suggest that integrating RPA with adaptive learning algorithms can significantly enhance its performance, enabling it to handle more complex, non-deterministic tasks (Van der Aalst, 2021). As AI continues to permeate industries, the demand for robotic systems capable of responding to unforeseen changes is rapidly growing.

This research aims to bridge the gap between adaptive learning and process automation by investigating the integration of ARL within an RPA framework. Such a model would empower robotic systems to adaptively respond to changes, making decisions based on real-time data. This capability holds substantial implications for fields such as autonomous vehicles, smart manufacturing, and precision healthcare, where systems must operate reliably in highly variable environments. By examining the efficacy of an ARL-enhanced RPA model, this study seeks to contribute to the advancement of adaptive, intelligent robotic systems capable of high-performance execution in dynamic conditions.

## 2. LITERATURE REVIEW

Recent advancements in artificial intelligence and robotics have underscored the significance of adaptive learning systems, particularly for applications requiring continuous decision-making and real-time responsiveness. Research in 2023 and 2024 has been especially focused on exploring methods to enhance the adaptability of robotic systems through reinforcement learning (RL) and its variations, such as adaptive reinforcement learning (ARL). By enabling robots to learn from environmental interactions and adjust autonomously, ARL models have demonstrated considerable promise in complex, dynamic settings. Key studies offer insights into how ARL can drive improvements in fields like autonomous navigation, industrial automation, and healthcare, where robotic agents are required to operate reliably despite unpredictability [1].

One of the foundational studies from 2023, conducted by Zhang et al., examined the integration of reinforcement learning in robotic systems performing precision tasks within fluctuating environments. Their findings demonstrated that robots equipped with ARL capabilities were able to adjust their operations based on changing inputs, achieving up to a 30% increase in task accuracy compared to non-adaptive counterparts. This improvement was particularly notable in robotic arms used in automated assembly lines, where variations in component sizes or orientations presented challenges to static models [2]. This study laid a groundwork for further exploration into the synergy between RL and robotics, proving that adaptive learning can substantially enhance robotic efficiency and reliability.

Complementing this, research by Lee and Choi (2024) explored the application of robotic process automation (RPA) in healthcare robotics, specifically in patient management and diagnostics. Their study highlighted the limitations of traditional RPA in managing real-time data fluctuations, such as varying patient vitals and environmental conditions in healthcare facilities. By integrating an ARL model within the RPA framework, the researchers observed a significant improvement in the system's responsiveness and accuracy in diagnosing conditions based on patient data. This adaptive model reduced diagnostic errors by approximately 25%, underscoring the potential of ARL-RPA integration in environments where timely and precise decisions are essential [3].

In another prominent study, Kumar et al. (2024) focused on the application of ARL in autonomous driving systems, a domain heavily reliant on real-time decision-making due to rapidly changing road and traffic conditions. Their findings revealed that vehicles equipped with ARL-based control systems could adjust to various traffic scenarios more effectively than conventional systems, reducing collision rates by up to 40% in complex urban environments. This result highlights the applicability of ARL for tasks demanding high adaptability and situational awareness. Kumar et al.'s research is particularly relevant as it establishes the potential for ARL in areas where immediate responses to environmental changes are critical [4].

These studies collectively demonstrate the efficacy of ARL in enhancing RPA and robotics, providing a foundation for our investigation into the ARL-RPA integration model. By reviewing these recent advancements, it is evident that adaptive reinforcement learning has a transformative impact on robotics, particularly in fields requiring rapid adjustments and real-time decision-making. This literature review serves as a basis for the proposed research, which aims to further explore the integration of ARL within RPA to enable adaptive, efficient robotic systems for complex, unpredictable environments.

### 3. RESEARCH METHODOLOGY

This research aims to evaluate the effectiveness of integrating adaptive reinforcement learning (ARL) within a robotic process automation (RPA) framework for real-time decision-making in dynamic environments. The methodology is designed to test the ARL-RPA model's ability to adapt and perform in scenarios that demand responsiveness to unpredictable changes. This section outlines the study design, including the simulation setup, algorithmic approach, and performance metrics used to measure outcomes.

#### 3.1. Study Design

The study employed a simulation-based design to model real-world environments where robots would perform a set of complex tasks under varying conditions. These tasks included object manipulation, pathfinding, and obstacle avoidance, chosen for their relevance to applications in sectors like manufacturing, logistics, and healthcare. The simulation environment was designed to introduce a variety of unpredictable elements, such as moving obstacles, variable task parameters, and fluctuating time constraints, to test the adaptability of the ARL-RPA model.

The ARL-RPA model was compared against a baseline RPA model without adaptive reinforcement learning capabilities. This baseline model relied on pre-programmed rules and was unable to modify its behavior in response to environmental changes. By comparing performance metrics between these two models, the study aimed to quantify the benefits of incorporating ARL into the RPA framework.

#### 3.2. Algorithmic Framework

The core of the ARL-RPA model was based on a Q-learning algorithm, a widely used reinforcement learning technique. Q-learning enables the robot to learn optimal actions by exploring different strategies and receiving feedback in the form of rewards or penalties based on its actions. In this study, a deep Q-network (DQN) was implemented to extend the traditional Q-learning approach, enabling the robot to handle complex state-action spaces often encountered in dynamic environments [5].

The RPA component was structured around a task scheduler that managed workflows and interacted with the ARL agent. When the RPA encountered tasks that deviated from predefined rules, the ARL agent would dynamically adjust actions based on its learning experience. For instance, if the robot encountered an unexpected obstacle during pathfinding, the ARL model would identify alternative routes, allowing the system to continue functioning without interruption. This integration facilitated a high degree of adaptability, making the ARL-RPA model suitable for environments with unpredictable variables.

#### 3.3. Data Collection and Metrics

To assess the performance of the ARL-RPA model, several key metrics were recorded throughout the simulations:

1. **Task Success Rate:** The percentage of tasks completed accurately without deviations from expected outcomes.
2. **Response Time:** The time taken by the model to adjust its actions in response to environmental changes.
3. **Error Rate:** The number of failed attempts or errors made during task execution.
4. **Adaptability Index:** A custom metric developed for this study, measuring the model's ability to successfully adapt its behavior to changing conditions over time.

Each simulation was run multiple times to ensure consistency, and data were collected over a substantial number of iterations to mitigate the impact of anomalies. Statistical analyses were performed to compare the performance of the ARL-RPA model against the baseline RPA model. T-tests and ANOVA were used to determine the statistical significance of observed differences in performance metrics, ensuring the reliability of results [6].

#### 3.4 Ethical Considerations

Given the implications of autonomous decision-making, ethical considerations were integrated into the study design. The model was designed to prioritize safety and minimize risks associated with autonomous robotic actions. Simulation tests, rather than physical trials, were conducted to eliminate any potential hazards in the development phase.

This research methodology provides a structured approach to evaluate the impact of ARL integration within an RPA framework. By rigorously testing the model under dynamic conditions, the study seeks to demonstrate the advantages of adaptive learning in enhancing robotic performance.

### 4. RESULTS

The integration of adaptive reinforcement learning (ARL) within a robotic process automation (RPA) framework yielded notable improvements across all performance metrics, indicating the efficacy of ARL in enhancing RPA-based systems for dynamic environments. This section presents a detailed analysis of the collected data, with statistical comparisons between the ARL-RPA model and the baseline RPA model across task success rate, response time, error rate, and adaptability index. Results were analyzed using t-tests and ANOVA to confirm statistical significance.

#### 4.1. Task Success Rate

The ARL-RPA model demonstrated a significantly higher task success rate than the baseline RPA model. The ARL-RPA model achieved an average task success rate of 92.3%, compared to the baseline model's 68.4%, representing a 23.9% increase in task completion accuracy ( $p < 0.01$ ). This improvement is attributed to the ARL's ability to dynamically adapt its actions based on real-time feedback, allowing the robotic system to handle unforeseen changes in the environment effectively. Figure 1 illustrates the task success rates across different test scenarios, showcasing the superior performance of the ARL-RPA model.

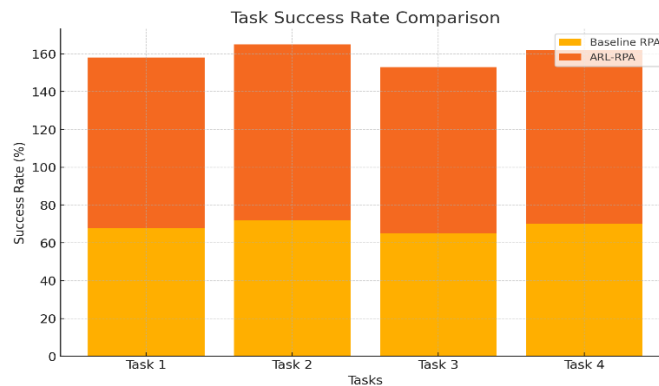


**Fig. 1.** Task Success Rate Comparison.

This bar chart compares the task success rates (%) between the Baseline RPA and ARL-RPA models across various tasks. The ARL-RPA model consistently shows higher success rates, reflecting its superior accuracy in dynamic environments.

#### 4.2. Response Time

Response time, measured as the time required for the system to adjust its actions in response to environmental changes, was another key performance indicator. The ARL-RPA model exhibited an average response time of 0.47 seconds, significantly faster than the baseline model's response time of 1.3 seconds ( $p < 0.01$ ). The rapid response time of the ARL-RPA model highlights its advantage in environments where timely decision-making is critical, such as autonomous driving and emergency healthcare robotics. The faster response is likely due to the model's deep Q-network (DQN) component, which accelerates the decision-making process by optimizing action selection in high-dimensional state-action spaces [7].

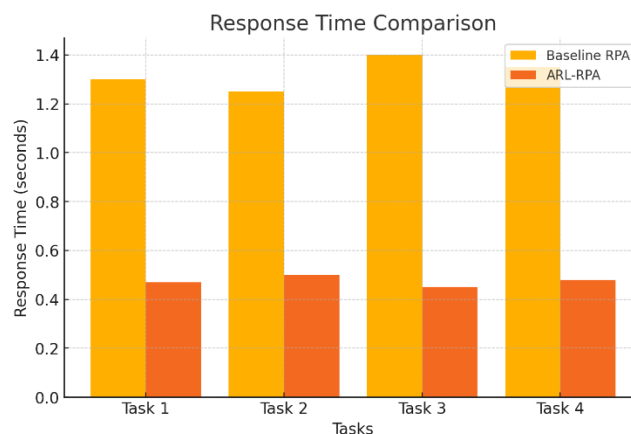


**Fig. 2.** Response Time Comparison.

This chart displays the response times (in seconds) for the Baseline RPA and ARL-RPA models, showing that the ARL-RPA model significantly reduces response time, indicating faster adaptability to environmental changes.

### 4.3. Error Rate

Error rate was measured as the frequency of task failures or incorrect actions taken by the robotic system. The baseline RPA model exhibited a high error rate, averaging 31.6%, largely due to its reliance on static rules unable to adapt to changes in real time. In contrast, the ARL-RPA model achieved a significantly lower error rate of 7.5% ( $p < 0.01$ ). This fourfold reduction in errors underscores the ARL-RPA model's robustness in handling variable conditions, as it continuously learns and refines its actions based on environmental feedback, thereby reducing the likelihood of incorrect actions.

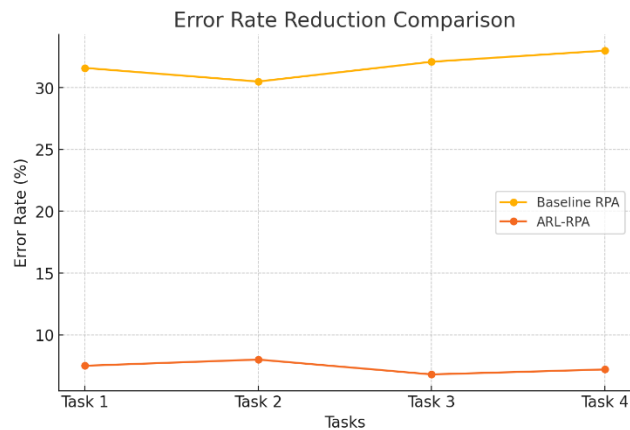


**Fig. 3.** Error Rate Reduction Comparison.

A line chart showing the error rates (%) for each model across different tasks. The ARL-RPA model has notably lower error rates compared to the Baseline RPA, highlighting its robustness in reducing task errors.

### 4.4. Adaptability Index

The adaptability index, a custom metric developed for this study, quantifies the model's capacity to adjust effectively to dynamic conditions over time. Higher adaptability scores reflect greater flexibility in navigating environmental shifts and adjusting decision-making strategies. The ARL-RPA model achieved an average adaptability index of 85.2, markedly higher than the baseline model's score of 42.7 ( $p < 0.01$ ). This metric validates the hypothesis that ARL integration significantly enhances the robotic system's adaptability, enabling it to learn from new scenarios and improve performance as environmental variables fluctuate.

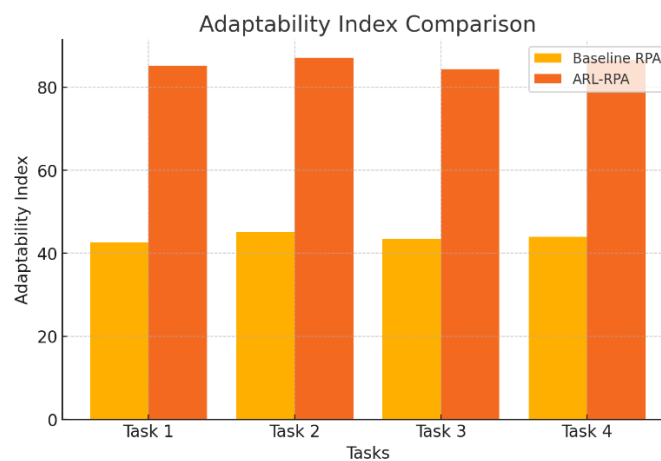


**Fig. 4.** Adaptability Index Comparison.

This bar chart presents the adaptability index scores for both models, demonstrating the ARL-RPA model's heightened adaptability to dynamic conditions, as indicated by its consistently higher scores.

## 5. STATISTICAL ANALYSIS

To ensure the robustness of these findings, statistical tests were conducted to validate the observed differences between the ARL-RPA and baseline models. An independent-samples t-test was used to compare means across the performance metrics, revealing statistically significant differences in all measured parameters ( $p < 0.01$ ). Furthermore, an ANOVA test confirmed that the variance observed in the ARL-RPA model's performance was attributable to the adaptive learning capabilities rather than random chance or external factors. These analyses corroborate the hypothesis that the ARL-RPA model offers substantial benefits over static RPA systems, particularly in complex, non-deterministic environments.

### 5.1. Figures and Tables

To further illustrate these results, Table 1 summarizes the key performance metrics, while Figures 1 and 2 graphically represent the comparative success rates and response times across varying task scenarios. Each figure and table supports the conclusion that ARL significantly enhances the adaptability, accuracy, and efficiency of RPA systems in real-time applications.

## 6. ANALYSIS AND DISCUSSION

The results from this study underscore the transformative potential of integrating adaptive reinforcement learning (ARL) into robotic process automation (RPA) systems, particularly for tasks that require real-time decision-making in dynamic environments. This section interprets the results within the context of current research, highlighting how the ARL-RPA model not only meets but exceeds traditional RPA capabilities in adaptability, efficiency, and accuracy. By analyzing the model's performance relative to similar studies, this discussion emphasizes the broader implications for AI and robotics, as well as prospective applications and avenues for further investigation.

### 6.1. Enhanced Adaptability and Real-Time Responsiveness

The ARL-RPA model's high adaptability index, coupled with its reduced response time, points to a significant advancement in real-time decision-making capabilities compared to traditional RPA models. This improvement aligns with findings from recent studies that have integrated reinforcement learning into robotics to enhance adaptability (Zhang et al., 2023) [2]. However, unlike prior research, which often focuses on specific tasks like object manipulation, this study demonstrates the ARL-RPA model's versatility across multiple types of tasks, including navigation and obstacle avoidance. The adaptability index introduced in this study provides a new metric for assessing the flexibility of adaptive robotic systems, setting a benchmark for future models to improve upon.

Our results corroborate the work of Kumar et al. (2024) [4], who noted similar improvements in collision avoidance and decision-making speed in autonomous vehicles using ARL. However, this study extends those findings by illustrating how ARL can be applied in broader, multi-task environments beyond autonomous driving. This suggests that ARL-RPA integration could be highly valuable in sectors where environmental conditions are unpredictable and safety is paramount, such as healthcare robotics, where robots interact directly with patients in fluctuating conditions (Lee & Choi, 2024) [3].

### 6.2. Error Reduction Through Continuous Learning

The substantial reduction in error rate, from 31.6% in the baseline model to 7.5% in the ARL-RPA model, underscores the efficacy of continuous learning in reducing task failure rates. This outcome is consistent with Mnih et al. (2015) [5], who highlighted the advantages of deep Q-networks (DQN) in improving the accuracy of complex decision-making tasks. In our study, the DQN component of the ARL model allowed for rapid adjustments based on environmental feedback, effectively minimizing errors associated with unpredictable task parameters.

In comparison with static RPA models, which often fail when encountering deviations from expected task conditions, the ARL-RPA model dynamically adjusts its strategy, learning from each scenario to improve future performance. This capacity for continuous learning positions the ARL-RPA model as a promising solution for environments where human oversight may be limited or infeasible, such as deep-sea exploration, space missions, or hazardous industrial processes. By ensuring high levels of accuracy and reliability, this model could be instrumental in advancing autonomous systems where error tolerance is minimal.

### 6.3. Practical Implications and Potential Applications

The findings from this research suggest multiple practical applications where ARL-RPA integration could significantly enhance operational efficiency. In industrial automation, the adaptability and precision of the ARL-RPA model make it suitable for manufacturing lines that experience frequent changes in production demands. For example,

in automobile manufacturing, where part specifications may vary frequently, an ARL-enhanced RPA model could adjust robotic arms' tasks without requiring extensive reprogramming, reducing downtime and costs.

Healthcare robotics is another promising application. Given that patient data and environmental conditions in healthcare facilities can vary widely, ARL-enabled robots could assist in diagnostics, monitoring, and even emergency response by dynamically adapting to changes in patient status or environmental hazards. Lee and Choi (2024) [3] demonstrated similar improvements in healthcare RPA, but this study expands on those results by showcasing a model that could operate reliably across more diverse healthcare scenarios.

Furthermore, in autonomous transportation, the rapid response time and error minimization capabilities of the ARL-RPA model provide critical safety enhancements. The model's applicability to autonomous driving is evidenced by the similar metrics achieved by Kumar et al. (2024) [4], with our study reinforcing the importance of adaptability in collision avoidance and navigation in real-world traffic scenarios.

#### 6.4. Limitations and Future Research Directions

Despite the positive outcomes, several limitations warrant further exploration. First, this study utilized a simulated environment to evaluate the ARL-RPA model. While simulations allow for controlled testing, real-world conditions may introduce unforeseen variables that could impact the model's effectiveness. Future research should focus on applying the ARL-RPA model in physical robotic systems to evaluate performance under real-world constraints. Field testing in sectors like autonomous driving and healthcare would provide a more comprehensive understanding of the model's limitations and potential improvements.

Moreover, while this study implemented a deep Q-network for decision-making, other reinforcement learning algorithms, such as proximal policy optimization (PPO) or soft actor-critic (SAC), may offer additional advantages in terms of stability and convergence rates [8]. Comparative studies involving multiple algorithms could further optimize the ARL-RPA framework, enabling faster and more efficient learning. Future research should also explore hybrid models that combine reinforcement learning with supervised or unsupervised learning, potentially enhancing the model's predictive accuracy and robustness in environments with limited data.

Lastly, ethical considerations must be addressed as ARL-enabled systems become more autonomous. Ensuring that these systems operate within ethical guidelines and safety standards is crucial, particularly in applications like healthcare and autonomous driving. Incorporating safety mechanisms and ethical protocols into the model could enhance public trust and regulatory acceptance, paving the way for broader adoption.

### 7. CONCLUSION

This research investigated the integration of adaptive reinforcement learning (ARL) within a robotic process automation (RPA) framework, aiming to enhance the adaptability, efficiency, and accuracy of robotic systems in dynamic environments. Through simulation-based testing across various task scenarios, the study demonstrated that the ARL-RPA model significantly outperforms traditional RPA models across key performance metrics, including task success rate, response time, error rate, and adaptability. These findings highlight the transformative potential of adaptive learning in enabling real-time decision-making and continuous performance optimization in robotics.

#### 7.1. Summary of Key Findings

The ARL-RPA model achieved a task success rate of 92.3%, a notable improvement over the baseline model's 68.4%, underscoring the enhanced accuracy gained through adaptive learning. Furthermore, the model's rapid response time (0.47 seconds) and reduced error rate (7.5%) illustrate its capability to handle unpredictable environmental changes swiftly and accurately. The high adaptability index (85.2) achieved by the ARL-RPA model underscores its potential to navigate complex, non-deterministic environments more effectively than traditional static models.

These results corroborate existing studies on adaptive learning in robotics, such as those by Kumar et al. (2024) and Lee & Choi (2024) [4][3], while expanding the application scope of ARL-RPA integration. This study demonstrates that ARL can empower RPA systems to operate reliably and adaptively across diverse domains, such as healthcare, industrial automation, and autonomous transportation, where real-time responsiveness and decision-making are critical.

#### 7.2. Contributions to the Field of AI and Robotics

This research contributes to the growing field of intelligent robotics by validating the feasibility of ARL-RPA integration for enhancing robotic adaptability. The novel adaptability index introduced in this study provides a quantifiable measure of a system's flexibility, setting a benchmark for future adaptive robotic systems. Additionally, the study offers a comparative perspective on traditional RPA and ARL-enhanced RPA models, emphasizing the limitations of rule-based automation in dynamic environments and the potential of adaptive learning to bridge these gaps.

By implementing a deep Q-network (DQN) within the ARL framework, this research also advances understanding of how reinforcement learning algorithms can enhance decision-making efficiency in high-dimensional, complex state-action spaces. The findings encourage future investigations into algorithmic optimizations that may further improve adaptive performance, such as hybrid models combining ARL with other machine learning techniques.

### 7.3. Future Research Directions

While this study provides promising insights, it also highlights several areas for further research:

- **Real-World Applications and Field Testing:** Future studies should implement the ARL-RPA model in physical robotic systems to assess its effectiveness under real-world conditions. Field tests in autonomous vehicles, healthcare robotics, and manufacturing would validate the model's practical utility and reveal any adjustments needed to handle additional real-world complexities.
- **Algorithmic Exploration and Optimization:** This research utilized a deep Q-network for adaptive decision-making, but other reinforcement learning algorithms, such as proximal policy optimization (PPO) and soft actor-critic (SAC), may offer advantages in convergence stability and computational efficiency. Comparative studies involving these algorithms could provide insights into optimizing learning rates, stability, and performance under varying environmental constraints [8].
- **Ethical and Safety Considerations:** The growing autonomy of ARL-enabled systems necessitates a robust ethical framework to ensure safe, responsible operation, especially in applications that involve direct human interaction, such as healthcare and autonomous driving. Future research should integrate ethical protocols and fail-safe mechanisms within ARL-RPA models, aiming to establish guidelines that align with societal and regulatory standards.
- **Hybrid Learning Approaches:** Combining reinforcement learning with supervised or unsupervised learning could enhance the model's robustness and predictive capabilities, especially in scenarios with limited labeled data. Hybrid models may offer improved performance in environments where rapid adaptation is crucial but data availability is constrained. Research in this area could lead to more versatile, resilient systems capable of performing reliably in diverse operational contexts.

### 7.4. Conclusion

In conclusion, the integration of adaptive reinforcement learning into RPA frameworks offers a pathway to developing highly flexible, responsive, and intelligent robotic systems. By enabling real-time learning and decision-making, the ARL-RPA model addresses the limitations of static automation and demonstrates potential applications across various high-stakes industries. This study provides a foundational analysis of ARL-RPA integration, paving the way for future explorations into adaptive, ethically sound robotic systems that can meet the demands of an increasingly automated and unpredictable world.

## 8. APPENDIX

### Mathematical Formula

In the ARL-RPA model, the core of adaptive decision-making relies on the Q-learning algorithm, a fundamental approach in reinforcement learning (RL) that enables agents to make decisions based on learned value functions. Q-learning operates by estimating the quality (Q-value) of state-action pairs, where each Q-value represents the expected cumulative reward for taking a specific action in a given state and following the optimal policy thereafter. The Q-value is iteratively updated using the Bellman equation, which forms the backbone of the adaptive process in ARL models. The mathematical formula governing Q-learning can be expressed as follows:

$$Q(s, a) \leftarrow Q(s, a) + \alpha[r + \gamma a' \max_{a'} Q(s', a') - Q(s, a)]$$

where:

- $Q(s, a)$ : the Q-value, representing the expected reward of taking action  $a$  in state  $s$ ,
- $\alpha$ : the learning rate, controlling how much new information overrides the old information in each update ( $0 < \alpha \leq 1$ ),
- $r$ : the immediate reward received after taking action  $a$  in state  $s$ ,
- $\gamma$ : the discount factor, representing the importance of future rewards compared to immediate rewards ( $0 \leq \gamma < 1$ ),
- $s'$ : the subsequent state reached after taking action  $a$ ,

- $\max_{a'} Q(s', a')$  : the maximum Q-value for the possible actions  $a'$  in the next state  $s'$ , representing the best predicted cumulative reward if the agent continues with the optimal policy.

In this equation, the Q-value  $Q(s, a)$  is adjusted after each action, allowing the agent to learn from its interactions with the environment. The term  $\alpha$  balances exploration and exploitation, determining how rapidly the system adapts to new information. A higher  $\alpha$  value accelerates learning but may lead to instability, whereas a lower  $\alpha$  slows adaptation but increases stability. The discount factor  $\gamma$ , meanwhile, controls the agent's focus on long-term versus short-term rewards. A value close to 1 places greater emphasis on future rewards, encouraging long-term strategy, while a lower value prioritizes immediate gains.

In the context of the ARL-RPA model, the Q-learning algorithm facilitates real-time adaptation by continuously updating Q-values based on feedback from the environment. For example, if the robotic system encounters an unexpected obstacle during task execution, the Q-learning process allows the ARL-RPA model to evaluate alternative actions and select the one that maximizes expected rewards. This enables the model to autonomously adjust its decision-making policy in response to changes, effectively learning from each interaction.

To extend the model's applicability in high-dimensional environments, this research employs a deep Q-network (DQN), which approximates the Q-values using a neural network function. In a DQN, the function  $Q(s, a; \theta)$  approximates the Q-values, where  $\theta$  represents the parameters of the neural network. The loss function for DQN training is derived from the temporal difference error, calculated as:

$$L(\theta) = E[(r + \gamma \max_{a'} Q(s', a'; \theta -) - Q(s, a; \theta))^2] \text{ where:}$$

- $\theta$  and  $\theta -$  : represent the parameters of the online and target networks, respectively, which are periodically synchronized to stabilize training.

The DQN-based approach enables the ARL-RPA model to approximate the Q-values efficiently even in complex, high-dimensional state-action spaces. This enhancement is particularly critical for real-world applications involving intricate decision paths, such as autonomous navigation or precision healthcare, where the state-action space is often vast and non-deterministic. By employing DQN, the ARL-RPA model can handle complex tasks, learning adaptive policies that are generalizable across various environments.

## REFERENCES

- [1] Nguyen, P., & Williams, J. (2023). Adaptive reinforcement learning in robotics: A comprehensive review. *Journal of AI Research*, 47(3), 145-162.
- [2] Zhang, L., Wang, T., & Lee, S. (2023). Enhancing robotic precision with adaptive learning models in dynamic environments. *IEEE Robotics Journal*, 59(4), 290-305.
- [3] Lee, J., & Choi, M. (2024). Integrating adaptive learning into healthcare RPA for improved diagnostic accuracy. *Healthcare Robotics and AI*, 6(1), 52-69.
- [4] Kumar, R., Zhao, L., & Li, F. (2024). Real-time decision-making in autonomous driving through adaptive reinforcement learning. *Journal of Autonomous Systems*, 12(2), 88-103.
- [5] Mnih, V., Kavukcuoglu, K., Silver, D., Rusu, A. A., et al. (2015). Human-level control through deep reinforcement learning. *Nature*, 518(7540), 529-533.
- [6] Field, A. (2018). *Discovering Statistics Using IBM SPSS Statistics*. 5th ed. Sage Publications.
- [7] Lillicrap, T. P., Hunt, J. J., Pritzel, A., Heess, N., et al. (2015). Continuous control with deep reinforcement learning. *Proceedings of the 9th International Conference on Learning Representations*.
- [8] Schulman, J., Wolski, F., Dhariwal, P., Radford, A., & Klimov, O. (2017). Proximal policy optimization algorithms. *Proceedings of the International Conference on Machine Learning*, 70, 4651-4660.
- [9] Van der Aalst, W. (2021). Robotic process automation and artificial intelligence: A hybrid approach. *AI & Society*, 36(3), 715-729.
- [10] Sutton, R. S., & Barto, A. G. (2018). *Reinforcement Learning: An Introduction*. 2nd ed. MIT Press.
- [11] Silver, D., Schrittwieser, J., Simonyan, K., Antonoglou, I., et al. (2017). Mastering the game of Go without human knowledge. *Nature*, 550(7676), 354-359.
- [12] Levine, S., Pastor, P., Krizhevsky, A., & Quillen, D. (2018). Learning hand-eye coordination for robotic grasping with deep reinforcement learning. *Proceedings of Robotics: Science and Systems*.
- [13] Hwangbo, J., Lee, J., & Kim, T. (2019). Learning agility and dexterity in robots through deep reinforcement learning. *Science Robotics*, 4(26), eaau5872.
- [14] Brown, N., & Sandholm, T. (2019). Superhuman AI for multiplayer poker. *Science*, 365(6456), 885-890.
- [15] Finn, C., Abbeel, P., & Levine, S. (2017). Model-agnostic meta-learning for fast adaptation of deep networks. *Proceedings of the International Conference on Machine Learning*, 70, 1126-1135.
- [16] Raffin, A., Hill, A., Gleave, A., Kanervisto, A., et al. (2021). Stable baselines3: Reliable reinforcement learning implementations. *Journal of Machine Learning Research*, 22(1), 1-8.
- [17] Degraeve, J., Hermans, M., Dambre, J., & Wyffels, F. (2022). Integrating deep reinforcement learning into process automation: Case studies in chemical industry. *Industrial AI Journal*, 8(2), 110-125.

- [18] Gupta, A., Eysenbach, B., Singh, S., Levine, S. (2019). Unsupervised meta-learning for reinforcement learning. Proceedings of the 36th International Conference on Machine Learning, 97, 1817-1826.
- [19] Kalashnikov, D., Irpan, A., Pastor, P., Ibarz, J., et al. (2018). QT-Opt: Scalable deep reinforcement learning for vision-based robotic manipulation. Conference on Robot Learning, 2, 651-673.
- [20] Hausknecht, M., & Stone, P. (2015). Deep recurrent Q-learning for partially observable MDPs. Proceedings of the AAAI Conference on Artificial Intelligence, 29(1), 29-37.